

POLITECNICO DI TORINO  
GRENOBLE INP - PHELMA  
ÉCOLE POLYTECHNIQUE FÉDÉRALE DE LAUSANNE

Master's Degree in Nanotechnologies for ICTs



*Master's Degree Thesis*

Design and optimization of one and two  
ports Two-Dimensional Mode Resonators  
for wide band RF applications

Supervisors

Prof. Cristian CASSELLA

Prof. Matteo COCUZZA

Prof. Stefano STASSI

Candidate

Fabio BERSANO

October 2020



# Summary

The aim of this Master's thesis is to optimize the design and performances of a novel class of piezoelectric Micro-Electromechanical Systems (MEMS) resonators for very and ultra high frequency (V/UHF) applications called Two-Dimensional-Mode resonators (2DMRs). The entire work has been conducted at the department of Computer and Electrical engineering of Northeastern University in Boston (MA,USA) under the supervision of professor Cristian Cassella and Ph.D. Luca Colombo.

The document is divided into six chapters and includes two appendices where details and design examples are described. The first chapter gives an introduction to the fundamental theory needed to understand the achievements of this work. A detailed analysis of the state-of-the-art of 2DMRs is then discussed and compared to other classes of piezoelectric MEMS resonators, with a focus on current performance limitations. With the aim of improving the quality factor at resonance  $Q$  and the electromechanical coupling coefficient  $k_t^2$  of 2DMRs without increasing the fabrication complexity, four different studies have been conducted and are explained in chapter three. The analyses have been carried on through 2D/3D FEM simulations with COMSOL<sup>®</sup> Multiphysics and analytically described with mathematical models. Firstly, the minimization of anchor losses is demonstrated through the analysis of an equivalent electrical circuit where inactive acoustic waveguides have been analytically modelled as transmission lines. The introduction of “*virtual fixed boundaries*” at the edge of the active areas through  $\lambda/4$  acoustic transformers showed how the optimization problem can be split in the definition of two energy transfer functions governing the design of the bus and the anchors. 3D FEM simulations with different boundary conditions (Fixed Constraints and Perfectly Matched Layers) demonstrated excellent agreement with the analytical models. Secondly, a new class of resonators named Two-Dimensional-Mode-Multimodal-Resonators ( $2DMR^M$ ) have been introduced here for the first time, demonstrating a boosting in the classical 2DMRs  $k_t^2$  thanks to a reactive coupling between the zero and the first order symmetric Lamb modes. A physical analysis of the multimodal resonators based on the dispersive relations of Lamb symmetric waves has been carried out and empirical design rules have been derived based on simulations

with different materials and layers thicknesses. The frequency lithographic tunability of  $2DMR^M$  has been computed and compared to the one of other MEMS resonators, demonstrating how this innovative configuration can overcome the limitations related to electrical loading and power handling common to many of other technologies. Moreover, as a way of reducing the residual stress in the piezoelectric film due to irregularities introduced by the bottom electrodes grating, an innovative 2DMR configuration including a continuous bottom electrode plate is discussed comparing the performances of different electrodes materials. Finally, several electrodes apodization shapes for spurious modes suppression have been simulated and compared obtaining unprecedented clean  $2DMR^M$  admittance responses in 3D simulations without affecting the electromechanical coupling coefficient. To conclude, an innovative 2-ports device exploiting a frequency selective evanescent coupling of two 2DMRs with applications in RF power sensing has been engineered and analysed for the first time in chapter four. Exhaustive experimental plans including hundreds of resonators have been outlined by parametrically drawing the lithographic masks with *ad-hoc* Python libraries coded with the *gdspy* module. The layouts and process flows are described in chapter five and conclusions are outlined in chapter six.

## COVID 19 EMERGENCY LIMITATIONS

To give a complete idea of the thesis work, it should be mentioned that the experimental plan has been prepared after months of simulations with the idea of fabricating, testing and characterizing the resonators in the cleanroom facility of Northeastern University during the last months of the internship. However, due to restrictions applied to exchange students, the fabrication has been performed by Ph.D. students. Although the work has been planned in advance, delays have accumulated due to increasingly severe restrictions and therefore no experimental data have been made available in time to be included in this thesis. However, this opened the possibility to extend and perfect the FEM simulations that are at the core of this work.

For the interested reader, the experimental results that are still being collected will be available in a few publications that are going to be submitted in the following months.

# Acknowledgements

I would like to thank my supervisor prof. Cristian Cassella for his continuous advice and support on my work. He taught me how to carry out the research with constancy, providing invaluable guidance in every step I made. I would like to express my sincere gratitude to Ph.D. Luca Colombo and Ph.D. Xuanyi Zhao for the management of the research activity and precious collaborations. Beside my supervisors, I would also thank the Principal Investigator of the lab professor Matteo Rinaldi, who gave me the opportunity to join his lab in an exciting environment for eight months. Sincere gratitude goes then to all the lab members who helped me by sharing their experience and knowledge on RF MEMS in our online weekly meetings. Last but not the least, I am extremely grateful to my parents, my sister and my friends for educating and supporting me throughout this intense experience, making me never feel alone. Finally, my heartfelt thanks go to Lodovica, who helped me in finding my way without compromises, caring about me in every moment, in every place.

*“... to infinity and beyond”*



# Table of Contents

<b>List of Tables</b>	IX
<b>List of Figures</b>	X
<b>1 Introduction</b>	1
1.1 RF MEMS resonators state of the art . . . . .	1
1.2 From piezoelectricity to RF resonators . . . . .	3
1.2.1 Piezoelectric materials for RF MEMS . . . . .	3
1.3 Piezoelectricity and Elastodynamics . . . . .	5
1.3.1 Piezoelectricity constitutive equations . . . . .	5
1.3.2 Fundamentals of elastodynamics . . . . .	8
1.3.3 Lamb wave theory . . . . .	10
1.3.4 Resonators and BVD model . . . . .	15
1.4 Resonators FoM . . . . .	19
1.4.1 Quality factor . . . . .	19
1.4.2 Electromechanical coupling coefficient . . . . .	21
<b>2 2DMRs and Lamb waves resonators</b>	23
2.1 Device description . . . . .	25
2.1.1 2DMR structure . . . . .	25
2.1.2 Materials considerations . . . . .	27
2.1.3 2DMR performances and mode analysis . . . . .	30
2.1.4 2DMR examples of applications . . . . .	31
2.2 2DMR Finite Element Modeling . . . . .	37
<b>3 2DMR design optimization</b>	41
3.1 Anchor losses optimization . . . . .	41
3.1.1 Bus dimensions design . . . . .	42
3.1.2 Anchor dimensions design . . . . .	45
3.2 2D Mode Multimodal Resonators . . . . .	58
3.3 Bottom plate resonators . . . . .	68

3.4	Apodization for spurious modes suppression . . . . .	72
<b>4</b>	<b>An innovative two-ports device</b>	<b>79</b>
4.1	Principle of operation and modeling . . . . .	79
4.2	Acoustic and electrical analyses . . . . .	80
<b>5</b>	<b>Layouts design</b>	<b>89</b>
5.1	Process flow and masks design . . . . .	89
5.2	Additional layouts . . . . .	94
<b>6</b>	<b>Conclusions</b>	<b>97</b>
<b>A</b>	<b>Electrical loading considerations</b>	<b>101</b>
<b>B</b>	<b><i>gdsfy</i> for layout drawings</b>	<b>107</b>
	<b>Bibliography</b>	<b>115</b>

# List of Tables

1.1	<i>measured properties of single crystal AlN [4]. . . . .</i>	8
3.1	<i>results from the study on the aperture A of the sinusoidal apodization. . . . .</i>	76
3.2	<i>comparison between different apodization shapes applied to the electrode fingers of a 2DMR. . . . .</i>	78
A.1	<i>experimental measurement of Pt thin film resistivity. . . . .</i>	103
A.2	<i>optimal configuration chosen for the 2DMR experimental plan considering the layers specifications. The 2DMR resonance frequency is <math>f_s \approx 2.2</math> [GHz] . . . . .</i>	103

# List of Figures

1.1	<i>positive and negative charges centres relative position in a molecule of a piezoelectric material without and in the presence of an external applied stress.</i> . . . . .	4
1.2	<i>deformation in solids, figure from [6].</i> . . . . .	5
1.3	<i>infinite plate assumed for the derivation of the Lamb theory.</i> . . . .	13
1.4	<i>2D model of a multilayered structure used for the evaluation of the dispersion curves for both the parallel and series resonances. The blue lines indicates the zero charge boundaries whereas the green and yellow lines indicate, respectively, the source and destination boundaries for the Floquet periodicity. The dispersion curves for the first five excited modes are also shown, where the dotted lines are related to <math>f_s</math> curves and solid lines to <math>f_p</math>.</i> . . . . .	14
1.5	<i>a) simplified FBAR structure b) equivalent electrical model of a resonator</i> . . . . .	15
1.6	<i>a) single resonance BVD model b) BVD model fitting of a 3D FEM simulation, the electrical parameters are listed in the inset.</i> . . . . .	16
1.7	<i>a) multi-resonances BVD model b) modified BVD model</i> . . . . .	18
2.1	<i>mode shapes of an (a) FBAR, (b) CMR and (c) XDMR (figure from [12]).</i> . . . . .	24
2.2	<i>comparison between Lamb wave resonators exciting thickness extensional modes. The <math>kt^2</math> refers to the maximum value experimentally demonstrated.</i> . . . . .	25
2.3	<i>3D and 2D profiles of a 2DMR resonator. The 2D model shows the section of the device cut by the red line.</i> . . . . .	26
2.4	<i>(a) number of 2DRM fingers vs length of the fingers that satisfy different impedance matching conditions (b) <math>R_s</math> dependence on the finger length for different impedance matching conditions. The plots refer to a Pt/AlN 2DMR with electrode width fixed to 1.25 <math>[\mu\text{m}]</math> and the matching resistance values are expressed in <math>[\Omega]</math>.</i> . . . . .	28

2.5	<i>schematic of a 2DMR with additional anchors along its length (figure from [16]) . . . . .</i>	29
2.6	<i>effective coupling computed for CLMRs with different materials and AlN thicknesses. The results can be generalized to the case of 2DMRs (plot from [1]). . . . .</i>	29
2.7	<i>2D displacement of a 2DMR exciting the S1 mode. . . . .</i>	31
2.8	<i>dispersion curves relative to the first 5 acoustic modes excited in the active area of the structure presented in fig.2.7. The curves have been computed through a Comsol<sup>®</sup> 2D model . . . . .</i>	32
2.9	<i>schematic representation of a Ladder filter. . . . .</i>	33
2.10	<i>experimental results of a Ladder filter based on CLMRs. <math>BW_{3dB} \approx 2.9\%</math> and <math>I.L. \approx 0.4</math> dB were demonstrated [19]. . . . .</i>	34
2.11	<i>schematic of an MEMS resonator-based oscillator (fig. from [20]). The MEMS acts as a filtering stage in the feedback loop of the sustaining amplifier at the resonance frequency. . . . .</i>	35
2.12	<i>envisioned change in RF front-end architecture from a single band to a multi-band system enabled by the monolithic integration of AlN based MEMS resonators (fig.from [21]). 2DMRs could replace CMRs thanks to the optimized performances presented in this thesis. . . . .</i>	36
2.13	<i>2D COMSOL<sup>®</sup> model of the periodic structure modelling the transverse section of a 2DM resonator. . . . .</i>	37
2.14	<i>3D COMSOL<sup>®</sup> model of a 2DMR including the resonator, the released area and the PMLs. . . . .</i>	38
2.15	<i>mesh of the 3D FEM model of a 2DMR including resonator, released area and PMLs. . . . .</i>	40
2.16	<i>3D COMSOL model of a 2DMR including the resonator, the released area and the PMLs with a symmetry plane to reduce the computational efforts and time. . . . .</i>	40
3.1	<i>(a) 3D model used for the study on the bus and (b) inactive area dimensions that have been optimized. . . . .</i>	42
3.2	<i>normalized transfer function governing the acoustic energy generated towards the anchors direction and mechanical energy density stored in the 2DMR active areas versus normalized <math>d</math> dimensions. . . . .</i>	45
3.3	<i>equivalent electrical circuit of the active and inactive region in a 2DMR. The anchor is modelled as a transmission line. . . . .</i>	46
3.4	<i>FEM simulation of a 2DMR assuming FC at the edges of the released area. <math>E_{stored}</math> is computed over the resonator and anchors volumes whereas <math>E_{lost}</math> is computed over the anchors/substrate interfaces through the acoustic Poynting's vector. <math>\mathbf{T}</math>, <math>\mathbf{S}</math> and <math>\mathbf{u}</math> are respectively the stress and strain tensors and the displacement vector. . . . .</i>	49

3.5	<i>function governing the dependence of the quality factor <math>Q</math> on anchor dimensions for fixed <math>d \approx n\lambda/4</math> and normalized <math>Q</math> values extracted from simulations for different anchor lengths.</i>	50
3.6	<i>comparison between energy lost computed with the acoustic Poynting vector formalism and the mechanical energy flux accross the anchors directly extracted from Comsol<sup>®</sup>.</i>	51
3.7	<i><math>Q</math> dependence on anchors dimensions. The results are from 3D simulations of short resonators exploiting the symmetry condition along their length. PMLs are included surrounding the released area.</i>	52
3.8	<i>comparison between the displacement induced at resonance with the best anchor configuration and the worst one. Displacements along <math>u</math>, <math>v</math> and <math>w</math> are compared together with the admittance responses vs frequency.</i>	54
3.9	<i>equivalent electrical circuit of the active and inactive region comprising the Si substrate surrounding the released area.</i>	55
3.10	<i>complete 3D model including the Si substrate and PML layers. The introduction of the surrounding substrate enables acoustic reflection at the edges of the released area, limiting the approximations introduced by fixed constraints and PMLs. The thin PMLs included at the top and bottom of the Si domains ensure partial absorption of acoustic energy by the surrounding substrates.</i>	56
3.11	<i>(a) energy lost through anchors computed with acoustic Poynting vector vs normalized anchor lengths (b) quality factor extracted from Comsol vs normalized anchor lengths. Both the energy variation and <math>Q</math> show the same periodicity as the analytical function <math>K(La)</math>.</i>	57
3.12	<i>first and zero order symmetric Lamb waves mode shapes.</i>	58
3.13	<i>simulated admittance response from a 2D model showing the (1.) <math>S_0</math>, (2.) <math>S_1</math> and (3.) <math>S_1</math> overtone excitation at different frequencies. The main contribution goes to the <math>S_1</math> (2.) resonance.</i>	59
3.14	<i><math>k_t^2</math> dependence on electrodes width and electrodes spacing in 2DMRs with Molybdenum electrodes. Results are presented for different ratio between the electrode and Aluminum Nitride thicknesses.</i>	60
3.15	<i><math>k_t^2</math> dependence on electrodes width and electrodes spacing in 2DMRs with Platinum electrodes. Results are presented for different ratio between the electrode and Aluminum Nitride thicknesses.</i>	61
3.16	<i>piezoelectric coupling factor for the <math>A_0</math>, <math>S_0</math> and <math>S_1</math> modes; the red point refers to the <math>k_x</math> related to the dilatational frequency of the <math>S_1</math> mode (<math>f_d</math>). These results have been evaluated from the dispersion curves derived from FEM 2D simulations.</i>	62
3.17	<i>2DMR mode shape observed for the optimal electrodes width and spacing combinations.</i>	63

3.18	<i>module of the admittance response vs frequency and phase for an optimized Mo/AlN 2DMR with <math>E.W. = 1 [\mu\text{m}]</math> and spacing = <math>2 [\mu\text{m}]</math> obtained from a 3D simulation. Electrical parameters extracted from the BVD model are listed in the inset. . . . .</i>	64
3.19	<i>simulated dispersion curves for active (AA) and inactive (IA) areas of a 2DMR with <math>AlN_t = 1 [\mu\text{m}]</math> and <math>Pt_t = 150 [\text{nm}]</math>. Continuous lines refer to AA whereas dotted lines refer to IA. . . . .</i>	65
3.20	<i>comparison of the stored energy density along the section of Pt/AlN 2DMRs with <math>EW = 0.8 [\mu\text{m}]</math> and different spacing values. Small and large spacings refer to minimum and maximum values included in the plots of fig.3.15. . . . .</i>	66
3.21	<i>resonance frequency dependence on the geometrical parameters of the electrode gratings. The colour refers to the magnitude of the electromechanical coupling coefficients. . . . .</i>	67
3.22	<i>2D FEM model of a 2DMR with a bottom plate electrode instead of patterned bottom electrodes. The mode shapes are similar to the one of classical 2DMRs. . . . .</i>	69
3.23	<i>computed <math>k_t^2</math> from simulations including different top and bottom electrode thicknesses. Results are showed for both Pt/AlN/Al and Pt/AlN/Mo configurations. . . . .</i>	70
3.24	<i>comparison of the acoustic impedance shown by different materials for longitudinal and vertical Lamb's waves in Aluminum Nitride thin films [1]. . . . .</i>	71
3.25	<i><math>k_t^2</math> dependence on top electrodes width and electrodes spacing for bottom plate 2DMRs with Platinum as both bottom and top electrodes material. The thickness ratio (<math>T.R. = 0.15</math>) expresses the ratio between the Pt films and the AlN thicknesses. . . . .</i>	71
3.26	<i>resonance frequency dependence on the geometrical parameters of the top electrodes in a bottom-plate Pt/AlN/Pt 2DMR; the thickness ratio between electrodes and piezoelectric film is <math>T.R. = 0.15</math>. The colour refers to the magnitude of the electromechanical coupling coefficients. . . . .</i>	72
3.27	<i>3D COMSOL<sup>®</sup> model of a 2DMR with irregular apodization applied to the fingers and total displacement shown at resonance. . . . .</i>	74
3.28	<i>total displacement shown at resonance of an optimized 2DMR taken as a reference for the apodization study. . . . .</i>	75
3.29	<i>sinusoidal apodization study on a non optimized 2DMR configuration. The curves are relative to four different sine aperture values. . . . .</i>	75
3.30	<i>2DMR with sinusoidal apodization applied to the fingers. "A" indicates the dimension that has been parametrically swept in simulations. . . . .</i>	76
3.31	<i>2DMR with circular apodization applied to the fingers. . . . .</i>	77

3.32	<i>simulated admittances for different apodization shapes adopted. The resonance and anti-resonance frequencies are shifted by the same amount, thus maintaining the <math>k_t^2</math> constant.</i>	78
4.1	<i>3D model of the two-ports device based on acoustically coupled 2DMRs. Terminal 1 is powered by an input signal whereas terminal 2 is left at a floating potential. Both terminals are terminated on user-defined impedances for simulations.</i>	80
4.2	<i>2D model of the two-ports device based on 2DMRs technology. In this example, <math>N1 &gt; N2</math>.</i>	81
4.3	<i><math>K^2</math> plot computed from the dispersive relations of the three fundamental modes extracted by COMSOL<sup>®</sup>.</i>	82
4.4	<i>displacement along Y and X directions at the 2DMR resonant frequency for an arc length including two active cells. The insets show the portion of the resonators included in the arc.</i>	82
4.5	<i>scattering parameters evaluated from COMSOL<sup>®</sup> 2D simulations with a real impedance termination (<math>R = 50 [\Omega]</math>). The <math>S_{21}</math> parameter shows a peak at the 2DMRs resonance frequency that is inversely proportional to the inactive area width.</i>	84
4.6	<i><math>S_{21}</math> peak value dependence on the inactive area width shown for narrow (a) and wide (b) gaps.</i>	85
4.7	<i>schematic of a two-port electrical network with load and source terminations.</i>	85
4.8	<i>input admittance seen from terminal 1 of the two-ports device obtained through 2D FEM simulations.</i>	86
4.9	<i>dependence of the electromechanical coupling coefficient on the width of the inactive area separating the two resonators. The periodicity is given by half-wavelength of the <math>S0</math> mode.</i>	87
4.10	<i>dependence of the quality factor at resonance (a) and quality factor at antiresonance (b) on the width of the inactive area separating the two resonators. Both parameters show a periodicity given by half wavelength of the <math>S0</math> mode.</i>	88
5.1	<i>process flow for the 2DMRs fabrication.</i>	90
5.2	<i>layout examples of 2DMRs. Numbers refer to the layers listed in the text.</i>	91
5.3	<i>layout of a 2-ports device comprising two 2DMRs with different number of fingers. Numbers refer to the layers listed in the text.</i>	92
5.4	<i>layout of a laterally anchored 2-ports device. Numbers refer to the layers listed in the text.</i>	92

5.5	<i>complete layout of the chip comprising all the resonators and testing structures for each layer. . . . .</i>	93
5.6	<i>process flow adopted by the Lincoln Laboratory for the 5[GHz] layout.</i>	94
5.7	<i>layout for the study of one and two ports AlN based 2DMRs with resonance frequency centered at 5 [GHz]. Multiports delay lines based on 2DMR<sup>M</sup> technology have been included. . . . .</i>	95
5.8	<i>layout for the study of one and two ports AlScN based 2DMRs with resonance frequency centered at 900 [MHz]. . . . .</i>	96
A.1	<i>2DMR layout example with different resistance contributions. . . . .</i>	104
A.2	<i>N<sub>p</sub> vs L<sub>e</sub> relation in a 1 [KΩ] matched 2DMR with 150 [μm] thick Pt electrodes and R<sub>s</sub> estimation. The R<sub>s</sub> dependence on the finger length shows an absolute minimum. . . . .</i>	105
A.3	<i>C<sub>0</sub> and R<sub>m</sub> dependence on the matching resistance in a 2DMR with 150 [μm] thick Pt electrodes. . . . .</i>	105
B.1	<i>portion of the Excel file listing the devices included in one of the experimental plans. . . . .</i>	110



# Chapter 1

## Introduction

### 1.1 RF MEMS resonators state of the art

The demand for more and faster data delivery in wireless mobile is encountering a drastic increase due to a multitude of applications enabled by smartphones and other new technologies. In response to this, new and tougher specifications for future RF front-end modules comprising oscillators, filters and multiplexers are required. Surface acoustic wave (SAW) filters based on piezoelectric substrates (e.g.,  $LiNbO_3$  or  $LiTaO_3$ ) have been in use since 1990s, but they suffer limited electromechanical performances due to the lack of acoustic energy constraint, especially in the vertical direction. Moreover, they rely on the excitation of *Rayleigh waves* that travel along the surface and are characterized by a relatively low phase velocity; because of this, SAW applications are commonly limited to frequencies below  $\approx 3$  [GHz]. In the last decade, piezoelectric micro-electro-mechanical (MEMS) resonators based on aluminum nitride (AlN) thin films have demonstrated the capability of forming high-performance filters owing to large piezoelectric coefficients and films quality [1]. The simplest devices are referred as film bulk acoustic resonators (FBARs) or, more generally, as bulk acoustic wave resonators (BAW) since they are based on the acoustic excitation of an extensional mode through their entire volume. They are composed of a piezoelectric layer sandwiched between a top and a bottom electrode and, owing to a simple and well defined energy constrained resonant cavity and to the excitation of a large piezoelectric coefficient, they stand out for very good performances and ease of fabrication. However, there is one main limitation of this technology that regards the monolithic integration of multi-band solutions. The center frequency of an FBAR is indeed set by the thickness of the film itself, which is usually uniform throughout the wafer. To solve this problem, a new class of resonators based on the excitation of Lamb waves has been introduced by research. Lamb waves are generally referred as plate waves and

describe the characteristics of acoustic waves propagating in an infinite ideal plate with free boundaries. They can be excited in a finite piezoelectric structure by interdigital transducers (IDTs) or, more generally, by electrode gratings disposed in specific configurations to match the acoustic wavelength of the modes. Thanks to the dependence of the resonance frequency on the electrodes dimensions, Lamb wave resonators can solve the monolithic integration issue that affects FBARs by lithographically setting the acoustic wavelength. However, common AlN Lamb wave resonators usually show moderate efficiency in the conversion of electrical energy into mechanical (and viceversa) if compared to BAWs. As a result, research has been looking at several electrodes typologies and configurations to boost the resonator performances towards the replacement of FBARs. While searching for the most efficient architecture, several technologies have been introduced following three main approaches:

- the excitation of lateral waves coupled with vertical waves
- the excitation of two dimensional lateral waves
- the coupling of 2D lateral waves with vertical waves

Following the first approach, cross-sectional Lamé mode resonators (CLMRs), laterally coupled alternating thickness mode resonators (LCAT), coupled bulk acoustic resonators (CBARs) and two dimensional resonant rods (2DRR) have been designed together with the devices at the core of this work, the so called *two-dimensional mode* resonators (2DMRs). Each design differs from the others by the polarity of the voltage applied to the electrodes, their dimensions and thicknesses, resulting in the direct excitation of different piezoelectric coefficients of the Aluminum Nitride film. They all have different merits and limitations in terms of electromechanical performances, spurious modes minimization and easy of fabrication. Together with these main features, other important parameters such as the power handling and form factor (i.e. size of the resonator) should be taken into account when selecting one typology for a specific circuital application. Since several technical aspects and details are needed for a full comparison between the multitude of devices, their analysis is carried out in the next chapter.

With the idea of exploiting two lateral waves, Checker Mode resonators are currently in investigation, where lateral waves along two perpendicular directions are excited by pads with rectangular or diamond shapes instead of long IDTs. However, very thin electrical lines are needed in this case, imposing a significant electrical loading to the system. For this reason, and considering the more complex manufacturing process, most of research focus is on other technologies.

The performances of all these MEMS resonators deeply rely on the properties of the piezoelectric material adopted (i.e. AlN), which governs the ability to cyclically convert energy from the mechanical to the electrical domain. It has been recently

demonstrated that Scandium doping of Aluminum Nitride thin films increases the piezoelectric coefficients [2],[3], therefore boosting the performances obtained with pure AlN regardless of the design implemented. Moreover, the Scandium introduction gives a ferroelectric property to the piezoelectric material, introducing an additional feature for the next generation of MEMS resonators for RF applications. In this thesis, the optimization of the design of two-dimensional mode resonators based on pure AlN is carried out. All the work has been done in the Microsystems Radio Frequency laboratory of prof. Cristian Cassella (<https://web.northeastern.edu/cassella/research/>), who recently patented both CLMRs and 2DMRs. In the following subchapters, the fundamentals of the theory needed to understand the physics, design and development of a MEMS resonator are explained.

## 1.2 From piezoelectricity to RF resonators

### 1.2.1 Piezoelectric materials for RF MEMS

As the word itself says, the piezo-electric effect (from the Greek *piezein*, to squeeze or press) is an **electro-mechanical** phenomenon. It was first proven in 1880 by the brothers Pierre and Jacques Curie. They demonstrated how the piezoelectric crystals exhibit a dipole moment whose strength and orientation can be changed by mechanical forces. Experimentally, it was observed how these materials are able to generate an electric charge in response to an applied mechanical interaction. At equilibrium, without any external stress, the negative and positive charges of each molecule of the material share the same symmetry centres and the electric effects are reciprocally cancelled, resulting in an electrically neutral molecule. When an external mechanical pressure is applied, the internal atomic structure is deformed, resulting in a separation of the positive and negative centres of the molecules, as depicted in fig.1.1.

The consequent generation of dipoles maps the phenomenon of energy conversion from the mechanical domain to the electrical and when the material is not short-circuited, the charges induce a measurable voltage across the material. Moreover, an equivalent behaviour is observed in the reverse direction, where the application of a voltage induces a mechanical deformation. This peculiar effect is nowadays exploited in many devices for radio-frequency applications, sensor and actuators of many kinds [4]. Among all these applications, we will investigate the evolution and the state-of-the-art of micro-scaled piezoelectric resonating structures.

Resonators and piezo generators for ultrasound applications were two of the first demonstrated MEMS devices. Among the piezoelectric materials, Lithium Niobate ( $LiNbO_3$ ) has historically gained interest in the late 1960s in the world of surface acoustic wave (SAW) to provide excellent piezoelectric properties in many applications where the acoustic domain was exploited for analog signal processing purposes.

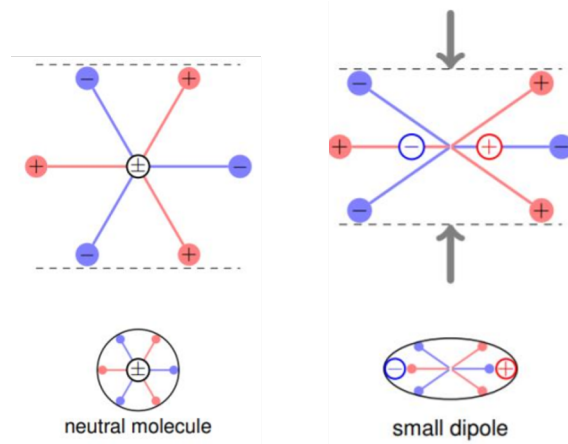


**Figure 1.1:** *positive and negative charges centres relative position in a molecule of a piezoelectric material without and in the presence of an external applied stress.*

Subsequently, in the 1970s and 1980s, the most investigated thin film materials were mainly ZnO and AlN. Due to their non-centrosymmetric wurtzite structures (i.e., without any inversion symmetry), these compounds are capable of exhibiting better mechanical performance at high-frequency operation if compared to other technologies. Following the fast growing of the mobile and telecommunication industry in the mid 1990s,  $LiNbO_3$  was again considered to compete with the AlN film bulk acoustic resonators (FBARs) technology thanks to the simultaneous delivery of high electromechanical coupling ( $kt^2$ ) and mechanical quality factor (Q). However, one fundamental aspect that goes in favor of Aluminum Nitride at the expense of other compounds, is the integration and process compatibility with CMOS related processes.

Today, AlN is the material of choice for most of RF devices that rely on piezoelectricity for mainly three reasons. Firstly, the strong polarity of the crystalline structure allows for a stable piezoelectric response in time. Secondly, the deposition process of AlN films is reliable and reproducible and finally, the material itself exhibits a good thermal conductivity for an insulator and is thus suited for filtering applications [4]. As common with many nitrides, AlN is characterized by a high hardness and large stiffness constants. The relevant piezoelectric coefficient ( $e_3 = 1.55 C/m^2$ ) is about ten times lower than in PZT thin films, but this is compensated by a very low dielectric constant, enabling a high electromechanical coupling coefficient for thickness extensional modes. Furthermore, a rather specific feature of AlN is its high sound velocity [5]. This permits to deposit thick films even for relatively high frequencies, overcoming process limitations common to other materials.

## 1.3 Piezoelectricity and Elastodynamics

### 1.3.1 Piezoelectricity constitutive equations

When an external force is applied to a solid, it deforms. If the original state of the structure can be restored, the deformation is said to be elastic, as opposite to the plastic permanent deformation. There are two main kinds of deformation, the first comprises extension and compression of a structure and the second is shear, they are schematized in fig.1.2. In both cases, a measure of the deformation can be

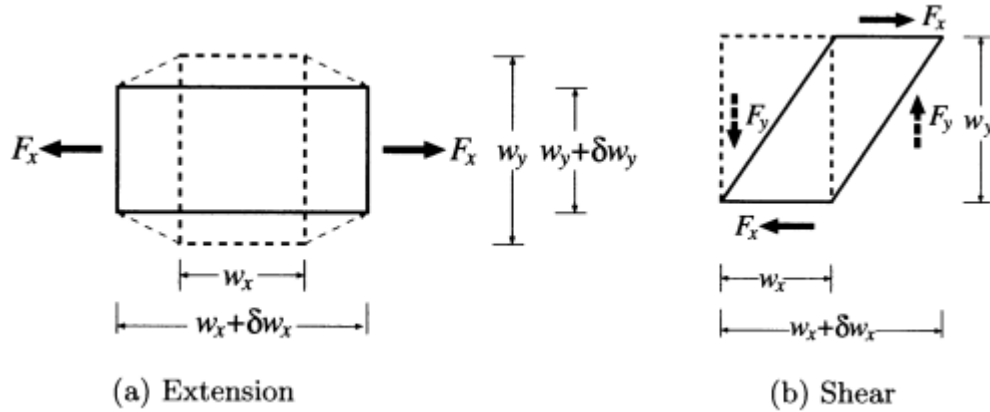


Figure 1.2: deformation in solids, figure from [6].

given by

$$S'_{ij} = \frac{\delta w_i}{\delta w_j} = \frac{\partial u_i}{\partial x_j} \quad (1.1)$$

where  $\mathbf{u}$  is the displacement vector of a point in the structure. To overcome the sensitivity of  $S'_{ij}$  to rotational displacement, the *strain* can be defined as [6]

$$S_{ij} = \frac{1}{2} \left( \frac{\partial u_i}{\partial x_j} + \frac{\partial u_j}{\partial x_i} \right) \quad (1.2)$$

so that to positive and negative values corresponds, respectively, extension and compression. Given the symmetry of eq.1.2, the matrix  $\mathbf{S}$  composed by nine elements shows only six independent values and a more compacted form of the definition given above can be written:

$$\mathbf{S} = \nabla \mathbf{u}, \quad (1.3)$$

where

$$\mathbf{S} = \begin{pmatrix} S_1 \\ S_2 \\ S_3 \\ S_4 \\ S_5 \\ S_6 \end{pmatrix}, \quad \nabla = \begin{pmatrix} \frac{\partial}{\partial x_1} & 0 & 0 \\ 0 & \frac{\partial}{\partial x_2} & 0 \\ 0 & 0 & \frac{\partial}{\partial x_3} \\ 0 & \frac{\partial}{\partial x_3} & \frac{\partial}{\partial x_2} \\ \frac{\partial}{\partial x_3} & 0 & \frac{\partial}{\partial x_1} \\ \frac{\partial}{\partial x_2} & \frac{\partial}{\partial x_1} & 0 \end{pmatrix}, \quad \mathbf{u} = \begin{pmatrix} u_1 \\ u_2 \\ u_3 \end{pmatrix}$$

and the following relation holds :

$$\begin{pmatrix} S_1 & S_6 & S_5 \\ S_6 & S_2 & S_4 \\ S_5 & S_4 & S_3 \end{pmatrix} = \begin{pmatrix} S_{11} & 2S_{12} & 2S_{13} \\ 2S_{12} & S_{22} & 2S_{23} \\ 2S_{13} & 2S_{23} & S_{33} \end{pmatrix}. \quad (1.4)$$

In order to describe the relation between the strain and the force applied to a plane of the structure, the stress  $T_{ij}$  is defined. It represents the force per unit of area, where the subscripts indicate the directions of the force and the vector perpendicular to the plane where the force is applied [6]. In a stationary framework, the equilibrium conditions for translation and rotation give

$$T_{ij} = T_{-i-j} \quad \text{and} \quad T_{ij} = T_{ji}. \quad (1.5)$$

Similarly to eq.1.2, eq.1.5 above infers only six independent element among the nine of type  $T_{ij}$ . When an elastic response is excited, the stress is proportionally related to the strain by the Hooke's law, it can be written with an abbreviated notation as

$$\mathbf{T} = \mathbf{cS}, \quad (1.6)$$

where

$$\mathbf{T} = \begin{pmatrix} T_1 \\ T_2 \\ T_3 \\ T_4 \\ T_5 \\ T_6 \end{pmatrix}, \quad \mathbf{c} = \begin{pmatrix} c_{11} & c_{12} & c_{13} & c_{14} & c_{15} & c_{16} \\ c_{12} & c_{22} & c_{23} & c_{24} & c_{25} & c_{26} \\ c_{13} & c_{23} & c_{33} & c_{34} & c_{35} & c_{36} \\ c_{14} & c_{24} & c_{34} & c_{44} & c_{45} & c_{46} \\ c_{15} & c_{25} & c_{35} & c_{45} & c_{55} & c_{56} \\ c_{16} & c_{26} & c_{36} & c_{46} & c_{56} & c_{66} \end{pmatrix}, \quad \mathbf{S} = \begin{pmatrix} S_1 \\ S_2 \\ S_3 \\ S_4 \\ S_5 \\ S_6 \end{pmatrix}.$$

$c_{ij}$  is called the *elastic constant* and the number of independent elements in  $\mathbf{c}$  depends on the crystallographic structure of the solid under interest. When a coordinate system that coincides with the crystal axes of a 6mm material (e.g,

AIN), is chosen, the stiffness matrix reduces to

$$\mathbf{c} = \begin{pmatrix} c_{11} & c_{12} & c_{13} & 0 & 0 & 0 \\ c_{12} & c_{11} & c_{13} & 0 & 0 & 0 \\ c_{13} & c_{13} & c_{33} & 0 & 0 & 0 \\ 0 & 0 & 0 & c_{44} & 0 & 0 \\ 0 & 0 & 0 & 0 & c_{44} & 0 \\ 0 & 0 & 0 & 0 & 0 & c_{66} \end{pmatrix} \quad (1.7)$$

and the relation  $c_{11} - c_{12} = 2c_{66}$  holds [6].

When it comes to apply the same relations for a piezoelectric medium, the contribution of the applied electric field to the stress has to be taken into account and vice versa. The strain  $\mathbf{S}$  is linearly coupled to the electric flux density  $\mathbf{D}$  by the so called *piezoelectric stress constants*  $e_{ij}$  and the following *stress-charge* relations holds:

$$\begin{pmatrix} D_1 \\ D_2 \\ D_3 \end{pmatrix} = \begin{pmatrix} e_{11} & e_{12} & e_{13} & e_{14} & e_{15} & e_{16} \\ e_{21} & e_{22} & e_{23} & e_{24} & e_{25} & e_{26} \\ e_{31} & e_{32} & e_{33} & e_{34} & e_{35} & e_{36} \end{pmatrix} \begin{pmatrix} S_1 \\ S_2 \\ S_3 \\ S_4 \\ S_5 \\ S_6 \end{pmatrix} + \begin{pmatrix} \epsilon_{11}^S & \epsilon_{12}^S & \epsilon_{13}^S \\ \epsilon_{12}^S & \epsilon_{22}^S & \epsilon_{23}^S \\ \epsilon_{13}^S & \epsilon_{23}^S & \epsilon_{33}^S \end{pmatrix} \begin{pmatrix} E_1 \\ E_2 \\ E_3 \end{pmatrix} \quad (1.8a)$$

$$\begin{pmatrix} T_1 \\ T_2 \\ T_3 \\ T_4 \\ T_5 \\ T_6 \end{pmatrix} = \begin{pmatrix} c_{11}^E & c_{12}^E & c_{13}^E & c_{14}^E & c_{15}^E & c_{16}^E \\ c_{12}^E & c_{22}^E & c_{23}^E & c_{24}^E & c_{25}^E & c_{26}^E \\ c_{13}^E & c_{23}^E & c_{33}^E & c_{34}^E & c_{35}^E & c_{36}^E \\ c_{14}^E & c_{24}^E & c_{34}^E & c_{44}^E & c_{45}^E & c_{46}^E \\ c_{15}^E & c_{25}^E & c_{35}^E & c_{45}^E & c_{55}^E & c_{56}^E \\ c_{16}^E & c_{26}^E & c_{36}^E & c_{46}^E & c_{56}^E & c_{66}^E \end{pmatrix} \begin{pmatrix} S_1 \\ S_2 \\ S_3 \\ S_4 \\ S_5 \\ S_6 \end{pmatrix} - \begin{pmatrix} e_{11} & e_{21} & e_{31} \\ e_{12} & e_{22} & e_{32} \\ e_{13} & e_{23} & e_{33} \\ e_{14} & e_{24} & e_{34} \\ e_{15} & e_{25} & e_{35} \\ e_{16} & e_{26} & e_{36} \end{pmatrix} \begin{pmatrix} E_1 \\ E_2 \\ E_3 \end{pmatrix} \quad (1.8b)$$

that in matrix form reads

$$\mathbf{D} = \mathbf{e}\mathbf{S} + \boldsymbol{\epsilon}^S \mathbf{E} \quad (1.9a)$$

$$\mathbf{T} = \mathbf{c}\mathbf{S} - \mathbf{e}^t \mathbf{E} \quad (1.9b)$$

The superscript  $S$  in eqs.1.9a and 1.8 indicates that the value of the dielectric constants are measured under constant strain. As for the case of the elastic constants, both the piezoelectric and dielectric constant matrices can be simplified

for specific crystallographic orientations. In the case of the hexagonal point symmetry 6mm of Aluminum Nitride, only five coefficients are inferred:

$$\mathbf{e} = \begin{pmatrix} 0 & 0 & 0 & 0 & e_{15} & 0 \\ 0 & 0 & 0 & e_{15} & 0 & 0 \\ e_{31} & e_{31} & e_{33} & 0 & 0 & 0 \end{pmatrix}, \quad \epsilon^S = \begin{pmatrix} \epsilon_{11}^S & 0 & 0 \\ 0 & \epsilon_{11}^S & 0 \\ 0 & 0 & \epsilon_{33}^S \end{pmatrix} \quad (1.10)$$

The values of these coefficients for a single crystal of Aluminum Nitride are listed in table 1.1 . Alternatively to eq.1.9, the piezoelectric relations can be expressed in a *strain-charge* form:

$$\mathbf{S} = \mathbf{s}^{E=0} \mathbf{T} + \mathbf{d}^T \mathbf{E} \quad (1.11a)$$

$$\mathbf{D} = \mathbf{d} \mathbf{T} + \epsilon^{T=0} \mathbf{E}, \quad (1.11b)$$

being  $\mathbf{s}^{E=0}$  the *compliance* matrix (inverse of the stiffness matrix) and  $\mathbf{d}$  the *piezoelectric coefficients* matrix.

AlN coefficients	
$c_{11}^E = c_{22}^E$ [GPa]	345
$c_{12}^E$ [GPa]	125
$c_{13}^E$ [GPa]	120
$c_{33}^E$ [GPa]	395
$c_{44}^E = c_{55}^E$ [GPa]	118
$e_{15}$	-0.48
$e_{31}$	-0.58
$e_{33}$	1.55
$\epsilon_{11}^S / \epsilon_0$	9.0
$\epsilon_{33}^S / \epsilon_0$	10.7

**Table 1.1:** *measured properties of single crystal AlN* [4].

### 1.3.2 Fundamentals of elastodynamics

To understand how a solid deforms given a stress configuration, the equation of motion defining the elastodynamics of the system has to be solved:

$$\nabla \cdot \mathbf{T} + \mathbf{f} = \rho \ddot{\mathbf{u}}, \quad (1.12)$$

where  $\mathbf{T}$  is the stress tensor,  $\mathbf{f}$  represents the mechanical body forces,  $\rho$  is the mass density of the domain and  $\ddot{\mathbf{u}}$  is the second time derivative of the mechanical displacement. For what concerns the electrical response of a piezoelectric material,

it is often analyzed under the *quasi-static* regime of electromagnetic fields. Within this approximation, it is assumed that the electric field changes in time sufficiently slowly in the domain volume so that no magnetic field can be taken into account and purely electrostatic equations can be used. This assumption relies on the fact that the size of the devices is most of the times much shorter than the electromagnetic wavelength.

In an elastic medium, the solution of the equation of motion can lead to propagating or stationary waves. These can be described in terms of stress, displacement or strain and divide in two main groups:

- *Longitudinal waves*, where the displacement is parallel to the propagation direction
- *Shear/Transversal waves*, where the displacement is perpendicular to the direction of propagation

As it will be further discussed, these two families of waves are characterized by different velocities, even if they propagate within the same medium. Transverse waves usually present lower velocities than the longitudinal waves, this results also in a lower acoustic impedance, defined as:

$$Z = v \cdot \rho, \tag{1.13}$$

being  $v$  the sound velocity in the medium and  $\rho$  its density. The acoustic impedance relates variations in stress to those in the velocity of the particles and it is fundamental to describe the behaviour of a wave when it has to propagate in non-homogeneous structures such as a MEMS resonator.

When a mechanical wave propagates in a piezoelectric material, electrical energy created by the motion is stored by local electric fields. The piezo interaction results in an enhancement of the effective stiffness coefficient and this is referred as *piezo-stiffening*. Being the effective stiffness coefficient higher than the nominal one, the sound velocity is increased:

$$v = \sqrt{c_D/\rho} = \sqrt{c^E(1 + k_t^2)/\rho} = v_u \sqrt{1 + k_t^2} \tag{1.14}$$

where the sound velocity is expressed in terms of the material stiffness  $c_E$  (evaluated with shorted boundaries), and the stiffened coefficient evaluated with floating boundaries  $c_D$ . Here, the  $k_t^2$  is called the electromechanical coupling coefficient and is derived from a combination of all the piezoelectric coefficients involved in the mechanical and electrical energy conversion.

In the case of a MEMS resonator, the equation of motion is solved for a bounded geometry, giving solutions in the form of *standing waves*. These solutions obey to the boundary conditions applied to all the edges of the structure and form

through multiple wave reflections between the device surfaces. Like the propagating waves, the standing waves divide in shear and longitudinal resonances, where the displacement field polarization in the first case is orthogonal to the latter one. A solution to the problem of waves propagation in plates has been analytically derived by Horace Lamb in 1916; part of the derivation is summarized below because of the centrality of the results in the design of Lamb waves resonators.

### 1.3.3 Lamb wave theory

Each resonator typology distinguish itself from others by the *guided wave modes* that are excited when putting the structure into resonance. A tool for the investigation of how the ultrasonic energy is confined and travels inside a thin film of a piezoelectric material comes from the study of the most generic *free plate* problem. Even though the 2DMR geometry is far from the one of a free plate, each region of the structure can be approximately thought as a portion of a multilayered film with boundary conditions applied at its edges. The analysis of the modes that can be excited in the ideal case of an infinitely extended plate can be useful to derive the characteristic of standing waves in a finite resonator volume.

In an isotropic, homogeneous and ideal plate as the one showed in fig.1.3, acoustic waves can be described in a cartesian tensor notation as:

$$\mu \cdot u_{i,jj} + (\lambda + \mu) \cdot u_{j,ji} + \rho \cdot f_i = \rho \cdot \ddot{u}_i \quad (i, j = 1,2,3), \quad (1.15)$$

where  $f_i$  and  $u_i$  are the body force and displacement along the  $x_i$  direction,  $\mu$  and  $\rho$  are the shear modulus and the density of the plate and  $\lambda$  is the Lamé constant, related to the Poisson's ration ( $\nu$ ) by  $\lambda = \frac{2\mu\nu}{1-2\nu}$  [7]. Eq.1.15 contains all the partial differential equations governing the displacement. If the domain in which they are applied is finite, boundary conditions (BC) are needed to solve a well posed Cauchy problem. The BCs take the form of defined tractions and/or displacements at the boundaries of the structure and, in the case under study, the surfaces of the plate in fig.1.3 are assumed to be traction-free.

According to Helmholtz's theorem, any vector field  $\mathbf{u}$  can be represented in terms of a vector potential  $\Psi$  and a scalar potential  $\phi$ :

$$\mathbf{u} = \nabla\phi + \nabla \times \Psi \quad \text{if} \quad \nabla \times \phi = 0 \quad \text{and} \quad \nabla \cdot \Psi = 0, \quad (1.16)$$

where a scalar potential field that is curl-free (i.e. no shearing is derived) and a vector potential field that is divergent-free (i.e. no volume change is inferred) are inferred.

Considering a section of the plate in fig.1.3 along the  $x_1/x_3$  plane, eq.1.15 can be uncoupled in two parts following eq.1.16. They are respectively referring to the *longitudinal* wave modes and the *transverse* or *shear* wave modes:

$$\frac{\partial^2 \phi}{\partial x_1^2} + \frac{\partial^2 \phi}{\partial x_3^2} = \frac{1}{c_L^2} \frac{\partial^2 \phi}{\partial t^2}, \quad \text{for longitudinal waves} \quad (1.17)$$

$$\frac{\partial^2 \Psi}{\partial x_1^2} + \frac{\partial^2 \Psi}{\partial x_3^2} = \frac{1}{c_T^2} \frac{\partial^2 \Psi}{\partial t^2}, \quad \text{for shear waves} \quad (1.18)$$

Under the simplistic assumption of plane strain, the displacements and stresses can be described by potentials as:

$$\begin{aligned} u_1 = u &= \frac{\partial \phi}{\partial x_1} + \frac{\partial \Psi}{\partial x_3} \\ u_2 = v &= 0 \\ u_3 = w &= \frac{\partial \phi}{\partial x_3} + \frac{\partial \Psi}{\partial x_1} \end{aligned} \quad (1.19)$$

$$T_{31} = \mu \left( \frac{\partial u_3}{\partial x_1} + \frac{\partial u_1}{\partial x_3} \right) = \mu \left( \frac{2\partial^2 \Psi}{\partial x_1 \partial x_3} - \frac{\partial^2 \Psi}{\partial x_1^2} + \frac{\partial^2 \Psi}{\partial x_3^2} \right) \quad (1.20)$$

$$T_{33} = \lambda \left( \frac{\partial u_1}{\partial x_1} + \frac{\partial u_3}{\partial x_3} \right) + 2\mu \frac{\partial u_3}{\partial x_3} = \lambda \left( \frac{\partial^2 \Psi}{\partial x_1^2} + \frac{\partial^2 \Psi}{\partial x_3^2} \right) + 2\mu \left( \frac{\partial^2 \Psi}{\partial x_3^2} - \frac{\partial^2 \Psi}{\partial x_1 \partial x_3} \right) \quad (1.21)$$

where  $\lambda$  and  $\mu$  are Lamé constants [8].

Given the equations of motion (eq.1.17 and eq.1.18), it is reasonable to assume infinite plane harmonic wave solutions in the form:

$$\phi = \Phi(x_3) \exp[i(kx_1 - \omega t)] \quad (1.22)$$

$$\Psi = \Psi(x_3) \exp[i(kx_1 - \omega t)] \quad (1.23)$$

which describe traveling waves in the  $x_1$  direction with wave vector  $k = 2\pi/\lambda_{x1}$  and standing waves along  $x_3$ . Substituting the last equations in 1.17 and 1.18, the equations governing the unknown functions can be derived:

$$\phi = \Phi(x_3) = A_1 \sin(px_3) + A_2 \cos(px_3) \quad (1.24)$$

$$\Psi = \Psi(x_3) = B_1 \sin(qx_3) + B_2 \cos(qx_3) \quad (1.25)$$

where the parameters  $p$  and  $q$  are dependent on the wavelength of the wave:

$$p^2 = \frac{\omega^2}{c_L^2} - k^2, \quad q^2 = \frac{\omega^2}{c_T^2} - k^2 \quad k = \frac{2\pi}{\lambda_{wave}} \quad (1.26)$$

The four constants  $A_1$ ,  $A_2$ ,  $B_1$  and  $B_2$  are determined by the boundary conditions of the system.  $c_L$  and  $c_T$  are the velocities of longitudinal and transverse modes, defined by [7]:

$$c_L = \sqrt{\frac{E(1-\nu)}{\rho(1+\nu)(1-\nu)}} = \sqrt{\frac{2\mu(1-\nu)}{\rho(1-2\nu)}}, \quad c_T = \sqrt{\frac{E}{2\rho(1+\nu)}} = \sqrt{\frac{\mu}{\rho}}, \quad (1.27)$$

being  $E$  the Young's modulus of the material. From the solution of the potentials, the displacements and stresses can be obtained by substitution in eqs.1.19,1.20,1.21:

$$u_1 = \left( ik\phi + \frac{d\Psi}{dx_3} \right) \quad (1.28)$$

$$u_3 = \left( \frac{d\Psi}{dx_3} + ik\Psi \right) \quad (1.29)$$

$$T_{31} = \mu \left( 2ik \frac{d\phi}{dx_3} + k^2\Psi + \frac{d^2\Psi}{dx_3^2} \right) \quad (1.30)$$

$$T_{33} = \lambda \left( -k^2\phi + \frac{d^2\phi}{dx_3^2} \right) + 2\mu \left( \frac{d^2\phi}{dx_3^2} - ik \frac{d\Psi}{dx_3} \right) \quad (1.31)$$

where the exponential terms have been omitted to simplify the expressions. The plate under study has free upper and lower surfaces, therefore the following boundary conditions can be applied to the system:

$$\begin{aligned} u(x, t) &= u_0(x, t) \\ t_i &= T_{ji}n_j \\ T_{31} = T_{33} &= 0 \quad \text{at } x_3 = \pm h \end{aligned} \quad (1.32)$$

giving

$$\frac{\tan(qh)}{\tan(ph)} = \frac{4k^2qp\mu}{(\lambda k^2 + \lambda p^2 + 2\mu p^2)(k^2 - q^2)} \quad (1.33)$$

Eq.1.33 gives the most general description of Lamb waves propagating in an isotropic and homogeneous suspended plate and a few considerations can be done. Substituting eqs.1.26, 1.27 in the last expression and considering the symmetric and anti-symmetric properties of the trigonometric functions involved, two parts with exclusively *symmetric* and *anti-symmetric* properties can be distinguished. Two types of Lamb waves modes can therefore be derived and eq.1.33 splits in:

$$\frac{\tan(qh)}{\tan(ph)} = -\frac{4k^2qp}{(k^2 - q^2)^2} \quad \text{asymmetric modes} \quad (1.34)$$

$$\frac{\tan(qh)}{\tan(ph)} = -\frac{(k^2 - q^2)^2}{4k^2qp} \quad \text{symmetric modes} \quad (1.35)$$

The symmetric and anti-symmetric Lamb modes are commonly named with the symbols  $S_i$  and  $A_i$  ( $i = 0, 1, \dots$ ) and eqs.1.34,1.35 are known as the *Rayleigh-Lamb equations*. These frequency relations can be used to determine the velocity at which a wave of a particular frequency propagates within the plate [8] and the frequency dependence on the wave vector  $k$  of the mode. The latter relation defines the *dispersion curves* that are unique for each mode and play a central role in the design of 2DMRs.

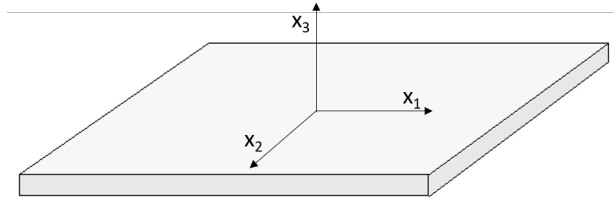


**Figure 1.3:** *infinite plate assumed for the derivation of the Lamb theory.*

The conventional way to compute dispersion curves for homogeneous acoustic waveguides is to implement the Semi-Analytical Finite Element (SAFE) method. On the other hand, another powerful tool to achieve the same results relies on the usage of *Floquet boundary conditions*. These boundary conditions can be used to extract dispersion curves of periodic waveguides, that typically characterize metamaterials and periodic architectures. For an infinite-plate waveguide, the Floquet boundaries can be expressed as:

$$\mathbf{u}_{dst} = \mathbf{u}_{src} e^{-i\mathbf{k}_F(\mathbf{r}_{dst} - \mathbf{r}_{src})} \quad (1.36)$$

where the wavenumber  $\mathbf{k}_F$  can be user-defined in a FEM analysis software and is usually swept in a relatively wide range. The subscripts *dst* and *src* designate the destination and source faces of a given material stack,  $\mathbf{u}$  is the displacement and  $\mathbf{r}$  describes the coordinates of the boundaries on which the BC is applied [9]. In this work, a unit cell formed by the same materials stack of specific regions inside the devices structure has been simulated on COMSOL® Multiphysics and the Floquet BC have been applied to its parallel lateral faces as depicted in fig.1.4. The eigenvalues (i.e. frequencies) associated to Lamb's eigenfunctions are evaluated by sweeping the wavenumber  $\mathbf{k}_F$ , and dispersion curves for the waveguides are drawn by plotting the wavenumber versus frequency, or viceversa. These dispersion curves typically appear periodic with respect to wavenumber with periodicity  $2\pi/d$ , being  $d$  the width of the unit cell (i.e. the distance between the parallel *src* and

*dst* faces). The first zone of the reciprocal lattice-space ( $-\frac{\pi}{d} < k_F < \frac{\pi}{d}$ ) is usually assumed as the focal point because the dispersion curves repeats themselves in the other zones.

For the complete analysis of the excited modes carried out in the following chapters, dispersion curves have been computed applying different electrical boundaries at the interface between the metal and the piezoelectric layer. If zero-charge boundaries are imposed, the equivalent stiffness of the piezoelectric layer is reduced because less energy gets stored in the electrical domain, and higher frequencies are obtained. In the opposite case of floating surfaces, the layer equivalent stiffness is increased and lower frequencies vs  $k_x$  are plotted, as visible in fig.1.4. These two configurations corresponds to the antiresonance and resonance frequency characterizing the electrical response of a piezoelectric resonator as will be explained in detail in the following subsection.

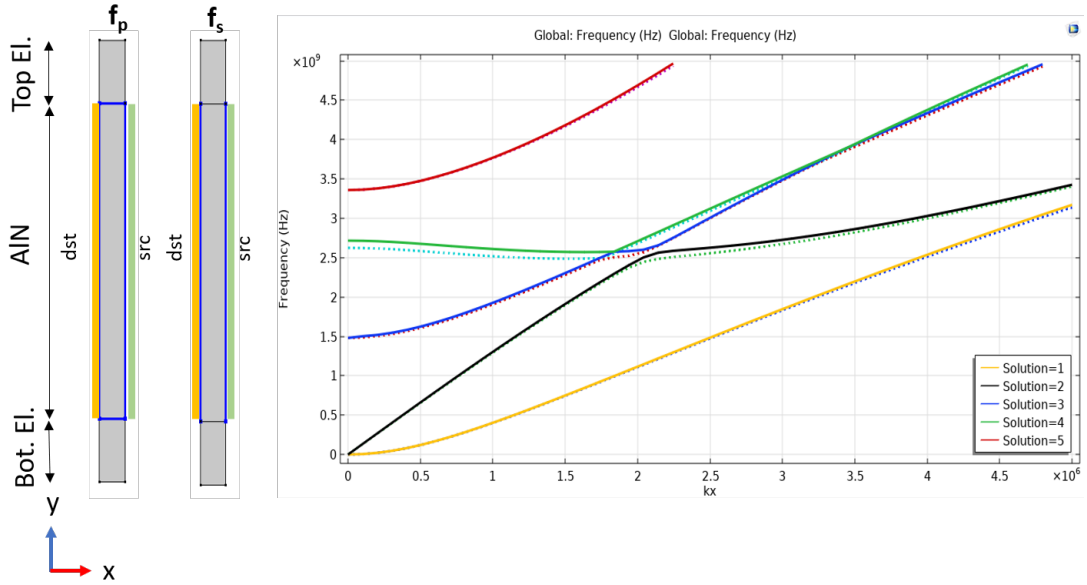


**Figure 1.4:** 2D model of a multilayered structure used for the evaluation of the dispersion curves for both the parallel and series resonances. The blue lines indicates the zero charge boundaries whereas the green and yellow lines indicate, respectively, the source and destination boundaries for the Floquet periodicity. The dispersion curves for the first five excited modes are also shown, where the dotted lines are related to  $f_s$  curves and solid lines to  $f_p$ .

### 1.3.4 Resonators and BVD model

When a piezoelectric resonator is excited in one of its acoustic resonant modes by the application of voltages in specific locations through metallic electrodes, the resonance can be detected as a change in the input admittance of the device. This behaviour is at the base of all the applications in which MEMS resonators are used as impedance elements in an electronic system. Let's take the most simple BAW resonator (FBAR) as the case study to derive an electrical model that can be applied to any kind of resonant system. In the structure shown in fig.1.5a), when a sinusoidal voltage signal  $v$  is applied between top and bottom electrodes, a mechanical force  $v_m$  is generated through piezoelectric effect and a displacement  $u$  is generated in the plate. The following relation holds:

$$v \propto v_m = M \frac{d^2 u}{dt^2} + \nu \frac{du}{dt} + Ku, \quad (1.37)$$

being  $M$ ,  $\nu$ , and  $K$  the effective mass, effective viscosity and effective spring constant of the plate. In terms of a damped oscillating system, the three terms correspond to inertia, friction and elasticity. Thanks to the piezoelectricity, electrical charges  $q_m$  proportional to the induced displacement accumulate on the electrodes; from these mechanical/electrical relations, the electromechanical equivalent circuit of fig.1.5b) can be derived where the current  $i_m = du/dt$  is a "mechanical" current and  $C_0$  is the capacitance expressing the electrostatic coupling between two electrodes [4].

If only the electrical characteristic is taken into account, the circuit can reduce to

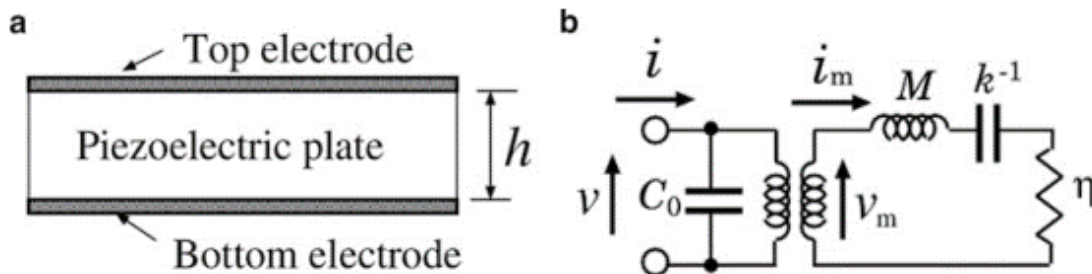


**Figure 1.5:** a) *simplified FBAR structure* b) *equivalent electrical model of a resonator*

the one in fig.1.6(a), where  $C_m$ ,  $L_m$ , and  $R_m$  are called the *motional capacitance*, *motional inductance* and *motional resistance* of the system. This circuitual model is called the Butterworth-Van Dyke (**BVD**) model. This is the most simple circuit describing a one port acoustic resonators and will be used to characterize simulation and experimental results in the following chapters.

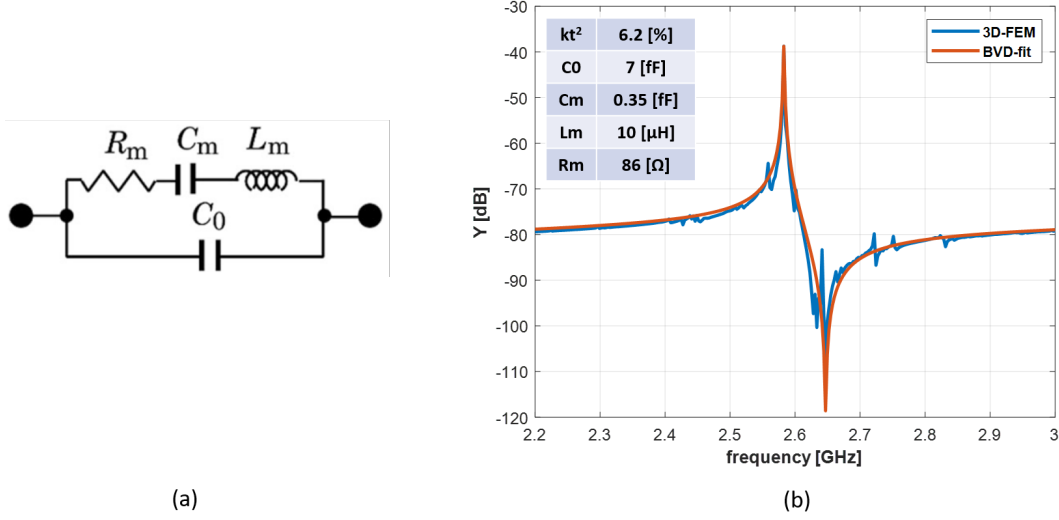


**Figure 1.6:** a) single resonance BVD model b) BVD model fitting of a 3D FEM simulation, the electrical parameters are listed in the inset.

A typical response of the input admittance versus frequency obtained from a 3D FEM simulation is shown in fig.1.6(b); the curve has been fitted with the BVD model and the electrical parameters are summarized in the inset. The frequency at which the admittance is maximum is called the *series resonance frequency* labelled as  $f_s$  whereas the frequency at the minimum is called the *parallel resonance frequency*  $f_p$ . From the electrical model, the admittance can be expressed as [4]:

$$Y = 2\pi j f C_0 \frac{1 - (f/f_p)^2 + j(f/f_p)Q_a^{-1}}{1 - (f/f_s)^2 + j(f/f_s)Q_r^{-1}} \quad (1.38)$$

where  $Q_r$  and  $Q_a$  are the resonance and anti-resonance quality factors. As will be discussed in detail, they are related to the steepness of the admittance peaks and are inversely proportional to the motional resistance. They can be computed as

$$Q_r = \frac{2\pi f_s L_m}{R_m} \quad (1.39a)$$

$$Q_a = \frac{2\pi f_p L_m}{R_m} \quad (1.39b)$$

and the the resonance and anti-resonance frequencies are evaluated as

$$f_s = \frac{1}{2\pi\sqrt{L_m C_m}} \quad (1.40a)$$

$$f_p = \frac{1}{2\pi\sqrt{L_m(C_m^{-1} + C_0^{-1})^{-1}}}. \quad (1.40b)$$

Given the electromechanical coupling coefficient ( $k_t^2 = \pi^2/8(f_p^2 - f_s^2)/f_s^2$ ), the motional parameters are estimated as:

$$C_m = \frac{8C_0k_t^2}{\pi^2} \quad (1.41a)$$

$$L_m = \frac{1}{\omega^2 C_m} \quad (1.41b)$$

$$R_m = \frac{\omega_{res}L_m}{Q_r}. \quad (1.41c)$$

and can be used to characterize the response of a device under test.

When designing a resonators, the contribution from multiple resonances should be taken into account. A good design should ensure that different acoustic modes are excited at different and well separated frequencies in order to distinguish the main resonant mode to the others. However, in practical applications it is a common thing to find spurious modes nearby the main resonance that, in some cases, strongly affect the acoustic performances of the device. The influence of multiple resonances can be taken into account adding one LCR branch to the BVD model for each of them as shown in fig.1.7a. Moreover, additional electrical components can be added to the electrical model to include dissipative contributions to the electrical response. The circuit in fig.1.7b includes the ohmic resistance of electrodes  $R_e$ , a resistance  $R_0$  modelling dielectric losses in the piezoelectric film, and a parasitic capacitance  $C_p$ . The addition of  $C_p$  is parallel to  $C_0$  increases the equivalent static capacitance but the two contributions are not distinguishable when estimating the parameters from an admittance curve. The energy that can be converted into mechanical energy is only the one stored by  $C_0$ , and therefore,  $C_p$  lowers the measured effective electromechanical coupling since does not actively participate in any electromechanical transduction.

The electrode resistance influences the admittance response only at  $f \approx f_s$  while  $R_0$  gives its contribution at  $f \approx f_p$ . The additional resistances modify eq.1.39 as

$$Q_r = \frac{2\pi f_s L_m}{R_m + R_e} \quad (1.42a)$$

$$Q_a = \frac{2\pi f_p L_m}{R_m + R_0}. \quad (1.42b)$$

where the additional components are derived as follows:

$$R_0 = \sqrt{\frac{8k_t^2}{\pi^2} + 1} \cdot \frac{\omega_r L_m}{Q_a} - R_m \quad (1.43a)$$

$$R_s = \Re\{Z(\omega \gg \omega_a)\} - R_0. \quad (1.43b)$$

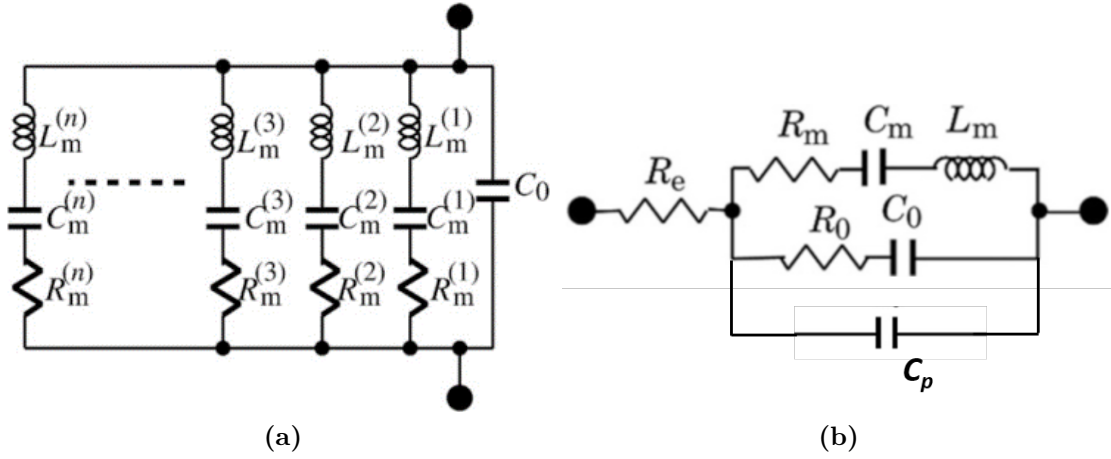


**Figure 1.7:** a) multi-resonances BVD model b) modified BVD model

It is worth noticing that these additional components may include other resonator non-idealities that affect the operation of the device together with the cited ones.

The BVD model is useful to characterize the performance of a device but cannot be used to predict the device response while designing a new architecture. To extract the parameters from a measured response, a set of steps should be followed:

- Y/Z extraction
- $(R_s+R_0)$  extraction for  $\omega \gg \omega_a$
- $kt^2$  extraction from  $f_s$  and  $f_p$
- $C_0$  extraction from  $\omega \gg \omega_a$
- $L_m$  computation from  $f_s$  and  $C_m$
- $R_m$  extraction from sweeping  $Q_r$  to match Y
- $R_0$  extraction from sweeping  $Q_a$  to match Y

The presented model has been discussed taking FBARs as a case study, but can be applied to any resonant structure, as Lamb waves resonators. To better understand the dependence of some parameters that have been introduced on the physics governing the device, a deeper physical insight is given in the next section.

## 1.4 Resonators FoM

The mechanical energy in the resonator body and the electrical energy applied through the metallic electrodes are cyclically converted from potential to kinetic. From a piezoelectric prospective, the stress and electric fields in the material reciprocally converts to each other owing to the two-way coupling shown by piezoelectricity. The performance of any piezoelectric device is dependent on the efficiency of both these two conversion mechanisms. There are two important parameters that quantifies this efficiency, they are defined as the *electromechanical coupling factor* ( $k_t^2$ ) and the *quality factor* (Q) of the resonator. In the following, a detailed description of these parameters and the analysis of the main effects that play a role in the optimization and degradation of the device figure of merit (FoM) is carried on.

### 1.4.1 Quality factor

The quality factor Q is directly related to the energy loss in the resonator. While the energy is cyclically converted, a portion of it turns into a form that cannot be recovered (e.g., heat) whereas another fraction could escape from the resonant structures and be dissolved in the surrounding environment. The simplest definition of Q is:

$$Q = 2\pi \frac{\text{Energy stored at resonance}}{\text{Energy dissipated per cycle}} \quad (1.44)$$

As there are multiple sources of dissipation and non-idealities in a real device, the denominator of eq.1.44 can be expressed as a sum of multiple components:

$$Q = 2\pi \frac{E_{\text{stored}}}{\sum_i E_{i \text{ dissipated/cycle}}} = \left( \sum_i \frac{1}{Q_i} \right)^{-1} \quad (1.45)$$

From this initial definition of the quality factor, a mechanical analogy with a damped mass-spring system is straightforwardly given. In analytical terms, a resonant structure is governed by a second-order differential equation of the form  $A\ddot{x} + B\dot{x} + Cx = 0$ , and the quality factor is related to the inverse of the damping ratio:

$$Q = \frac{1}{2\zeta}, \quad (1.46)$$

where  $\zeta$  is defined as the ratio between C and the critical damping of the system

$$\zeta = B/2\sqrt{CA}. \quad (1.47)$$

Even though these are good definition for the Q parameter, none of them is convenient to use when analyzing the admittance plots from a measurement. When it comes to relate the Q to plot, an handier definition is generally used:

$$Q = \frac{f_r}{BW_{3dB}}, \quad (1.48)$$

where  $f_r$  is the resonance frequency and  $BW_{3dB}$  is the frequency bandwidth comprising values between the admittance peak and its value at  $-3$  dB from the maximum. According to this last definition, it is clear that Q is higher when a sharper resonance is achieved, meaning that more energy is confined at the resonance.

Let's now briefly analyze which are the main terms appearing in the summation of eq.1.45. For the sake of conciseness, all the losses contributions can be identified in three main classes [4]:

1. *Electrical losses* from the non ideal conductivity of the electrodes and dielectric losses of the piezoelectric material
2. *Electro-mechanical losses* derived from the non ideal energy conversion from one domain to the other in the piezoelectric film
3. *Anchors and elastic losses* associated to the escape of acoustic energy from the system

The first class listed has been well characterized by research and these effects are now taken into account while processing the measurement results. The second contribution can be attributed to *intrinsic losses*, as they depend on the material properties and film homogeneity and ultimately depends on the reliability of the process flow. Finally, the energy leakage is strongly affected by the engineering of the structure and we call them *extrinsic losses*. They play a central role in one of the studies presented in this work and are here discussed with more emphasis.

One of the main source of losses is related to the amount of acoustic energy that is radiated trough the frame that holds the resonant structure of the device. This behaviour is strongly dependent on the geometry adopted and dimensions of the supports but, most importantly, its contribution depends also on the specific modes excited in the active areas of the device, hence making it difficult to universally characterize it. As the frequency is increased, the device dimension shrinks, but the anchor dimensions (commonly maintained at their minimum) may be unable to scale with the same rate. This make it fundamental to study an optimal anchor configuration for each different type of MEMS resonator.

## 1.4.2 Electromechanical coupling coefficient

The coupling factor describes the efficiency of the conversion from the electrical to the mechanical domain and vice versa. One of the most important aspect to keep in mind for its analysis is the difference between the electromechanical coupling factor characteristic of the resonator and the coupling factor of the material itself. The latter does not depend on the resonator design, whereas the first can be boosted or degraded depending on the electrodes implementation. The piezoelectric coupling factor ( $K^2$ ) of a lossless material can be defined as

$$K^2 = \frac{W_M}{W_M + W_E} \quad (1.49)$$

where  $W_M$  is the work that is delivered to a mechanical load by a piezoelectric actuator preloaded with a potential energy  $W_M + W_E$  [4]. It can be demonstrated that the coupling factor has a second order proportionality to the piezoelectric coefficient of the material and is inversely proportional to the stiffness and the dielectric constant. This is because a stiff material is subjected to less displacement (leading to smaller  $W_M$ ) and the higher the dielectric constant, the larger is the potential energy that is conserved in the electrical domain. The  $K^2$  represents the upper bound for the efficiency of energy conversion in a resonator built with a given piezoelectric material. To quantify the conversion efficiency in a resonant device with a specific geometry, the effective electromechanical factor is commonly defined as:

$$k_{eff}^2 = \frac{f_p^2 - f_s^2}{f_p^2} \quad (1.50)$$

where  $f_p$  and  $f_s$  are, respectively, the antiresonance frequency and the resonance one. In this work, the  $k_{eff}^2$  will be abbreviated as  $k_t^2$  and a slightly different definition will be used, in coherence with the work presented in [10]:

$$k_t^2 = \frac{\pi^2}{8} \frac{f_p^2 - f_s^2}{f_s^2} = \frac{\pi^2}{8} \frac{C_m}{C_0}. \quad (1.51)$$

Eq.1.51 describes the electromechanical coupling factor also in terms of the ratio between the motional capacitance and the static capacitance of the resonator. Both parameters can be estimated from the BVD model.

Finally, the FoM for a piezoelectric MEMS resonator is commonly defined as the product between the two parameters:

$$FoM = k_t^2 \cdot Q \quad (1.52)$$

It quantifies the efficiency in the mutual conversion of electrical and mechanical energy and the amount of energy that is not lost in undesired form of dissipation.



## Chapter 2

# 2DMRs and Lamb waves resonators

The electromechanical coupling at resonance of a MEMS resonator is strictly related to the magnitude of the piezoelectric coefficient that transduces the electric signal in an acoustic wave. FBARs are made by a piezoelectric film sandwiched between a top and a bottom electrode so that a thickness extensional mode is excited through the  $d_{33}$  coefficient. Since the monolithic integration of multiple FBARs is limited by the uniformity of the film thickness, other resonators have been introduced to solve this limitation and some of them with similar features are here briefly compared. A first example is given by contour mode resonators (CMRs) that rely on the direct excitation of the zero-order symmetric Lamb mode (S0). They enable a frequency tunability with lithographically defined electrode dimensions but show a limited electromechanical coupling due to the low  $d_{31}$  coefficient of Aluminum Nitride ( $kt^2 \approx 3\%$ ) [11]. A way to overcome this  $kt^2$  constraint is to combine the excitation of the two piezoelectric coefficients along different directions. This was firstly proposed by Zuo et al. in [12], where a coherent combination of  $d_{33}$  and  $d_{31}$  transduction was demonstrated to boost the electromechanical coupling up to 10% in a basic rectangular section of a cross-sectional dilation mode resonator (XD MR). Depending on the ratio between the thickness ( $t$ ) and the width ( $W$ ) of the resonant structure, a two dimensional mode builds up in the cross section as depicted in fig.2.1. Electrical charges are generated from mechanical displacement in the vertical direction through the  $d_{33}$  coefficient and in the lateral dimension through the  $d_{31}$  coefficient and the two contributions sum to each others increasing the electromechanical efficiency [12]. This is coherently described by the negative polarity of  $d_{31}$  with respect to  $d_{33}$ . On the other hand, while boosting the electrical performance, a very poor lithographic control of the resonance frequency affects the XD MR topology, just as in the case of FBARs.

Based on these inputs, the question that research has been answering is: how is it possible to effectively make a resonator that exploits the features of XDMRs enabling a lithographic tunability of the resonance frequency?

The solution is provided by the two-dimensional-mode resonators (2DMRs), presented for the first time in [13] and patented in 2018 by prof. Cassella from Northeastern University. They build from an array of thickness extensional mode unit cells spaced by a given distance. The maximum  $kt^2$  experimentally demonstrated up to the date of this work is 4.9%, which is a good result but not very surprising if compared to other devices.

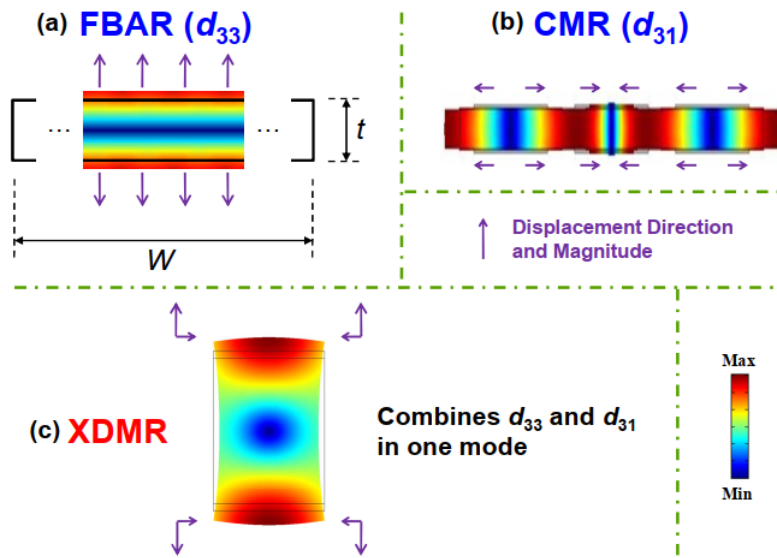


**Figure 2.1:** mode shapes of an (a) FBAR, (b) CMR and (c) XDMR (figure from [12]).

CLMRs, for example, rely on the combined excitation of the S0 and S1 Lamb waves through the alternation of electrodes polarities both along the vertical and horizontal directions. They showed high  $kt^2$  up to 6.3% (in AlN)) and enabled a good control on spurious modes; however, the electrodes width gets too small if high frequencies (e.g.  $> 2$  GHz) are targeted. This translates in a limitation in terms of power handling and electrical loading imposed to the system that can degrade the admittance response.

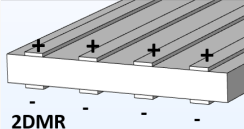
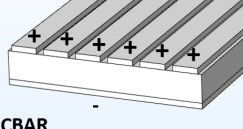
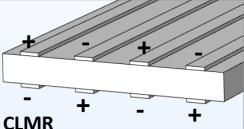
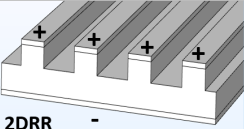
A recent work [14] demonstrates that a  $kt^2$  close to FBARs can be achieved by setting a very small spacing between homopolar fingers. This configuration is referred as coupled bulk acoustic resonator (CBAR) and, even if similar to 2DMRs with a bottom electrode plate, CBARs are characterized by a mode shape similar to the one of FBARs and therefore a poor frequency tunability is available for

design.

Lastly, a novel configuration exploiting unconventional acoustic behaviours has been introduced under the name of two-dimensional-resonant-rods (2DRRs). It is built from a forest of locally resonant rods, built in the body of an AlN layer that is sandwiched between a bottom un-patterned metal plate and a top metallic grating [15]. In this case, the main limitation is related to the process complexity that includes the partial etching of AlN in the regions between the rods.

All these configurations exploit the combination of different modes and piezoelectric coefficients and they all include thickness extensional displacements in their mode shapes. The table in fig.2.2 includes merits and limitations for the different resonators together with the electrodes polarity configurations; data refer to the last experimental results that have been published up to the date of this work.

The aim of the work presented in this thesis is to boost the 2DMRs performances overcoming their limits and the ones of the other resonant structures exploiting thickness extensional modes. From now on, the focus is put on this particular technology.

	 2DMR	 CBAR	 CLMR	 2DRR
Max $kt^2$	4.9 %	7.9 %	6.34 %	7.4 %
Merits	<ul style="list-style-type: none"> <li>✓ Good <math>kt^2</math></li> <li>✓ Larger electrodes than CLMR</li> </ul>	<ul style="list-style-type: none"> <li>✓ High <math>kt^2</math></li> <li>✓ Bottom electrode plate gives better AlN crystallinity</li> </ul>	<ul style="list-style-type: none"> <li>✓ High <math>kt^2</math></li> <li>✓ Good control of spurious modes</li> </ul>	<ul style="list-style-type: none"> <li>✓ High <math>kt^2</math></li> <li>✓ Bottom electrode plate gives better AlN crystallinity</li> </ul>
Limits	<ul style="list-style-type: none"> <li>✗ Needs patterning of bottom electrodes</li> <li>✗ Uncontrolled spurious modes</li> </ul>	<ul style="list-style-type: none"> <li>✗ Poor frequency variability</li> <li>✗ Similar to FBARs but more elaborated structure</li> </ul>	<ul style="list-style-type: none"> <li>✗ Needs patterning of bottom electrodes</li> <li>✗ Small electrodes at high <math>f</math></li> </ul>	<ul style="list-style-type: none"> <li>✗ Needs AlN partial etching</li> </ul>

**Figure 2.2:** comparison between Lamb wave resonators exciting thickness extensional modes. The  $kt^2$  refers to the maximum value experimentally demonstrated.

## 2.1 Device description

### 2.1.1 2DMR structure

2DMRs include both top and bottom electrode fingers, usually made with the same material. This gives a considerable design flexibility to excite resonant modes with precise periodicity along the width of the device. A schematic representation of a

2DMR is depicted in fig.2.3. The architecture is characterized by an Aluminum Nitride layer sandwiched between two identical metal gratings. The electrodes at the top and the bottom of the piezoelectric layer are used to excite the resonant modes inside the material through the application of a transverse electric field. They are formed by a periodic array of equipotential metallic fingers with width  $W_e$  and length  $L_e$ , spaced by a constant distance called, for convenience,  $s$ . As it will be deeply investigated, the dimension of the fingers and their relative spacing play a fundamental role in the definition of the lateral wavelength  $\lambda_x$  of the excited mode. The number of metallic strips that form the electrodes can be arbitrarily modified to define the input impedance of the device when the finger length has been set but this results in a trade-off when choosing long and narrow resonators instead of short and wide structures.

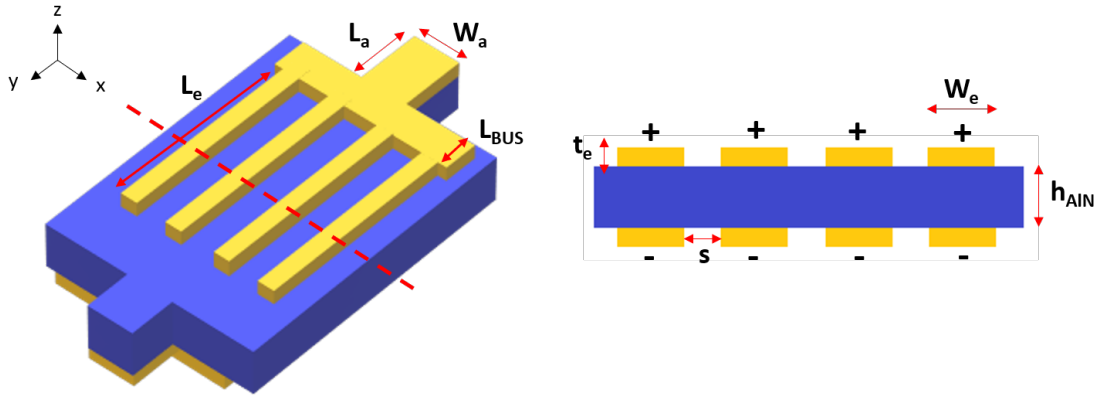


**Figure 2.3:** 3D and 2D profiles of a 2DMR resonator. The 2D model shows the section of the device cut by the red line.

Indeed, the number of the fingers and their length should be chosen so to ensure a poor electrical loading to the system. Given the BVD model in fig.1.7b, if  $R_e$  is much bigger than  $R_m$ , the admittance response *vs* frequency can be hidden, making the device not testable. Fig.2.4a shows the combinations of the number of finger pairs  $N_p$  and finger length  $L_f$  that satisfy matching conditions of the resonator input impedance to a set of  $R_{matching}$  for a given electrode width. In order to choose the right configuration that limits the electrical loading of the system, an estimation of the series resistance *vs* the electrode length is needed and its trend is shown in fig.2.4b. Different contributions to the  $R_s$  come from the pads and routings needed to test the structure and a deeper insight into these contributions is given in Appendix A at the end of the document. It is worth noticing that the series resistance shows an absolute minimum that gets smaller for bigger matching

impedances. For electrode finger lengths below the optimum values, the resistance contribution of the bus connecting the fingers gets much higher, due to the wider routing needed in accordance to extremely high  $Np$  values (fig.2.4a). As a trade off between  $R_s$  minimization and a good number of fingers  $N_p$ , a  $1 [k\Omega]$  matching impedance has been assumed for the studies here presented.

The connection of the equipotential gratings is done by a bus bar, made of the same material of the electrodes, with a width  $busW$  and a length equal to the device lateral dimension. In order to suppress any unwanted spurious mode with a resonance frequency close to the desired one, a dummy bus bar can be placed on the symmetric side of the electrically connected one to preserve the symmetry of the structure along the y direction, but a parasitic capacitance is introduced and hence it has not been considered. The entire structure is maintained suspended through the support of two anchors with width  $W_a$  and length  $L_a$ . These are the only supports of the device and should be designed so to minimize the amount of acoustic energy escaping from the resonator to the substrate. Their dimensions usually depend on the specific mode excited by the Lamb wave resonator, since different wavelengths and displacements propagate differently.

Since 2DMRs distinguish from the other configurations for a localized displacement concentrated under the electrodes, it is possible to anchor them along their length as in fig.2.5. As demonstrated by Cassella et al., this design feature helps with the suppression of spurious modes that can affect the device performance when the AlN sidewall profile deviates from  $90^\circ$ . Furthermore, as both lateral sides are anchored, heat produced by vibrations escapes more effectively, hence reducing the self-heating impact on the device non-linearity while enabling a higher power handling [16].

### 2.1.2 Materials considerations

The electromechanical coupling coefficient is not only correlated to the piezoelectric material but also depends on the metals adopted for the electrodes. As the  $k_t^2$  is proportional to the acoustic energy localized in the resonator, a large acoustic impedance difference between the metals and AlN can improve performances since waves are better confined. Actually, in addition for exciting acoustical waves, the electrode fingers work like Bragg reflectors so that a confinement of the acoustic wave is observed. The more difference between the high and low acoustic impedance is implemented in the periodic pattern, the better reflection of acoustic wave and the larger electromechanical coupling coefficient can be achieved [1]. Fig.2.6 shows the effective electromechanical coupling coefficient evaluated for different electrode materials and thicknesses; the results are related to CLMRs, but can be extended to the case of 2DMRs. Although Molybdenum shows a high acoustic impedance, the use of Mo as the IDT metal does not enable a  $k_{eff}^2$  as large as W or Pt because

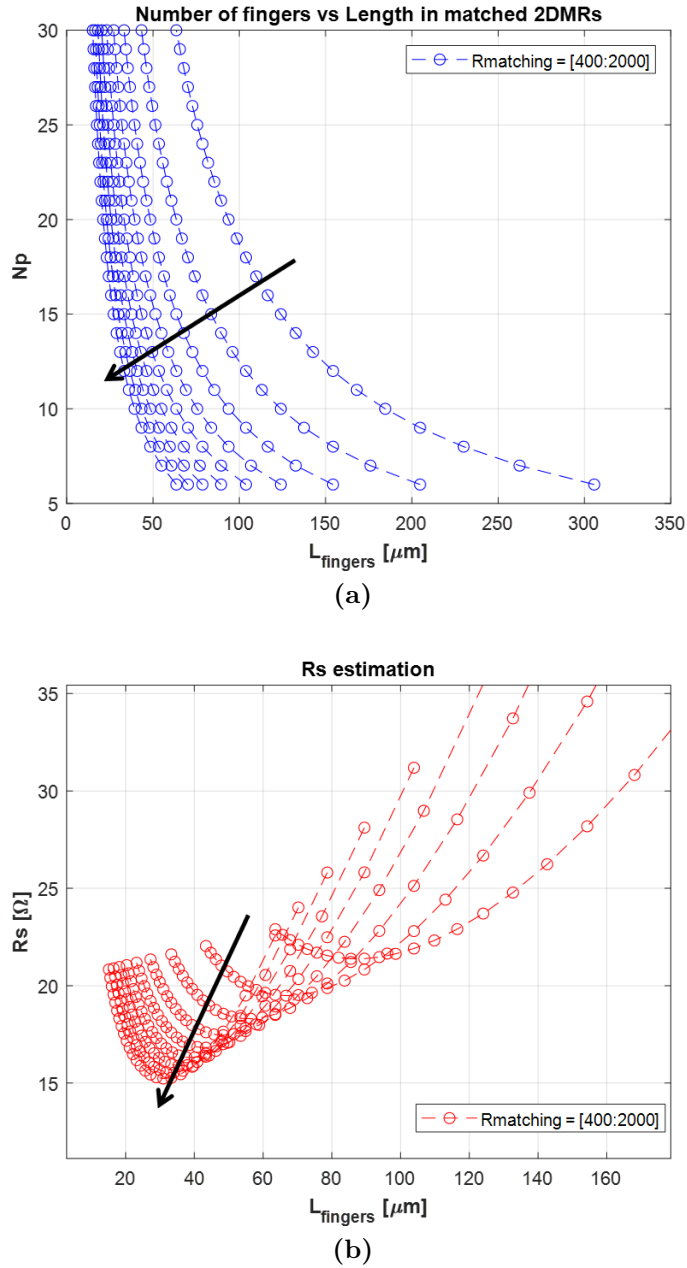


**Figure 2.4:** (a) number of 2DRM fingers vs length of the fingers that satisfy different impedance matching conditions (b)  $R_s$  dependence on the finger length for different impedance matching conditions. The plots refer to a Pt/AlN 2DMR with electrode width fixed to  $1.25 \mu\text{m}$  and the matching resistance values are expressed in  $[\Omega]$ .

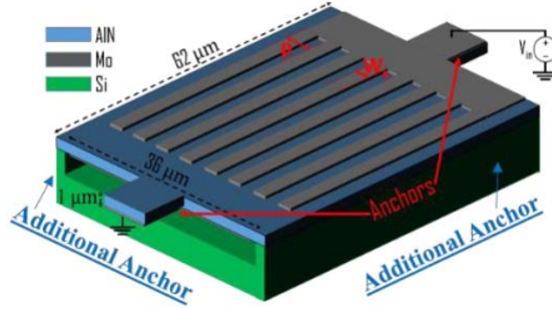


**Figure 2.5:** schematic of a 2DMR with additional anchors along its length (figure from [16])

of its smaller density [12]. Indeed, the light conductor allows more mechanical displacements inside the metal layer, which deteriorates the electromechanical performances. Therefore, a thick or heavy metal should be considered to obtain a large  $k_{eff}^2$  in one-port AlN Lamb wave resonator and its choice is strongly dependent on the reliability of the manufacturing process [1].

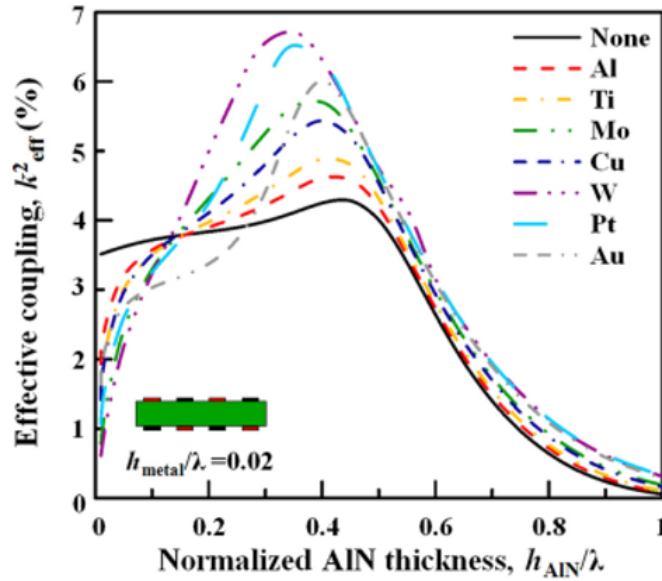


**Figure 2.6:** effective coupling computed for CLMRs with different materials and AlN thicknesses. The results can be generalized to the case of 2DMRs (plot from [1]).

When choosing the metal, other considerations about resistivity, acoustic losses,

roughness and ease of deposition should be analyzed. One fundamental feature to mitigate acoustic losses related to the piezoelectric material is the good crystallization of  $c$ -axis oriented AlN thin films. For example, W has a poor surface roughness making it difficult to deposit AlN with acceptable crystallinity. Most of the simulations for the studies presented here are based on Molybdenum and Platinum. That is because the in-house fabrication capabilities at Northeastern Un. are optimized for these two materials, being the classical materials of choice for this class of resonators. In the main experimental layout drawn for this work, however, Pt has been chosen because Mo can be attacked by  $XeF_2$  during the release process, introducing another limitation that still has to be characterized and understood.

Another important parameter for a proper excitation of the acoustic mode is the thickness of the electrodes. A general consideration is that when AlN is relatively thin (i.e.,  $h_{AlN}/\lambda < 0.2$  [1]), the  $k_{eff}^2$  decrease for thick metal layer because the displacement deviates from the piezoelectric film towards the metal. However, for higher AlN thicknesses (i.e.,  $h_{AlN}/\lambda > 0.4$ ), thick electrodes enhance the  $k_{eff}^2$  giving a stronger stiffening effect. In this work, electrode thicknesses in the range  $0.1 < t_{electrode}/h_{AlN} < 0.4$  have been simulated, they have been chosen to minimize the electrode resistance without affecting the mode shape at the resonance ( $t_{electrode}/h_{AlN} \approx 0.15$ ).

### 2.1.3 2DMR performances and mode analysis

The resonance frequency  $f_r$  of 2DMRs is determined by the thickness of the piezoelectric film ( $h_{AlN}$ ) and the pitch of the gratings ( $p$ ), defined as the sum of the electrode width  $W_e$  and the spacing  $s$ . As the electrode width can be arbitrarily made wider or narrower, the Lamb wave lateral wavelength  $\lambda_x$  can be engineered. Since the  $d_{33}$  coefficient is much larger than  $d_{31}$ , the mode of vibration has a larger stress along the  $z$ -direction than the  $x$ -direction (see fig.2.3 for axes reference) [13]. This implies that  $f_r$  is much more sensitive to the thickness of the piezoelectric substrate than to the pitch. However, a lithographic tunability of the resonant frequency higher than 10% can be achieved varying  $W_e$  and the relative spacing between fingers while maintaining high  $kt^2$  [13],[16],[17].

Fig.2.7 shows the simulated displacement along  $x$  and  $z$  directions in a 2D FEM model of a 2DM resonator. Electric fields in the  $z$  direction are applied and each couple of facing metallic strips excites a dispersive Lamb wave mode (i.e., with  $k_x \gg 0$ ). As the stress along  $x$  ( $T_x$ ) is in phase with the stress along  $z$  ( $T_z$ ), the charge produced by the two motions add to each others, hence enabling a high electromechanical coupling. Such mode has vertical displacement confined under the metallized region (that we call *active region*) and is *reactively* coupled to those excited by adjacent strips [18]. Although high  $k_t^2$  are generally achieved,

the coupling decreases significantly when different grating geometries are used to monolithically synthesize resonators working at different resonance frequencies. One solution to this limitation has been proposed in [18] where a piston-like displacement is reconstructed using framed electrodes. Although effective, this solution drastically complicates the manufacturing process.

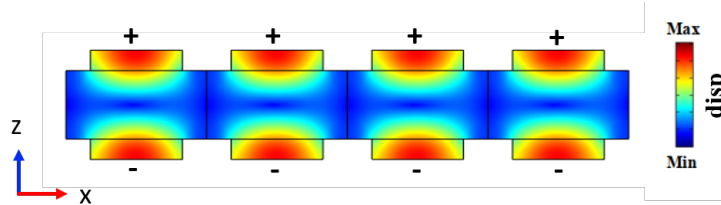


**Figure 2.7:** 2D displacement of a 2DMR exciting the S1 mode.

A better physical insight on the 2DMR mode excitation can be given analyzing the dispersion curves relative to the materials stack composing the active areas. Curves for low-order Lamb modes have been obtained through Comsol simulations for several piezoelectric film thicknesses, one example is shown in fig.2.8. Again, the self explanatory mode shape of fig.2.7 categorizes the 2DMRs in the class of thickness-extensional (TE) mode resonators and this displacement reflects the first symmetric Lamb wave mode shape (S1). This mode is characterized by two maximums and one minimum along the material thickness in the total displacement profile. The minimum frequency excitable by the S1 mode is called the *dilatational frequency*  $f_d$  and the mode has a cut-off frequency below which it cannot be excited with large wavelengths that is strongly dependent on the thickness of the Aluminum Nitride layer.

## 2.1.4 2DMR examples of applications

### Electrical filters

2DM resonators can be used in RF system as filters in many location of a transceiver chain. Electrical filters are implemented as an array of resonators that can be electrically, mechanically or acoustically coupled. The simplest filter configuration is the so called Ladder filter, formed by one-port resonators electrically connected as "shunt" and "series" components; an example is schematized in fig.2.9.

The number of resonators included in the chain depends on design constraints and gives the order of the filter. The center frequency of the filter is given by the series resonators while parallel resonators are engineered to express an anti-resonance at the same frequency. The measured scattering parameter of a 3rd order Ladder filter made with CLMRs is shown in fig.2.10 [19], showing the typical frequency

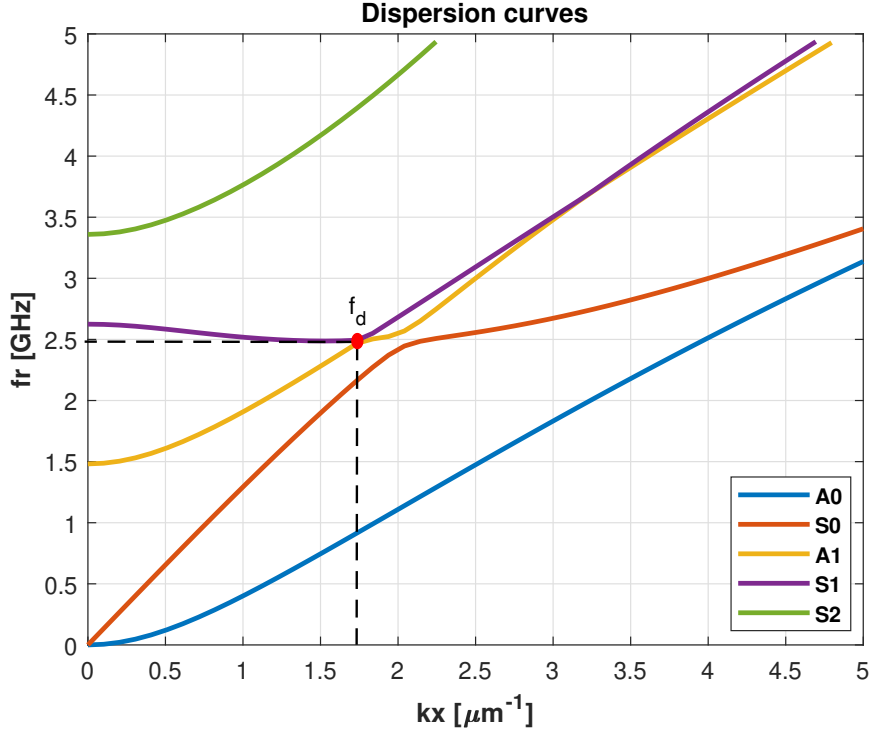


**Figure 2.8:** dispersion curves relative to the first 5 acoustic modes excited in the active area of the structure presented in fig.2.7. The curves have been computed through a Comsol<sup>®</sup> 2D model

window for selected signals transmission. At the series resonance frequency, the  $S_{21}$  parameter of the filtering stage is evaluated as:

$$\begin{aligned}
 S_{21}(f_s) &\approx \frac{2}{2 + N(Z_s/R_0 + R_0/Z_p)} = \\
 &\approx \frac{2}{2 + NrM^{-1}(\eta^{-1} + \eta)},
 \end{aligned} \tag{2.1}$$

where

$$\begin{aligned}
 \eta &= R_0\omega\sqrt{C_0^s C_0^p} \\
 r &= \sqrt{C_0^p/C_0^s} \\
 M &= Q_r \cdot k_t^2.
 \end{aligned}$$

$C_0^s$  and  $C_0^p$  are the capacitances relative to series and shunt resonators whereas  $R_0$

is the terminal resistance. If they are chosen so that  $\eta \approx 1$ , we get:

$$S_{21}(f_s) \approx \frac{2}{2 + N/2 \cdot \frac{r}{Q \cdot k_t^2}}, \quad (2.2)$$

being  $N$  the order of the filter. A few consideration can be done looking at eq.2.2. The highest the resonators FoM, the lowest the insertion loss I.L. (it is the loss of signal power due to the insertion of the device in the circuit) whereas a large capacitance ratio  $r$  gives higher losses. These ones are directly related to the order of the filter (the highest  $N$ , the higher the I.L.), however, a trade off is given by the *out-of-band-rejection* which is enhanced by higher  $N$  values. The frequency bandwidth is proportional to the electromechanical coupling coefficient of the resonators:

$$BW_{3dB} \approx \frac{k_t^2}{\sqrt{1 + r^2}} \quad (2.3)$$

Therefore, 2DMRs are good candidates for implementing wide bandwidth Ladder filters. This is an application that has never been implemented with 2DMRs and the device optimization reached with this work will give a support for future filter designs.

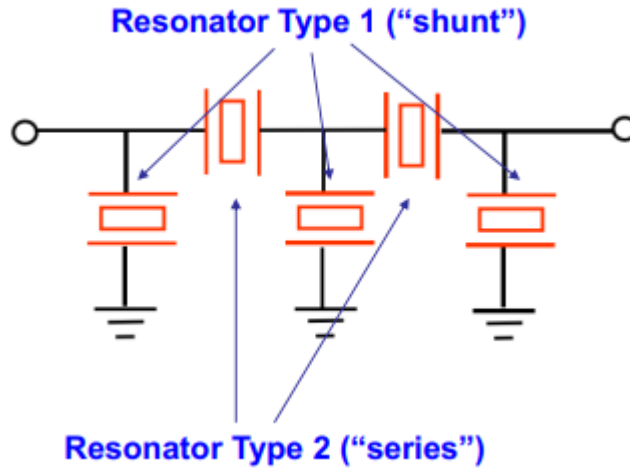


**Figure 2.9:** schematic representation of a Ladder filter.

## Oscillators

MEMS resonators can be interfaced with amplifiers to build electronic oscillators that generate an electric signal at the resonance frequency. 2DMRs are good candidates for this application because of their high quality factor and frequency filtering property. The general topology of an oscillator is given in fig.2.11; here

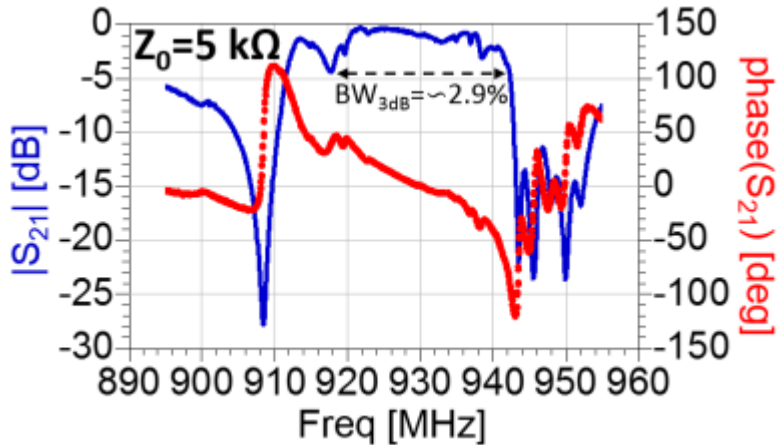


**Figure 2.10:** *experimental results of a Ladder filter based on CLMRs.  $BW_{3dB} \approx 2.9\%$  and  $I.L. \approx 0.4$  dB were demonstrated [19].*

the MEMS resonator is placed in a positive feedback loop of a sustaining amplifier with a frequency dependent gain  $A(s)$ , filtering the frequency response according to a transfer function  $\beta(s)$ . When the power is switched up, the noise present in the loop gets amplified while being filtered and, after multiple passes, the signal growth stabilizes because of non linearities [20]. In order for the oscillation to start and stabilize, the linear gain of the loop (i.e.,  $|A(s)\beta(s)|$ ) should be greater than unity and the phase shift around the loop should allow a constructive growth of the signal ( $\angle(A(s)\beta(s)) = n360^\circ$ ,  $n = 0,1,2, \dots$ ). These conditions are known as Barkhausen conditions.

The non idealities of both MEMS resonator and sustaining amplifier compromise the purity of the spectral density of the output signal. The introduction of *phase-noise* (PN) relative to the MEMS resonator mainly depends on two factors [20]:

- an higher Q of the resonator reduces the PN because of enhanced filtering capabilities
- the PN is decreased when higher powers can be sustained because of the increased sustainable signal amplitudes.

Both the conditions above can be fully satisfied by a proper design of a two-dimensional mode resonator.

## Radio Front-Ends

The design of a reconfigurable RF front-end includes arrays of filters and oscillators that would be impractical if fabricated with FBARs or LC tunable filters because

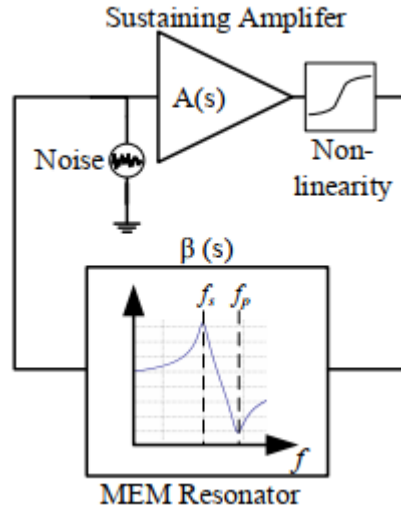


**Figure 2.11:** *schematic of an MEMS resonator-based oscillator (fig. from [20]). The MEMS acts as a filtering stage in the feedback loop of the sustaining amplifier at the resonance frequency.*

these components cannot be monolithically integrated on the same chip. This imposes the need for external interconnects that introduce parasitic capacitances, increasing the insertion losses. To solve this bottleneck, a massive array of 2DMRs and switches could be implemented on the same silicon chip further reducing the form factor of current technologies [21]. Moreover, the monolithic fabrication of multiple components could drastically reduce the parasitic components. The AlN based technology could substitute the existing single-band multi-chip solution with a multichannel **single-chip** implementation enabled by switched narrow band AlN filters and oscillators [21]. The hypothetical front-end evolution from a single-band to a multi band architecture is schematically shown in fig.2.12, where CMRs have been implemented instead of 2DMRs.

### Power sensing and parametric circuits

Due to the localized displacement shown by 2DMRs that enables the introduction of additional anchors at lateral sides, these devices can sustain more power than CLMRs and CMRs. Indeed, side anchors represent another way for self generated heat to disperse in the environment without overheating the device itself. This feature can be exploited, for example, in the design of a novel power detector architecture where two acoustically isolated 2DMRs interact at resonance so that information about the input power is read from an unloaded output terminal (see Chapter 4 for details). Moreover, 2DMRs show wider electrodes compared to other

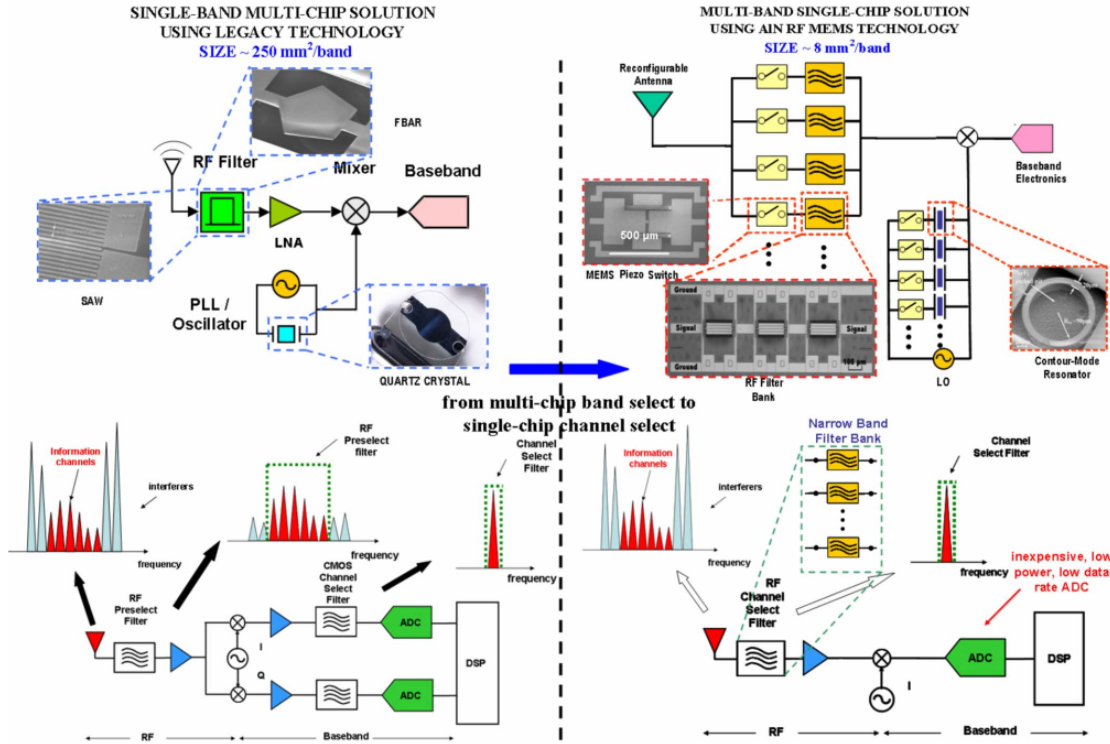


**Figure 2.12:** envisioned change in RF front-end architecture from a single band to a multi-band system enabled by the monolithic integration of AlN based MEMS resonators (fig.from [21]). 2DMRs could replace CMRs thanks to the optimized performances presented in this thesis.

resonators and therefore are suited for very and ultra-high frequency applications ensuring low electrical loading. Further applications are currently investigated by MicronRF group, they include the monolithically integration of varactors and other nonlinear components with high performance 2DMRs with the target of building innovative parametric systems without the need of off-chip interconnects. An example is given by frequency selective limiter circuits (FSL) for above-threshold signal suppression. In this application, a 2DMR resonator adds an extra layer of selectivity for the FSL to stop signals at the resonance frequency with power exceeding a given threshold.

## 2.2 2DMR Finite Element Modeling

In this section, the fundamental components of some of the FEM models built for simulating the operation of 2DMRs are illustrated.

For the sake of simplicity and minimization of computational efforts, each device has been firstly simulated with a basic 2-Dimensional model. Fig.2.13 shows a 2D schematic composed of one thin layer of Aluminum Nitride and metallic electrodes (made of Pt or Mo) on its top and bottom faces. The main purpose of 2D models is to understand the acoustic response of the piezoelectric plate when electrically excited by an infinite electrode array. This can be easily implemented by setting periodic boundary conditions (PB) at the lateral edges of the plate, as shown in the model schematic.

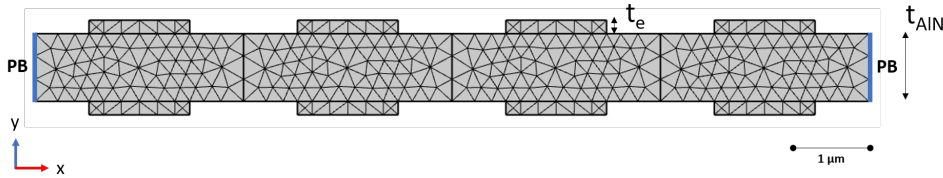


**Figure 2.13:** 2D COMSOL<sup>®</sup> model of the periodic structure modelling the transverse section of a 2DM resonator.

By sweeping the frequency of the voltage signals applied to top and bottom electrodes, acoustic modes excited in a wide frequency range can be monitored from the admittance plots extracted directly from the finite-elements model. Different modes of resonance can be categorized from their mode shapes and displacement profiles expressed at the resonance frequencies. These acoustic modes can be approximately mapped on dispersion curves computed for infinite ideal structures, where due to the finite volume, only a set of  $k_x$  in the continuous wavevectors space satisfies the Cauchy problem governing the displacement. However, since the Lamb waves theory is derived under the assumptions of infinite plate width and perfect layer homogeneity, it is fundamental to notice that this approach is affected by significant approximations because regions with very different acoustic behaviour alternates within the same resonant structure. Moreover, Lamb waves only represent sets of solutions in the eigenspace relative to each region and a particular mode could be described as a linear combination of Lamb's eigenfunctions, making it difficult to categorize it from its displacement shape. In fact, the modeling of Lamb modes in finite structures is truly a complex phenomenon which is simply inaccessible to hand modeling [22] and it is convenient to use dispersion curves as an instrument for designing new structures.

The mesh size of the 2D structure is chosen to have at least six elements for each electrode, being this an empirically-demonstrated good value to ensure reliability of the simulations.

A more complex model is required for 3D simulation where several features of the device and surrounding substrate have to be considered. Fig.2.14 shows the 3D model of a 2DMR. There are three main building blocks in the structure: the resonator, the released region and the Perfectly Matched Layers (PMLs). All the

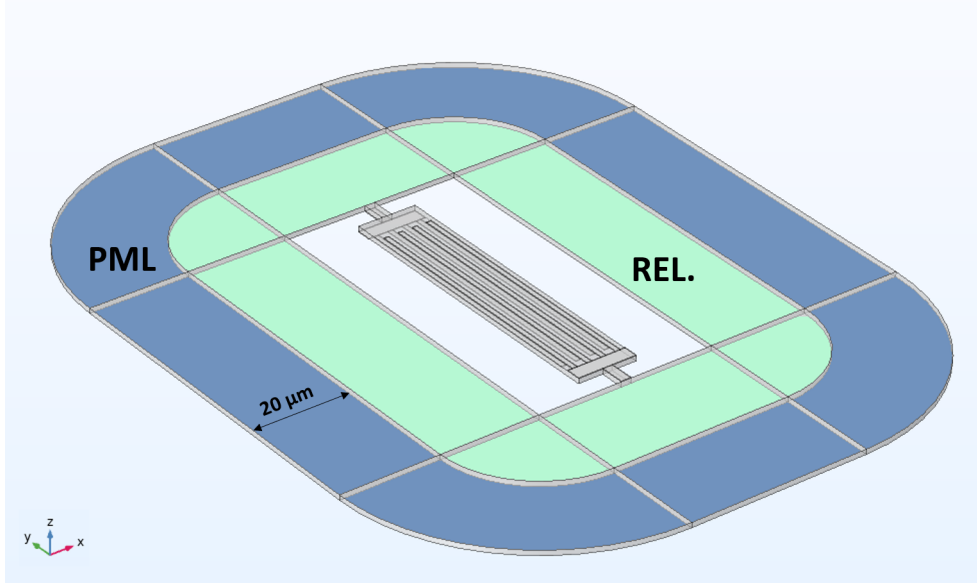


**Figure 2.14:** 3D COMSOL® model of a 2DMR including the resonator, the released area and the PMLs.

the parameters characterizing the resonator geometry have been swept in different ranges, following the same ideas of 2D simulations. The complete model permits to analyze the performances looking for the best electrodes, buses and anchors dimensions in all directions. At this point, the optimization procedure may seem quick and easy, however, it is important to remember that 2D analysis only considers the  $x$  and  $z$  components of the acoustic mode, but the addition of the third dimension drastically changes the device response introducing several uncontrolled spurious modes.

The released region models the area of AlN substrate that has been isotropically etched to detach the resonant structure from the substrate. Two different boundary conditions have been applied at the edges of this area, one modelling fixed constraints (FC) and the other modelling PMLs. Perfectly matched layers play a fundamental role in the evaluation of acoustic energy transmitted from the resonator active areas to the substrate through the anchors. In most of the

chips, the resonating device is much smaller than the silicon substrate on which it is built, and waves radiating from the anchors are attenuated by the time they reflect from the chip sides. For this reason, reflected waves can be most of the times neglected as a first extreme approximation. Under this assumption, the volume around processed areas can be modelled without loss as a semi-infinite half-space. Usual conditions employed to model the response of such an infinite domain make use of on boundary dampers, infinite elements, boundary integrals or exact Dirichlet-to-Neumann boundaries [23]. Each of these methods truncates the domain with an artificial boundary that absorbs the incident acoustic waves. However, there is no closed form of a Green's function for an elastic half-space and so, Dirichlet-to-Neumann boundary conditions cannot express its highly accurate global conditions[23]. The issue can be solved by the adoption of a *perfectly matched layer* designed to absorb acoustic waves that does not need a closed form for the Green's function to operate. With the PML implementation, COMSOL<sup>®</sup> introduces a complex-valued coordinate transformation in the acoustic field equations to compute the energy lost in the substrate [24]. To implement this transformation, the software automatically extracts the geometrical parameters but requires an estimation of the acoustic wavelength propagating in the layers ( $\lambda_{PML}$ ). A part from the wavelength, other parameters as *PML scale factor* and *order* have been set to 1, following the example presented by Segovia-Fernandez in [24].

The optimized mesh of the 3D structure is shown in fig.2.15, where a very *fine* element density is set inside the resonator. The mesh of the portions of anchors facing the external substrate has been mapped and parametrically defined to maintain a constant density of square elements while sweeping anchors dimensions in simulations. Finally, in order to ensure the absorption of the acoustic waves propagating from the released area into the PMLs, the mesh of these domains has been drawn following the mesh elements of the released area and using cylindrical coordinates at the corners.

As a means to reduce the computational complexity and time maintaining an high mesh element density inside the structure, a *symmetry plane* has been introduced in the 3D model for the studies where an high number of simulations was needed. Fig.2.16 shows an example of half resonator used to simulate big parametric sweeps in 3D simulations; though it barely approximates the real symmetries of the structure, it has been empirically demonstrated that the results are only slightly different from the case in which the entire structure is simulated. As will be discussed, a complete 3D model that includes the Si substrate surrounding the released area has been built as a final configuration to limit the FC and PMLs approximations, details will be discussed in the next chapter.

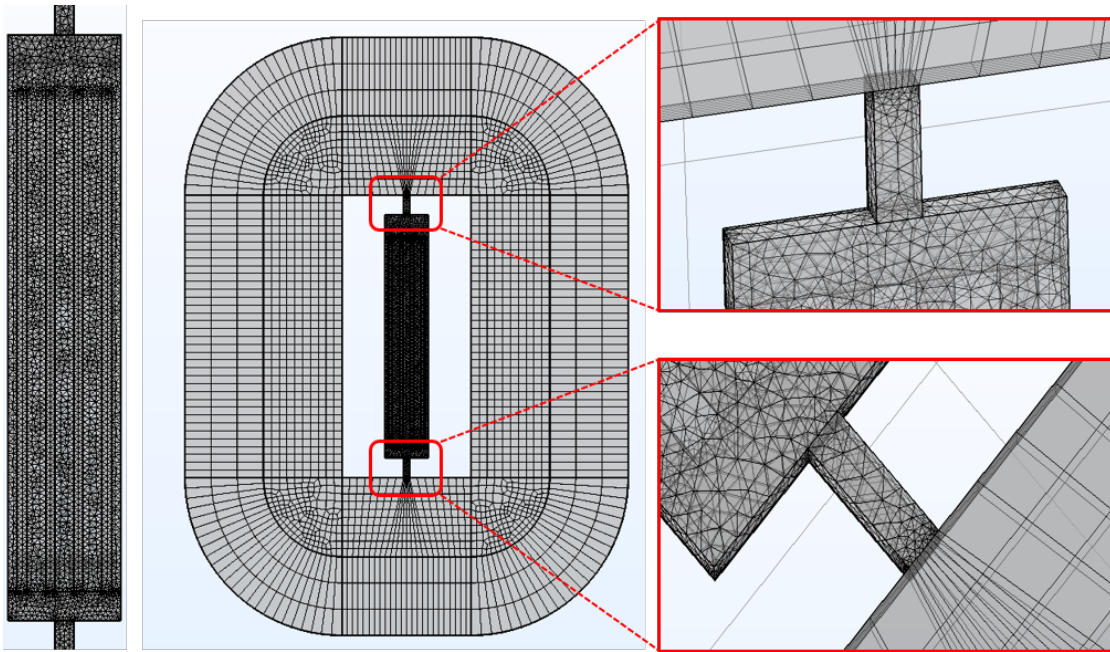


**Figure 2.15:** mesh of the 3D FEM model of a 2DMR including resonator, released area and PMLs.

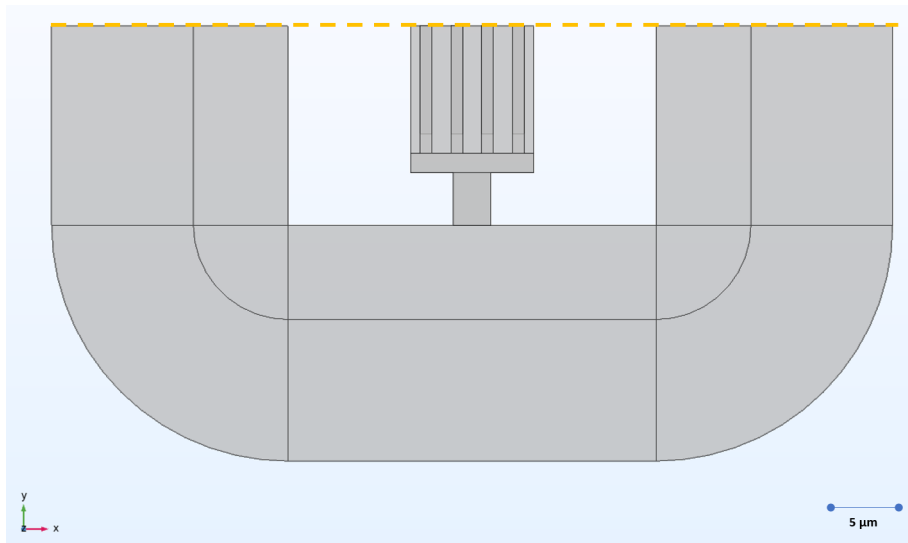


**Figure 2.16:** 3D COMSOL model of a 2DMR including the resonator, the released area and the PMLs with a symmetry plane to reduce the computational efforts and time.

## Chapter 3

# 2DMR design optimization

In this chapter, four studies for the optimization of the 2DMR design are presented. First of all, anchor losses have been analyzed through 3D simulations to improve the quality factor of 2DM resonators at the resonance frequency. Then, novel architectures have been investigated and optimized to boost the electromechanical coupling coefficient while minimizing unwanted spurious modes in the electrical response of the devices.

### 3.1 Anchor losses optimization

The resonator quality factor  $Q$  is a key parameter for the reduction of power consumption and noise cancellation in a MEMS resonator as it is directly correlated to the frequency selectivity of the electrical response. Many effects contribute to its deterioration and, in the case of 2DMRs, the scattering of elastic waves from the resonator into the substrate through the anchors is one of the main source of losses [24]. These are called *anchor losses* and can significantly reduced by properly designing the anchoring supports and concentrating the acoustic wave displacement far from the tethers area [25]. Different approaches have been followed to reduce their effect in MEMS resonators starting from the optimization of the anchors geometry to the introduction of reflectors to better confine the acoustic energy [26] while engineering acoustic mismatches in the released areas [27]. However, even though they are all similar, each resonator typology is based on the excitation of different acoustic modes, and therefore, the optimization results cannot be generalized for all MEMS resonators. Since no studies have ever been conducted on 2DMRs, this section focuses on analyzing the quality factor dependence on the dimensions of the inactive region comprising the inactive gap, the bus and the anchor.

### 3.1.1 Bus dimensions design

The *bus* is the top metallized strip included between the stress-free edge beside the anchor and the active area. Its main function is to route the electrical signal from the pads to the electrode fingers and its dimensions should be carefully chosen to minimize the electrical loading of the resonator. It plays also an important role in defining the boundary conditions of the active areas at the fingers edges.

As elucidated in [26] for the case of Contour Mode Resonators, there are mainly two mechanisms by which the bus width can impact the quality factor. Firstly, the bus can affect the amount of acoustical energy generated by the active region in the anchoring direction, and secondly, it impacts the amount of energy that is transferred from the active region to the inactive one. The same work shows that, given an acoustic wavelength  $\lambda$  excited in the active area, when the bus width is chosen to have a spacing between the active area and the resonator edge  $d \approx \lambda/4$  (fig.3.1), each bus behaves as a  $\lambda/4$  transformer, converting the stress-free boundaries beside the anchors into *virtual fixed boundaries* [26]. When this happens, the amount of acoustic energy that the resonator generates along the anchor direction is minimized, therefore reducing acoustic leakage through anchors. For what regards the second mechanism, it was found that for a given anchor geometry, there exist two sizes of the bus that minimize the acoustic energy transmitted through the inactive area. Following the same approach used for CMR, the dependence of the energy stored in the active areas (and hence the quality factor) on the bus dimension has been analyzed for 2DMRs for the first time in this work. Moreover, design rules for the anchors length have been derived starting from the optimized bus width.

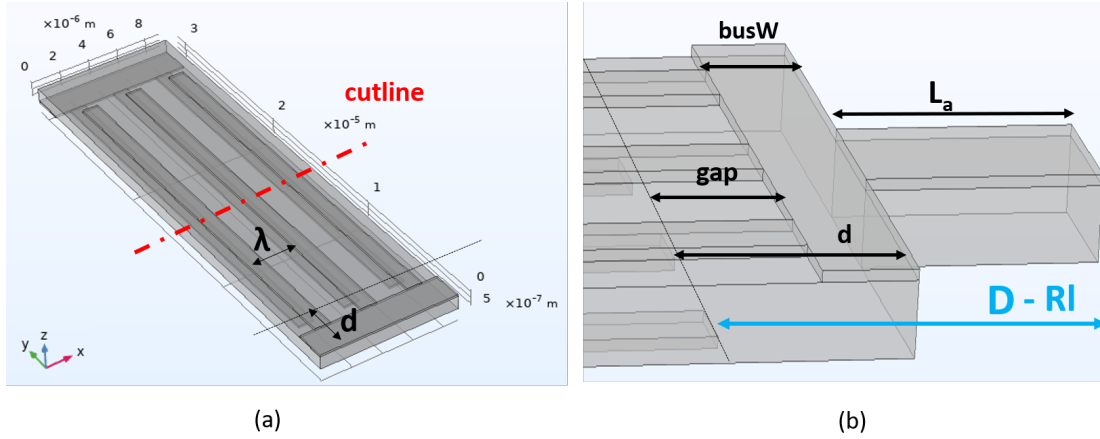


**Figure 3.1:** (a) 3D model used for the study on the bus and (b) inactive area dimensions that have been optimized.

### Buses as $\lambda/4$ transformers

The minimization of acoustic energy generated along the anchors direction can be intuitively reduced to the problem of how to introduce nodal lines at the edge of the active regions so to minimize the displacement in close proximity to the anchors. The motion due to each couple of fingers at the edge of the resonator active region can be modeled by an equivalent spring constant  $K$ . It can be seen as formed by the parallel combination of all the equivalent spring constants of the fingers forming the electrode grating, each defined as [26]:

$$K^n = F_y/|u^n| \quad (3.1)$$

where  $F_y$  is the force generated along the anchors direction and  $u^n$  is the displacement induced by it. Since the *gap* dimension (fig.2.3,b) is usually small compared to the bus, it is possible to approximate the same acoustic wavelength for both the active and inactive region; however, this approximation loses credibility for metal thicknesses higher than 200 [nm]. Under this assumption, it is possible to write the displacement  $u^n$  as the sum on an incident and a reflected acoustic wave generated by the active area of the fingers:

$$u^n = u_{in}^n + u_{ref}^n = u_{in}^n (1 - \Re\{\Gamma \cdot e^{j2kd}\}) \cdot \hat{y} = (u_{in} - u_{in} \cdot \Gamma \cdot \cos(2kd)) \cdot \hat{y} \quad (3.2)$$

where  $\Gamma$  is the reflection coefficient relative to the stress-free boundary ( $\Gamma \approx -1$ ). In a 2DMR, the number of fingers included in the anchor width is generally greater than one, let's indicate this number with letter  $M$  and the total number of fingers with  $N$ . The effective spring constant can thus be evaluated as

$$\begin{aligned} K_{eff} &= (N - M)K^n + MK_{anch}^m = \\ &= (N - M) \frac{F_y}{(u_{in} + u_{in} \cdot \cos(2kd))} + M \frac{F_y}{u_{in}} = \\ &= K_{anch} \left[ \frac{N + M \cos(2kd)}{1 + \cos(2kd)} \right] \end{aligned} \quad (3.3)$$

where  $K_{anch}^m$  is the equivalent spring constant of the  $m$  finger facing the anchor and does not include any reflection. The energy that is generated toward the inactive area can then be computed:

$$E_y = \frac{1}{2} \frac{F_y^2}{K_{eff}} = \frac{F_y^2}{2K_{anch}} \cdot \left[ \frac{1 + \cos(2kd)}{N + M \cos(2kd)} \right] \quad (3.4)$$

Eq.3.4 qualitatively describes the amount of energy that can be potentially transmitted through the inactive area. However, only a portion of it is proportional to

the anchor width (and hence to  $M$ ) can cross the anchor. The amount of energy flowing through the tether supports can therefore be written as:

$$E_{anchor} = \frac{M \cdot Pitch}{W_{tot}} \cdot E_y \quad (3.5)$$

Eq.3.5 shows that the energy reaching the anchors can be thought as a product of two transfer functions, the first dependent on the ratio between the anchor width and the total width of the resonator and the second expressed as a function of  $d$  (fig.3.1b). By separating the two contributions and normalizing eq.3.4 with respect to constant terms we can write the transfer function governing the acoustic energy:

$$H(d) = \frac{1 + \cos(2kd)}{N + M\cos(2kd)} \quad (3.6)$$

The quality factor  $Q$  is inversely proportional to the amount of energy lost per cycle and hence the same relation holds relatively to the transfer function in eq.3.6. Fig.3.2 shows simulated results of the normalized expression of  $H(d)$  with respect to the lateral acoustic wavelength together with the energy density stored in the active areas for the ideal case of a 2DMR with  $N = 3$  and  $M = 1$ . It shows that for  $d$  values equal to odd multiples of  $\lambda_x/4$ , the energy transfer function reaches its minimum and for this value the mechanical energy density in the active area is maximized. The density of mechanical energy has been evaluated through 3D COMSOL<sup>®</sup> simulations along the cut-line shown in fig.3.1a and similar results have been obtained for 2DMRs exciting different wavelengths confirming the relation derived above.

As the bus is the biggest electrical component within the 2DMR area, its dimension should be chosen to minimize the resistance while satisfying the derived conditions. A good trade-off is generally given for  $busW \approx 5/4\lambda$  and this is the value adopted for most of the devices studied in this work. .

### $k_t^2$ considerations

As described by eq.1.51, the electromechanical coupling coefficient is directly proportional to the resonator motional capacitance  $C_m$ , which inversely measures the effective stiffness of the resonator. As a general rule, when the resonator is made stiffer, the  $k_t^2$  is reduced because less displacement is enabled and lower  $C_m$  is observed. This relates the coupling coefficient to the boundary conditions imposed to the active area edges and, ultimately, to the bus dimensions. Indeed, when the inactive region is engineered so to behave as a  $\lambda/4$  transformer, nodal lines are introduced at the finger edges, making the device stiffer [13]. This effect leads to a reduction in the  $k_t^2$  of the resonator, which shows an inverse behaviour with respect to the quality factor  $Q$ .

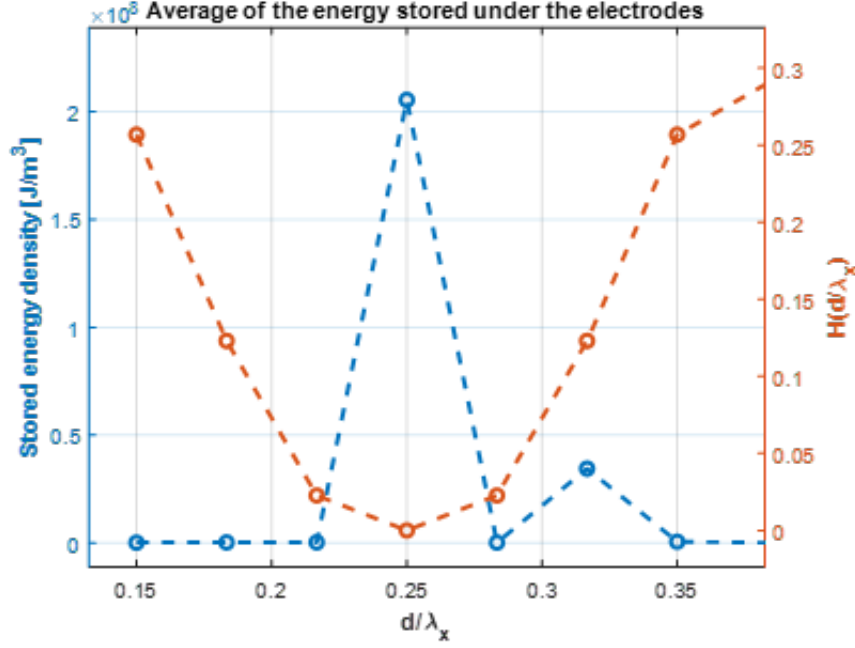


**Figure 3.2:** *normalized transfer function governing the acoustic energy generated towards the anchors direction and mechanical energy density stored in the 2DMR active areas versus normalized  $d$  dimensions.*

### 3.1.2 Anchor dimensions design

#### Energy flow minimization with FC

In the previous section, the  $\lambda/4$  transformer behaviour was derived under the assumption of no energy reflection from the released area towards the anchors. However, the substrate surrounding the device acts as a fixed boundary constraint (FC) placed at the edge of the released area due to the significant acoustic impedance difference between the two regions. This introduces an acoustic reflection that establish a dependence of  $E_{anch}$  on the length of the anchors  $L_a$ .

The resonator can be modelled with the equivalent circuit shown in fig.3.3 [28] in which the anchor acts as a transmission line and a voltage generator is introduced to model acoustic forces along the  $y$  direction (i.e.,  $F_y$ ). The line is ended on an open circuit to model the fixed boundary condition imposed by the substrate. In the circuit,  $Z_0$  is the characteristic acoustic impedance of the active area whereas  $Z_1$  is the characteristic impedance relative to the inactive portion  $D = L_a + d + Rl$  (fig.3.1) where the released area can be neglected as a first case study. The voltage seen at node  $a$  in figure is a function of the anchor length due to the dependence of  $Z_{in}$  on the length of the line.

The transmission line input impedance is defined as:

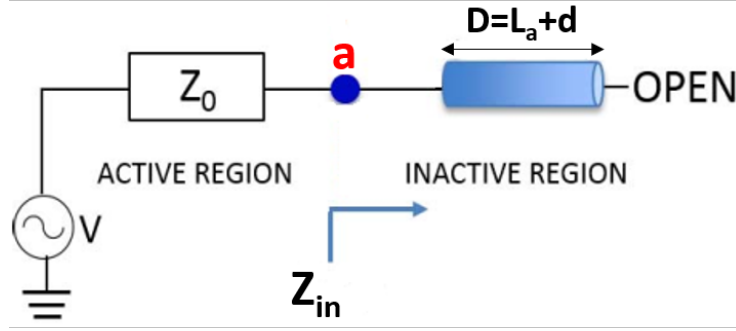


**Figure 3.3:** equivalent electrical circuit of the active and inactive region in a 2DMR. The anchor is modelled as a transmission line.

$$\begin{aligned}
 Z_{in} &= \frac{V_a}{I_a} = Z_1 \left( \frac{e^{jkD} + \Gamma_L e^{-jkD}}{e^{jkD} - \Gamma_L e^{-jkD}} \right) = \\
 &= Z_1 \left( \frac{e^{jkD} + e^{-jkD}}{e^{jkD} - e^{-jkD}} \right) = \\
 &= \frac{-jZ_1}{\tan(kD)},
 \end{aligned} \tag{3.7}$$

where  $k = 2\pi/\lambda$  is the acoustic wavevector and  $\Gamma_L$  is the reflection coefficient given by the load mismatch, defined as:

$$\Gamma_L = \frac{Z_L - Z_0}{Z_L + Z_0}$$

but if FC are assumed,  $Z_L \gg Z_0$  and so  $\Gamma_L \approx 1$ .

The stored acoustic energy at the input of the transmission line can be computed as the product of the current and voltage at node **a**:

$$\begin{aligned}
 E_{av} &= \frac{1}{2} \Im \{ V_a I_a^* \} = \\
 &= \frac{1}{2} \Im \frac{V^2 Z_{in}}{|Z_{in} + Z_0|^2} = \\
 &= \frac{1}{2} \frac{V^2 Z_1 \tan(kD)}{Z_0^2 \tan^2(kD) + Z_1^2}
 \end{aligned} \tag{3.8}$$

If little acoustic mismatch is assumed from the active to the inactive area,  $Z_1 \approx Z_0$  and eq.3.8 reduces to

$$E_{av} = \frac{V^2}{4Z_0} |\sin(2kD)| \tag{3.9}$$

and a new energy transfer function is introduced:

$$F(L_a) = |\sin(2kD)| = |\sin(2kd + 2kL_a + 2kR_l)|. \quad (3.10)$$

According to  $F(L_a)$ , the energy available at node  $\mathbf{a}$  nulls when  $D = n \cdot \frac{\lambda}{4}$ ,  $n$  being an integer value. Therefore, if  $d$  is chosen to be a multiple of  $\lambda/4$  to null eq.3.6, the anchor length should be chosen to be a multiple of the same factor too. By sweeping the bus length, the contribution due to the  $\lambda/4$  transformer and the one derived from the transmission line multiply together, giving a general transfer function with  $\lambda/4$  periodicity:

$$K(d) = H(d) \cdot F(d) = \frac{1 + \cos(2kd)}{N + M\cos(2kd)} \cdot |\sin(2kd + 2kL_a + 2kR_l)| \quad (3.11)$$

Since COMSOL<sup>®</sup> Multiphysics does not precisely evaluate the *Quality factor for resonance frequencies* under the assumption of fixed boundary conditions, a new approach based on the parallelism between the acoustic fields equations and Maxwell equations has been followed for the Q computation.

The acoustic equation of motion can be written as:

$$\nabla \cdot \mathbf{T} = \frac{\partial p}{\partial t} - \mathbf{F}, \quad (3.12)$$

where  $\mathbf{p} = \rho \mathbf{v}$  is the momentum density ( $kg/m^2s$ ) and  $\mathbf{v}$  the velocity of the acoustic wave. The strain-displacement relation becomes

$$\nabla_s \mathbf{v} = \frac{\partial \mathbf{S}}{\partial t}. \quad (3.13)$$

Eqs.3.12 and 3.13 can be manipulated as:

$$-\mathbf{v} \cdot (\nabla \cdot \mathbf{T}) = -\mathbf{v} \cdot \frac{\partial p}{\partial t} + \mathbf{v} \cdot \mathbf{F} \quad (3.14a)$$

$$-\mathbf{T} : \nabla_s \mathbf{v} = -\mathbf{T} : \frac{\partial \mathbf{S}}{\partial t} \quad (3.14b)$$

where the double dot product of two tensors introduced is defined as  $\mathbf{A} : \mathbf{B} = A_{ij}B_{ij}$  with summation over the repeated subscripts. Adding the two equations in eq.3.14, integrating their expression over a volume V and applying the divergence theorem for a bounding surface S we get [29]:

$$\oint_S (-\mathbf{v} \cdot \mathbf{T}) \cdot \hat{\mathbf{n}} dS = - \int_V \mathbf{v} \cdot \frac{\partial \mathbf{p}}{\partial t} dV - \int_V \mathbf{T} : \frac{\partial \mathbf{S}}{\partial t} dV + \int_V \mathbf{v} \cdot \mathbf{F} dV. \quad (3.15)$$

Following a derivation similar the one of electromagnetism, the right-hand side terms in eq.3.15 can be identified as the rate-of-change of the stored energy in the

system  $\partial U/\partial t$ , the total viscous power loss of the system  $P_d$  and the total power supplied to the volume  $P_s$  [29]. With this identifications, eq.3.15 reduces to:

$$\oint_S (-\mathbf{v} \cdot \mathbf{T}) \cdot \hat{\mathbf{n}} dS + \frac{\partial U}{\partial t} + P_d = P_s \quad (3.16)$$

where  $U$  is the total elastic energy in  $V$  and the surface integral expresses the total power flow outward through the closed surface  $S$ . The integrand

$$\mathbf{P} \cdot \hat{\mathbf{n}} = -\mathbf{v} \cdot \mathbf{T} \cdot \hat{\mathbf{n}}$$

is the power flow density in the  $\hat{\mathbf{n}}$  direction of an acoustic waveguide and

$$\mathbf{P} = -\mathbf{v} \cdot \mathbf{T} \quad (3.17)$$

is the **acoustic Poynting vector** [ $W/m^2$ ].

In the case of 2DMRs, the anchors can be treated as acoustic waveguides as they are not directly piezoelectrically excited and the  $P_s$  and  $P_d$  terms in eq.3.16 can be neglected as no acoustic energy is generated or dissipated *inside* the supports [24]. Finally, under steady state conditions,  $U$  is constant and hence eq.3.16 reduces to:

$$\oint_S (\mathbf{v} \cdot \mathbf{T}) \cdot \hat{\mathbf{n}} dS = 0. \quad (3.18)$$

Eq.3.18 states that the total power flow through the acoustic waveguides surface (i.e. the anchors surfaces) is null; in other words, the power flow through the anchors surface facing the resonator ( $S_{res}$ ) and the anchors surface facing the released area ( $S_{rel}$ ) are equal:

$$\int_{S_{res}} (\mathbf{v} \cdot \mathbf{T}) dS = \int_{S_{rel}} (\mathbf{v} \cdot \mathbf{T}) dS. \quad (3.19)$$

Thanks to eq.3.19, it is possible to compute the acoustic energy lost due to leakage through the support tethers by evaluating the power flow through one surface. Indeed, the energy can be computed by integrating the power over one period of vibration:

$$E_{lost} = 2 \cdot \int_0^T \int_{S_{rel}} (\mathbf{v} \cdot \mathbf{T}) dS dt, \quad (3.20)$$

where the factor 2 takes into account the contribution from both the anchors. A 3D model including fixed constraints at the edge of the released area has been built as a first extreme case that considers a unitary reflection coefficient  $\Gamma$ . The energy lost through the anchors has been evaluated integrating the displacement and stress product (i.e., the Poynting vector) along the surface of the anchor for different anchor lengths:

$$E_{lost} = \iint_{S_{rel}} (-\mathbf{u} \cdot \mathbf{T}) \cdot \hat{\mathbf{n}} dS. \quad (3.21)$$

Together with the energy lost through leakage, the energy stored in the resonator active volume ( $V$ ) has been evaluated by integrating the double dot product of the stress and strain tensors [24]:

$$E_{stored} = \iiint_V \mathbf{T} : \mathbf{S} dV. \quad (3.22)$$

Finally, the quality factor  $Q$  at the 2DMR resonance frequency has been evaluated, according to eq.1.44, as:

$$Q_{FC} = \frac{E_{stored}}{E_{lost}} \quad (3.23)$$

where the  $2\pi$  factor is not present because the Poynting vector is here represented in terms of displacement instead of velocity to be more easily computed in the *solid.Mechanics* framework. A schematic representation of the COMSOL<sup>®</sup> model is shown in fig.3.4.

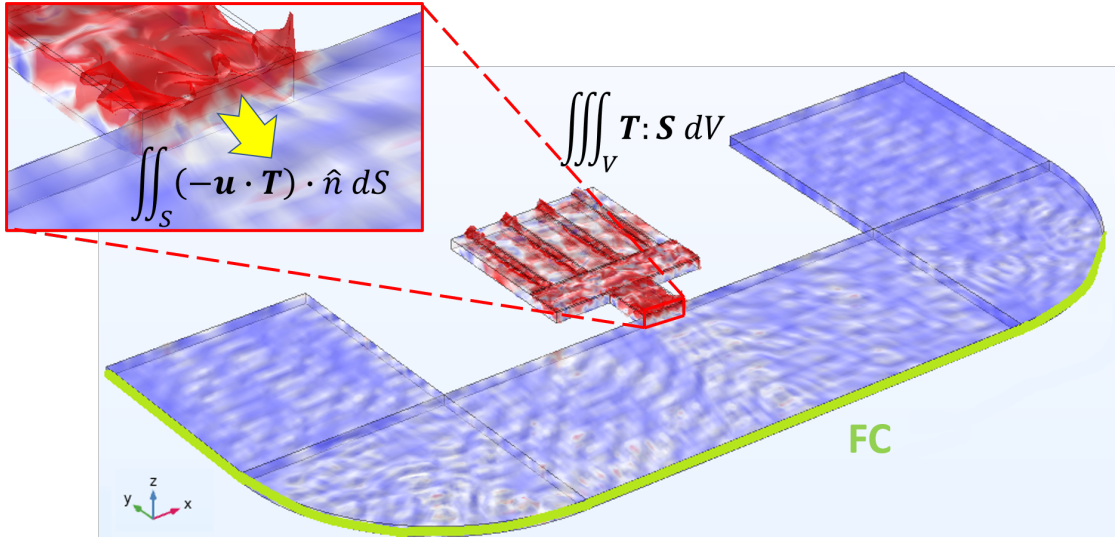


**Figure 3.4:** *FEM simulation of a 2DMR assuming FC at the edges of the released area.  $E_{stored}$  is computed over the resonator and anchors volumes whereas  $E_{lost}$  is computed over the anchors/substrate interfaces through the acoustic Poynting's vector.  $\mathbf{T}$ ,  $\mathbf{S}$  and  $\mathbf{u}$  are respectively the stress and strain tensors and the displacement vector.*

Fig.3.5 shows the results obtained from simulations in which the anchor length has been swept in a range covering one acoustic wavelength of the mode excited in the resonator. On the same plot, the values assumed by the transfer function in

eq.3.10 for the selected  $L_a$  are drawn. In coherence with the mathematical model derived above from transmission lines theory, the resonator quality factor markedly shows a periodicity with respect to  $L_a$ , reaching maximum values when  $F(L_a)$  is minimum. In fact, when eq.3.10 is minimized, the available acoustic energy at the anchors nodes is minimized too and the quality factor is thus maximized.

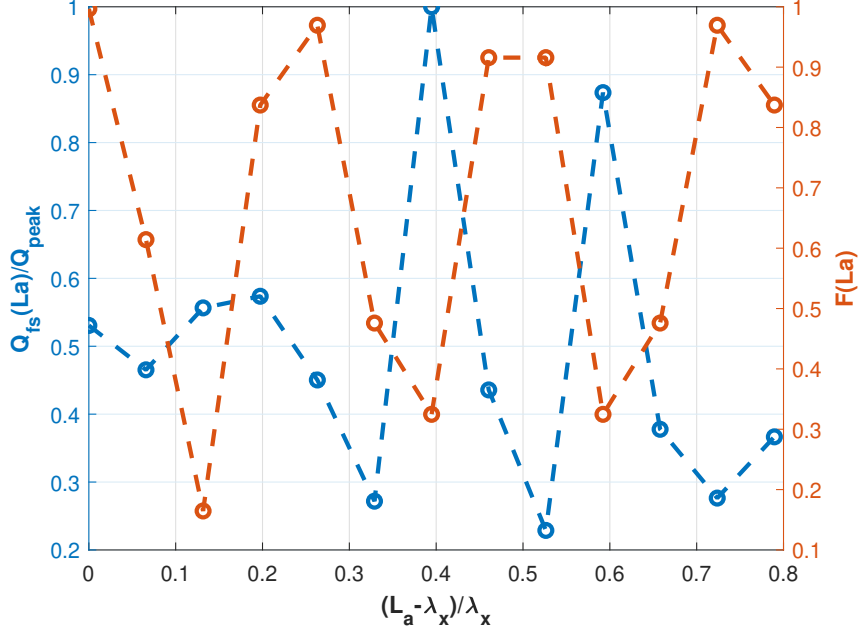


**Figure 3.5:** *function governing the dependence of the quality factor  $Q$  on anchor dimensions for fixed  $d \approx n\lambda/4$  and normalized  $Q$  values extracted from simulations for different anchor lengths.*

To check the reliability of the acoustic Poynting vector formalism, the energy lost computed with eq.3.21 is compared with the average mechanical energy flux directly extracted by Comsol across the anchors faces in fig.3.6. The two contributions show exactly the same periodicity and order of magnitude, confirming the reliability of the model and the  $\lambda/4$  periodicity predicted by analytical computations.

### PML implementation

Since the AIN substrate is typically much larger than the released resonant structure, all the elastic waves escaping from the anchors are dispersed and, as an opposite approximation to the previous paragraph, total energy dissipation can be assumed (i.e., a null reflection coefficient is inferred). This phenomenon of acoustic dissipation can be precisely modeled by the adoption of properly meshed PMLs

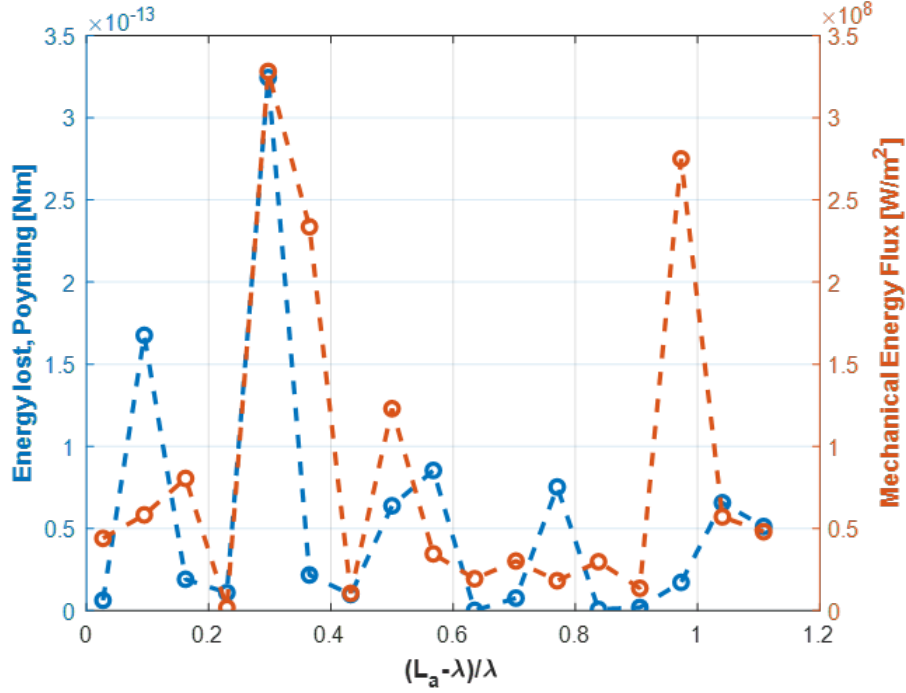


**Figure 3.6:** comparison between energy lost computed with the acoustic Poynting vector formalism and the mechanical energy flux across the anchors directly extracted from Comsol®.

surrounding the released area.

Fifty anchor configurations have been simulated with the symmetric 3D models described in the modeling section of 2DMRs operating at 3 [GHz]. The Aluminum Nitride thickness was set to 1 [ $\mu\text{m}$ ] and Molybdenum was chosen as the electrodes material with a thickness ratio of 0.15 with respect to the piezoelectric film. The *quality factors for resonance* have been extracted directly from COMSOL® for all configurations and their dependence on anchors dimensions has been studied; the simulation results are presented in the two dimensional plot in fig.3.7.

In order to ensure the reliability of simulations, a few features have been introduced in the 3D model. First of all, an ideal mechanical quality factor  $Q_{ideal} = 10000$  has been assumed for the unloaded resonator and introduced in the solid mechanics configurations through the imposition of a mechanical damping factor  $\eta = 1/Q_{ideal}$ . Moreover, in order to take into account non-idealities in the electrical domain, dielectric losses have been introduced in the model under the material specifications. The introduction of these non-idealities is necessary for COMSOL® to properly evaluate the Bode quality factor versus frequency. However,

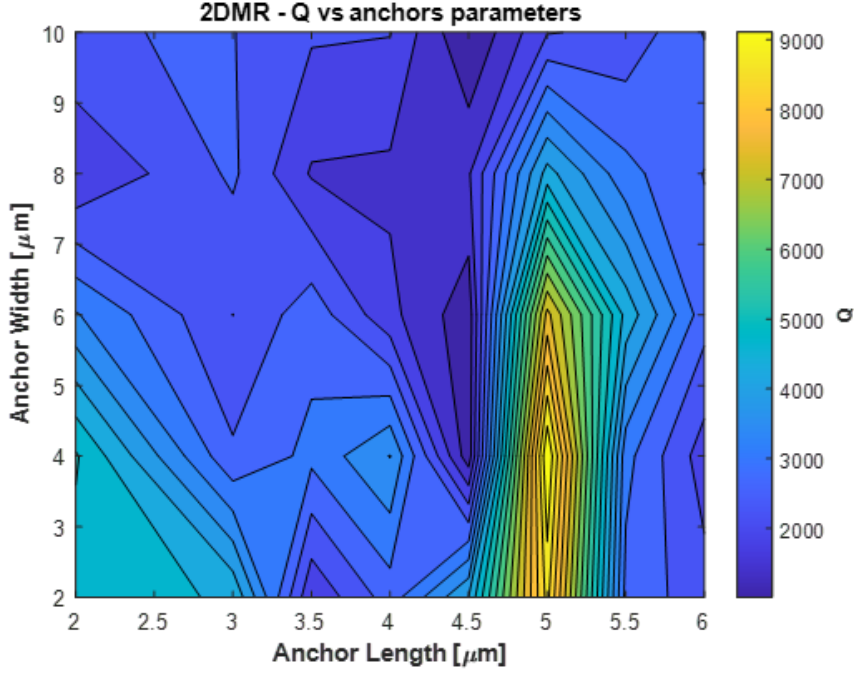


**Figure 3.7:**  $Q$  dependence on anchors dimensions. The results are from 3D simulations of short resonators exploiting the symmetry condition along their length. PMLs are included surrounding the released area..

since the focus was on the energy dissipated through anchors, the additional sources of losses have been applied to the resonator domain only, maintaining an ideal material configuration for the substrate surrounding the 2DMR.

As a means to better observe the effect of anchor losses, short resonator with a length of  $\approx 30$  [ $\mu m$ ] have been chosen, increasing the ratio between inactive and active area in the resonant architecture. Indeed, it has been proved that for resonator lengths bigger than  $50$  [ $\mu m$ ], smaller quality factor variations are observed within the same model. Since the geometric anchor parameters have been swept in a wide range, the number of mesh elements in the portion of the anchors facing the released area has been parametrically mapped so to maintain a constant density of square elements per unit of area in all the simulations. Each of the fifty simulations includes 300 frequency points between the series and the parallel frequency of the admittance plots to have a good point density in the proximity of the resonance peak where the quality factor has to be evaluated. Although it is always preferred to simulate the entire architecture of a device, as the number of computations increases, the simulation time polynomially increases, and therefore, symmetry along the resonator length has been assumed. In this way, the halving of

the domains volume compensates for the high number of configurations simulated and a denser mesh can be adopted.

According to fig.3.7, the mechanical quality factor at resonance is maximized when the anchor length is set to 5 [ $\mu m$ ]. The simulated resonators excite a wavelength  $\lambda_x \approx 3$  [ $\mu m$ ] and, assuming a slightly longer acoustic wavelength in the inactive areas, the optimal anchor length corresponds to an integer multiple of the acoustic wavelength. In fact, the following relation holds:

$$D = L_a + busW + gap \approx 11 \cdot \lambda.$$

The displacements shown by the best ( $L_a = 5$  [ $\mu m$ ],  $Wa = 4$  [ $\mu m$ ]) and the worst ( $L_a = 4.5$  [ $\mu m$ ],  $Wa = 6$  [ $\mu m$ ]) anchor configurations are compared in fig.3.8. It is evident that when the anchor is properly designed, less acoustic energy is lost into the substrate surrounding the resonator. The  $v$  components of the total displacements show that for the case with lower Q, acoustic waves propagates undisturbed in the released region, contrary to the case of the optimized configuration. The admittance responses versus frequency demonstrate how different anchor and bus configurations can impact the excitation of spurious modes. This dependence is still under investigation and experimental measurements are needed to prove the presence of any relation.

To conclude, these simulations helped the design of all the resonators studied in this thesis, giving an insight of what are the optimal anchor dimensions for resonators working around 3 [GHz].

### Complete model: Si substrate and PML

The last two subsections analysed the acoustic energy leaky via the support tethers in two opposite extreme cases where the acoustic reflection coefficient  $\Gamma$  at the edge of the released area was considered as unitary (FC approximation) and null (PMLs approximation). In a real implementation, the Silicon substrate surrounding the resonator shows a big (but not huge) acoustic impedance compared to the one of the release region; this modifies the 2DMRs equivalent electrical circuit as shown in fig.3.9. Here,  $Z_L$  represents the acoustic impedance of the substrate surrounding the released area,  $Rl$  is the length of the released area and  $\Gamma$  is the acoustic reflection coefficient. The impedance seen at node **a** is now described as:

$$Z_{in} = Z_0 \left( \frac{Z_L + jZ_0 \tan(kD)}{Z_0 + jZ_L \tan(kD)} \right) \quad (3.24)$$

and eq.3.8 can be written, in a more general form, as:

$$E_{av} = \frac{V^2}{4Z_0} \frac{(Z_0^2 - Z_L^2)}{(Z_0 + Z_L)^2} |\sin(2kd + 2kL_a + 2kRl)| \quad (3.25)$$

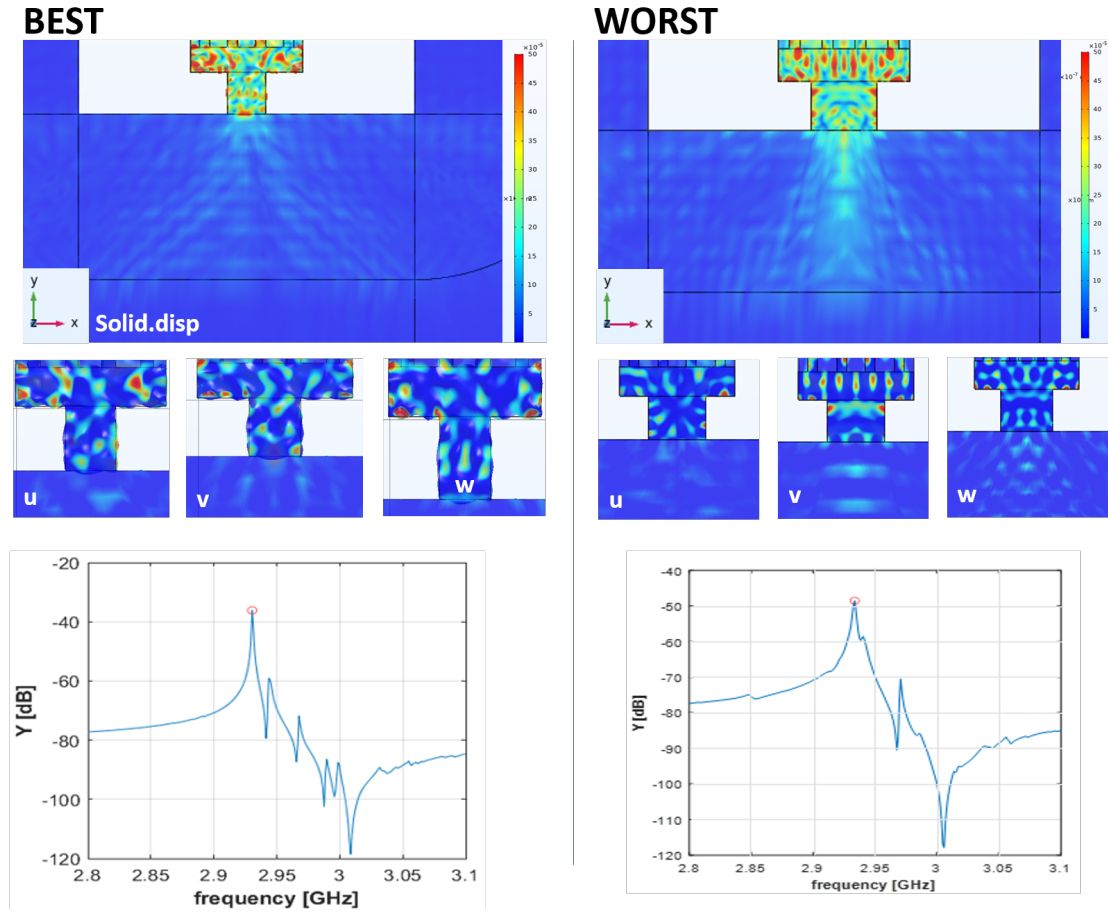


**Figure 3.8:** comparison between the displacement induced at resonance with the best anchor configuration and the worst one. Displacements along  $u$ ,  $v$  and  $w$  are compared together with the admittance responses vs frequency.

According to eq.3.25, the periodicity of the energy versus the acoustic waveguide length is the same found for the case with fixed boundary constraints, but the magnitude of the energy strictly depends on the acoustic mismatch between the two regions.

The complete 3D model built to fully characterize the energy reflection occurring at the released area edge is shown in fig.3.10 together with the optimized mesh adopted for simulations. Perfectly matched layers have been introduced both at the top and bottom of the Silicon substrate to partially absorb the radiated acoustic waves. A detailed sweep on anchors length has been carried on with an high density of frequency points to ensure the reliability of the simulations. The results for the energy lost through the supports computed with the Poynting vector formalism

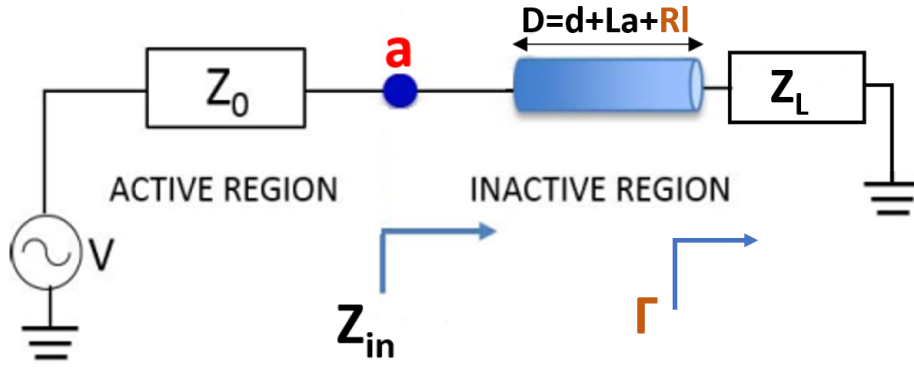


**Figure 3.9:** equivalent electrical circuit of the active and inactive region comprising the Si substrate surrounding the released area.

and the quality factor extracted by Comsol are shown in fig.3.11. The simulated points are superimposed with the analytical function governing eq.3.25 which is characterized by a  $\lambda/4$  periodicity. Also in this case, a good agreement between the simulated and predicted results is achieved, validating the analytical model used to characterize the anchor losses in 2DM resonators.

The time needed to obtain the data of fig.3.11 exceeds five hours of computation, making it difficult to use this model for fast anchors designs. However, since the model applies both the Solid.Mechanics and Electrical Comsol modules to the entire architecture of the resonator and surrounding substrates, it reaches a level of complexity that can be useful for building precise simplified models. In fact, a purely acoustic model that does not include the piezoelectric relations has been built to study the anchors as acoustic waveguides and verified by comparing the results with the ones here presented. Since in this case the displacement is induced by pressure conditions and only one physics is included, computational times of a few minutes are achieved. Moreover, user defined acoustic impedances can be defined as boundary conditions in the acoustic module and their values can be extracted from the complete model that is here proposed, making it possible to substitute entire blocks by equivalent acoustic boundary conditions. To conclude, the presented study not only characterizes the behaviour of anchor losses in 2DMRs and S1 based Lamb resonators, but also gives important reference data to build purely acoustic models characterized by low computational efforts for fast resonators and anchors designs.

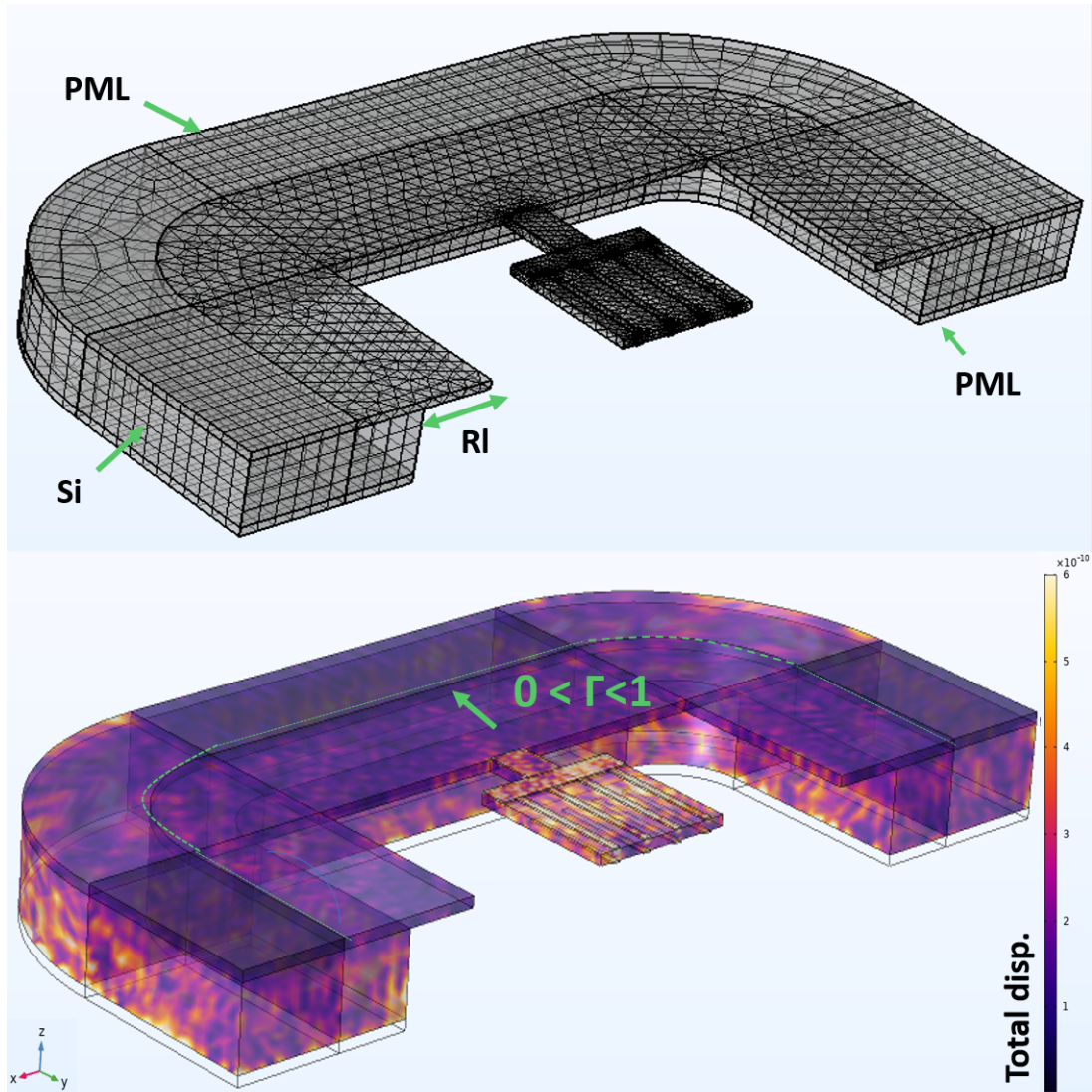


**Figure 3.10:** complete 3D model including the Si substrate and PML layers. The introduction of the surrounding substrate enables acoustic reflection at the edges of the released area, limiting the approximations introduced by fixed constraints and PMLs. The thin PMLs included at the top and bottom of the Si domains ensure partial absorption of acoustic energy by the surrounding substrates.

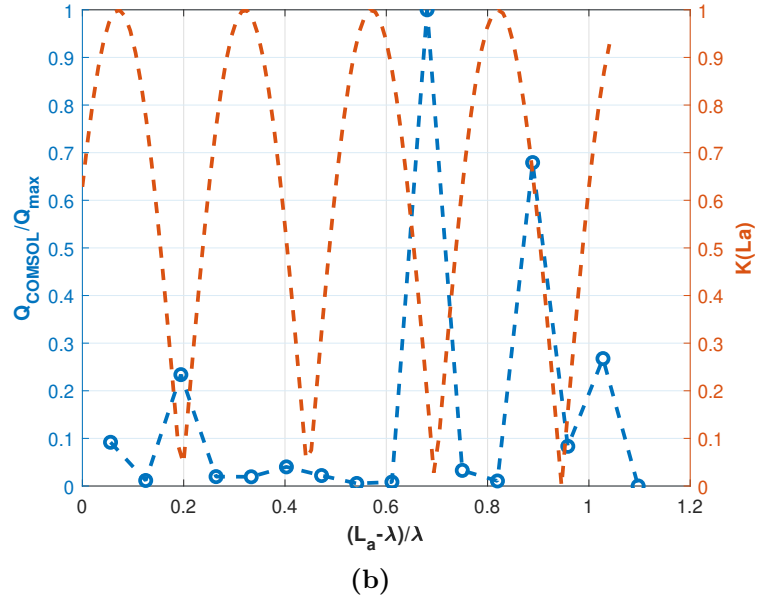
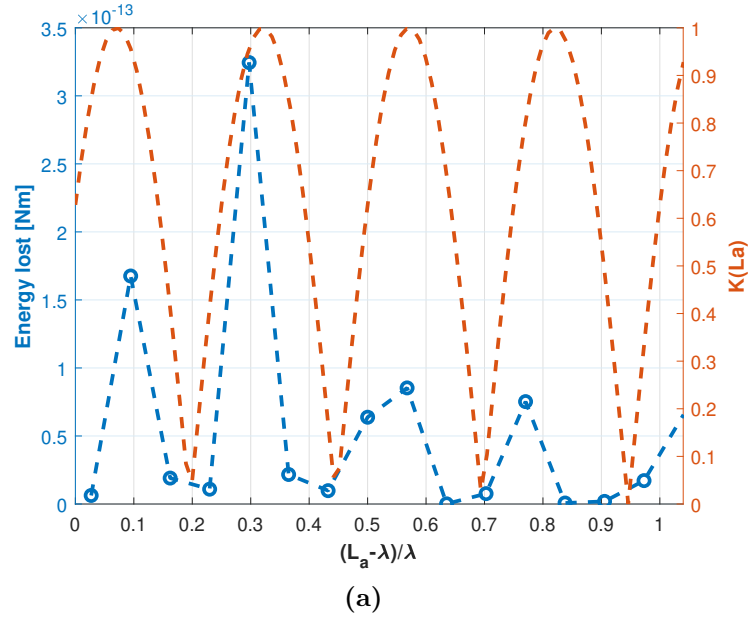


**Figure 3.11:** (a) energy lost through anchors computed with acoustic Poynting vector vs normalized anchor lengths (b) quality factor extracted from Comsol vs normalized anchor lengths. Both the energy variation and  $Q$  show the same periodicity as the analytical function  $K(La)$ .

### 3.2 2D Mode Multimodal Resonators

In previous works, 2DMRs with electromechanical coupling exceeding 4.9% at ultra high frequencies have been demonstrated [13], [16]. It has also been discussed how the electromechanical coupling of these resonators can be improved with the introduction of active and inactive metallic frames that enable a multimodal excitation and a *quasi-square displacement* in the active areas [30][18]. However, this approach introduces additional steps in the fabrication as framed electrodes are needed, increasing the complexity of the manufacturing process. The aim of this study is to investigate how the 2DMR  $k_t^2$  can be improved without further complicating the manufacturing process.

The conventional 2DM mode is a combination of both lateral and longitudinal vibrations, but since the  $d_{33}$  coefficient is larger than  $d_{31}$ , the largest stress is shown along the vertical direction. Lateral and longitudinal vibrations inside the plate can be interpreted according to Lamb's solutions as  $S1$  and  $S0$  modes, being respectively the first symmetric mode and the fundamental zero order symmetric mode. These are characterized by different mode shapes (fig.3.12) where the  $S1$  can be thought as an array of thickness extensional unit cells and the  $S0$  shows an alternation of compression and expansion zones along the plate width.

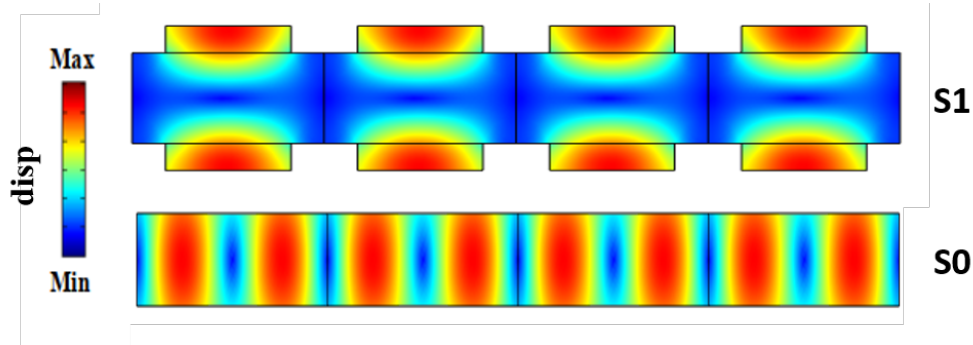


**Figure 3.12:** *first and zero order symmetric Lamb waves mode shapes.*

From the point of view of the 2DMR admittance response, it is generally possible to distinguish two resonances around the center frequency with mode shapes referable to the  $S1$  and  $S0$  modes. The two modes generally appear at different frequencies so that they can be independently described, but the most coupling goes to the first symmetric mode thanks to the direct excitation of the  $d_{33}$  as shown by the FEA results in fig.3.13. However, when specific design rules are met, the first two resonances of fig.3.13 couple in a unique resonance enhancing the  $k_t^2$ . This feature has been investigated through COMSOL<sup>®</sup> 2D simulations by sweeping the electrodes width and relative spacing so to excite waves with different

wavelengths and monitoring the  $k_t^2$  variations of the main S1 resonance.

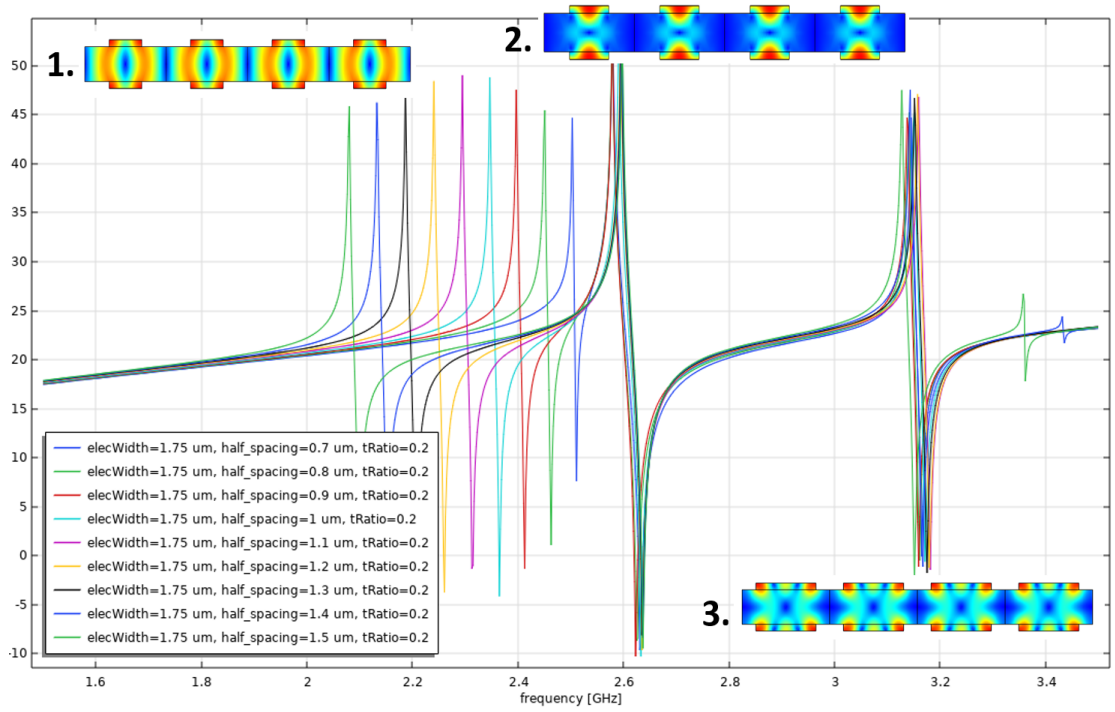


**Figure 3.13:** simulated admittance response from a 2D model showing the (1.) S0, (2.) S1 and (3.) S1 overtone excitation at different frequencies. The main contribution goes to the S1 (2.) resonance.

The results from simulations including Molybdenum and Platinum as electrode materials are respectively collected in figs.3.14 and 3.15 as sets of two-dimensional plots, where the colour indicates the electromechanical coupling coefficient. Local  $kt^2$  maxima up to 6.7% are recognizable for specific electrode width and spacing combinations in both cases, overcoming the usual 2DMR performances. This is an interesting result because demonstrates that, by properly designing the electrodes pattern of a "classical 2DMR", the same  $k_t^2$  of CLMRs and CBARs can be reached implementing wider electrodes.

To explain the maxima appearing in the plots of figs.3.14 and 3.15, a deeper investigation of the dispersion relations and mode characteristics is needed. The optimum wavelength (or lateral wave number) at which the coupling of each Lamb mode is maximized in the material stack adopted has been derived from the computation of the piezoelectric electromechanical coupling coefficient  $K^2$ . Fig.3.16 shows the  $K^2$  for the first two symmetric modes together with the zero

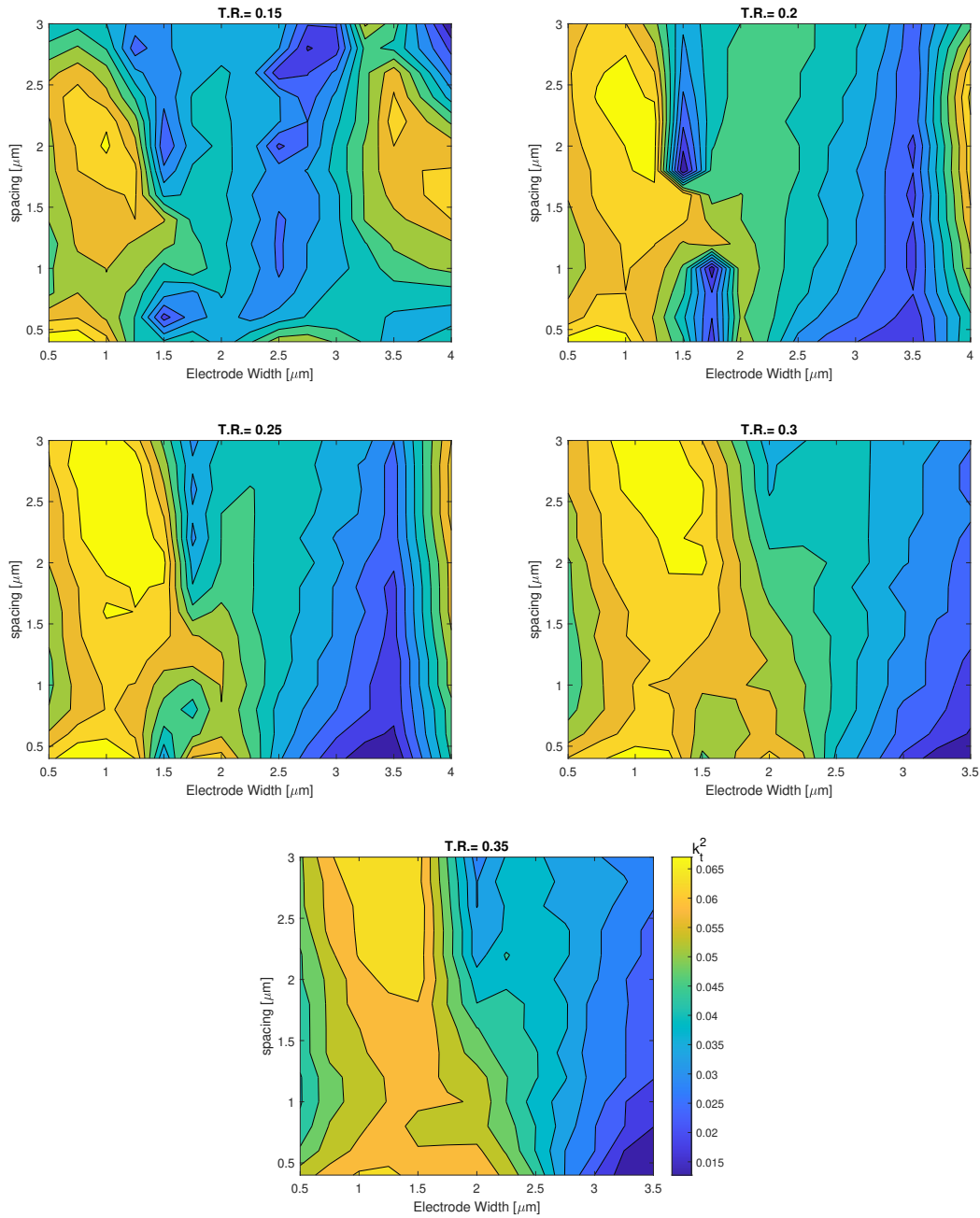


**Figure 3.14:**  $k_t^2$  dependence on electrodes width and electrodes spacing in 2DMRs with Molybdenum electrodes. Results are presented for different ratio between the electrode and Aluminum Nitride thicknesses.

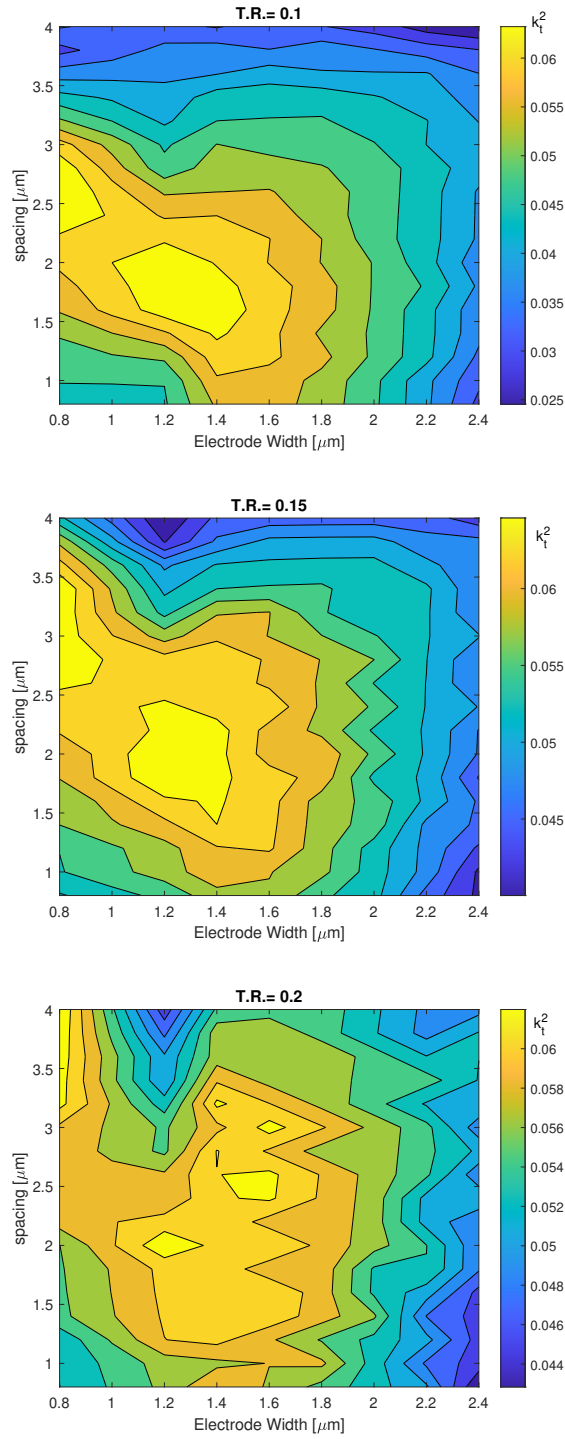


**Figure 3.15:**  $k_t^2$  dependence on electrodes width and electrodes spacing in 2DMRs with Platinum electrodes. Results are presented for different ratio between the electrode and Aluminum Nitride thicknesses.

order anti-symmetric mode evaluated from the dispersion curves computed with COMSOL<sup>®</sup> at both the resonance and antiresonance frequencies for the AlN/Mo configuration. The plot shows the maximum electromechanical coupling achievable by the acoustic modes and demonstrates that the  $S1$  and  $S0$  maxima are achieved at different  $k_x$ . This suggests that in order to design a device with maximized  $S1$  coupling, a  $k_x$  below the dilatational point (i.e.,  $k_x \approx 1.5 [\mu m^{-1}]$ ) should be excited by the electrodes configuration. Doing this way, not only the  $S1$  direct excitation would be optimized, but the  $S0$  coupling would be minimized at the same time.

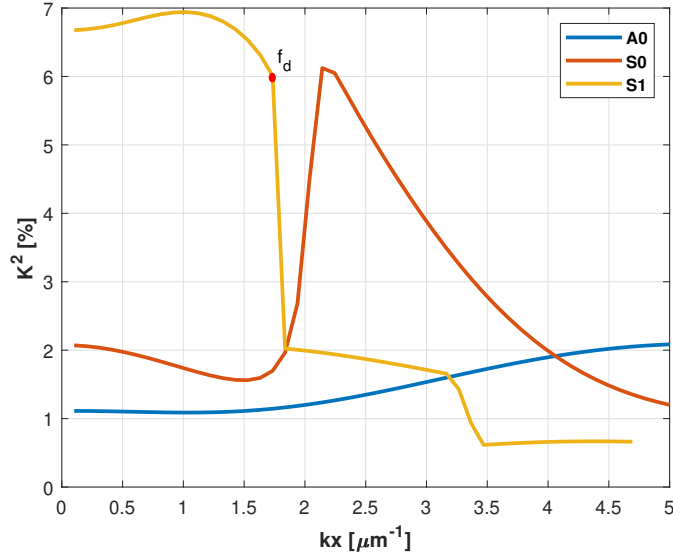


**Figure 3.16:** piezoelectric coupling factor for the  $A0$ ,  $S0$  and  $S1$  modes; the red point refers to the  $k_x$  related to the dilatational frequency of the  $S1$  mode ( $f_d$ ). These results have been evaluated from the dispersion curves derived from FEM 2D simulations.

The numerical results shown in fig.3.16 refer to the ideal case where no boundaries are imposed to the plates. But in real finite structures, the highest electromechanical coupling coefficient for the  $S1$  mode cannot usually exceed 5% because of the confined displacement. With this consideration in mind, the explanation of the high  $k_t^2$  values found in simulations should be searched by looking at possible multiple modes interactions that change the usual physical behaviour expressed by the first order thickness extensional mode alone.

In the following, the plot of fig.3.15 with  $T.R. = 0.15$  is taken as a case study to derive the 2DMR behaviour at the points of maximum  $k_t^2$  as this is the configuration adopted for the main experimental plan of this work (i.e.,  $AlN_{thickness} = 1 [\mu m]$ )

and  $Pt_{thickness} = 150$  [nm]). For an electrode width of  $\approx 1.3$  [ $\mu m$ ], the highest  $k_t^2$  value is achieved when two resonances merge into a single one and this occurs for a spacing  $s \approx 2.4$  [ $\mu m$ ]. With this arrangement, the main resonance shows a mode shape like the one in fig.3.17, where the  $S1$  and  $S0$  contributions sum in a constructive way. This only happens for specific spacings that are inversely proportional to the electrodes width and the optimal ratio between the electrodes width and spacing is a function of the materials and their thicknesses, as the phase velocities of the modes are strongly dependent on these parameters [1].

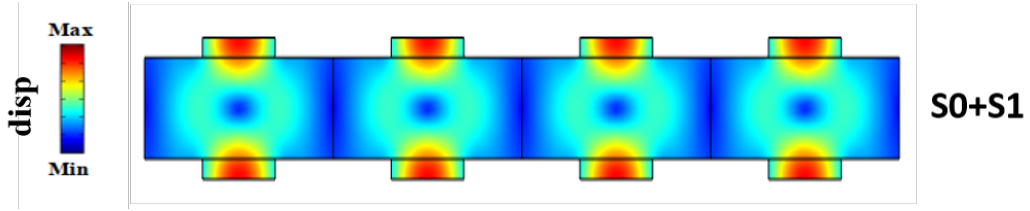


**Figure 3.17:** 2DMR mode shape observed for the optimal electrodes width and spacing combinations.

The admittance response from a 3D model including PML and optimized anchoring supports of a 2DMR with Molybdenum electrodes and optimized parameters extracted from fig.3.14 is plotted in fig.3.18 together with the equivalent electrical values derived from the BVD model fitting. The admittance plot is precise and clean if compared to the 3D models of not optimized structures, with some weakly excited spurious modes between the resonance and antiresonance frequencies. Similar resonances are obtained from 3D simulations of each maximum  $k_t^2$  region of figs.3.14 and 3.15.

From a geometrical point of view, when the active and inactive areas are wide enough to respect the displacement induced by the  $S0$  mode at the resonance frequency (i.e., they are comparable with the  $S0$  wavelength at  $f_s$ ), the two eigenvalues from Lamb's problem relative to the  $S1$  and  $S0$  eigenfunctions reactively couple into a unique solution enhancing the electromechanical coupling of the two-dimensional mode. Interesting considerations can be done by looking at the dispersion curves of the first modes propagating in the uncovered and covered areas of the optimized Pt configuration case study (i.e., IA and AA) plotted in fig.3.19. The curves show that for  $E.W. = 1.3$  [ $\mu m$ ], a  $k_{x,S1} \approx 2.3$  [ $\mu m^{-1}$ ] is excited at  $f_s = 2.2$  [GHz], being  $\lambda_{x,S1} \approx 2 \cdot E.W.$  At the same resonance frequency, the  $S0$  mode propagating in the inactive areas shows a  $k_{x,S0} \approx 1.3$  [ $\mu m^{-1}$ ] and, considering a spacing  $s = 2.4$  [ $\mu m$ ] the following phase relation holds for the

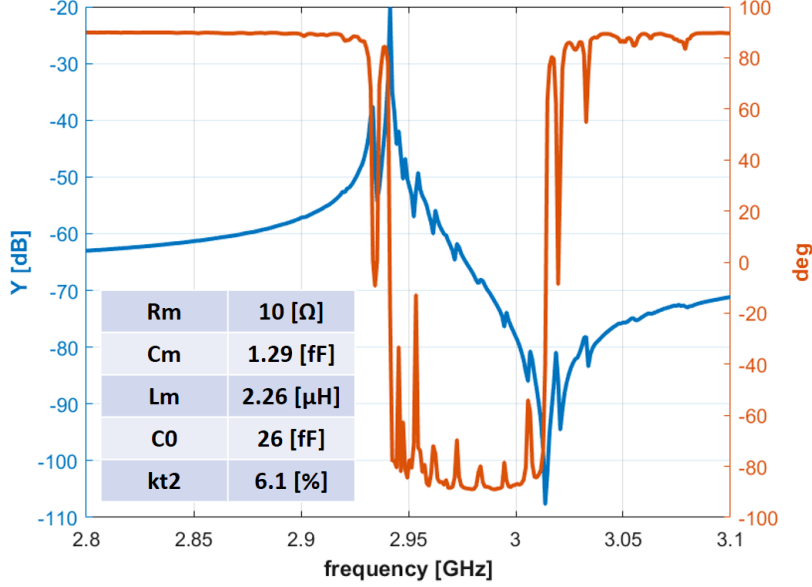


**Figure 3.18:** module of the admittance response vs frequency and phase for an optimized Mo/AlN 2DMR with  $E.W. = 1$  [μm] and spacing = 2 [μm] obtained from a 3D simulation. Electrical parameters extracted from the BVD model are listed in the inset.

horizontal displacement:

$$\begin{aligned}
 \Delta\phi_{S1}(AA) &= k_{x,S1} \cdot AA \approx 2.4 \cdot 1.3 \approx \pi \\
 \Delta\phi_{S0}(IA) &= k_{x,S0} \cdot IA \approx 1.3 \cdot 2.4 \approx \pi \\
 \Delta\phi(p) &= \Delta\phi_{S1}(AA) + \Delta\phi_{S0}(IA) \approx 2\pi
 \end{aligned} \tag{3.26}$$

The phase relation in eq.3.26 confirms how the two solutions of the Lamb's problem can reactively couple into a periodic mode shape with wavelength  $\lambda_x \approx W_e + s = p$ . It is important to notice that the main contribution is still given by the  $d_{33}$  coefficient, but for precise inactive area widths, the horizontal displacement induced by  $d_{31}$  matches the  $S0$  wavelength enhancing the energy density at the active area boundaries.

Indeed, from a mechanical point of view, this can be seen as a change of boundary conditions at the active areas edges induced by the lateral components of the acoustic wave. The extensional mode does not show an exponentially decreasing evanescent displacement as it usually does in 2DMRs because portion of the acoustic energy is coupled with horizontal displacement induced by the  $S0$  mode. By relaxing the fingers constraints, more displacement is induced at the electrodes edges, hence increasing the motional capacitance  $C_m$  with respect to usual 2DMRs with

the same  $C0$ . This enables a more efficient electromechanical transduction that ultimately ends in boosting the  $k_t^2$  of the main resonance mode. Due to this particular feature enabled by the interaction of multiple modes, we call these optimized 2DMRs as **Two-Dimensional-Mode-Multimodal-Resonators** ( $2DMRs^M$ ).

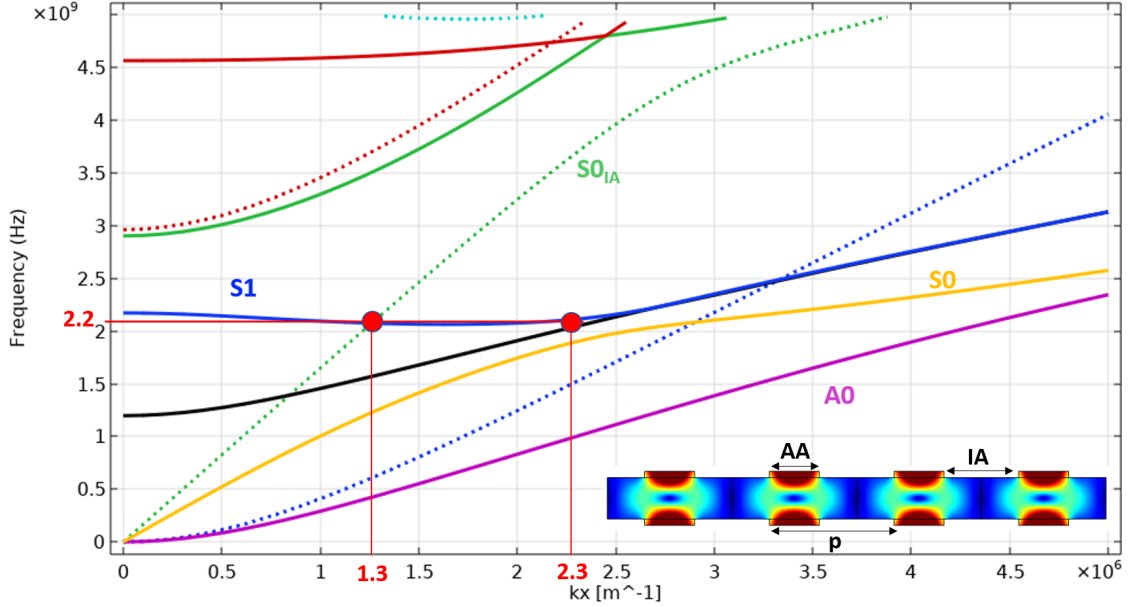


**Figure 3.19:** simulated dispersion curves for active (AA) and inactive (IA) areas of a 2DMR with  $AlN_t = 1$  [ $\mu m$ ] and  $Pt_t = 150$  [ $nm$ ]. Continuous lines refer to AA whereas dotted lines refer to IA.

Fig.3.20 compares the stored energy densities in the active and inactive regions of 2DMRs sharing the same electrode width  $EW = 0.8$  [ $\mu m$ ] but with different spacings. The graphs demonstrate that when the optimal spacing is set, the energy gets locally stored under the electrodes only, showing how the S0 contribution is actually effective by maximizing the S1 induced displacement instead of exciting significant acoustic components in the inactive areas. Furthermore, when the spacing is made larger, significant energy storing between the fingers is observed and the S1 coupling is significantly decreased.

The frequency tunability of the optimized devices can be derived from the four dimensional plot in fig.3.21, where the  $f_s$  curve is plotted versus the geometrical parameters of the electrodes grating. The colour of the plot indicates the electromechanical coupling coefficient computed for each configuration. According to the simulated results, a frequency tunability of 11% around the central frequency can

be achieved for  $k_t^2$  values above 5%:

$$\frac{\Delta f}{f_{s, \text{central}}} \approx 11\% \quad \text{with} \quad k_t^2 > 5\%, \quad (3.27)$$

being this value comparable to the one characterizing the framed-2DMRs [18].

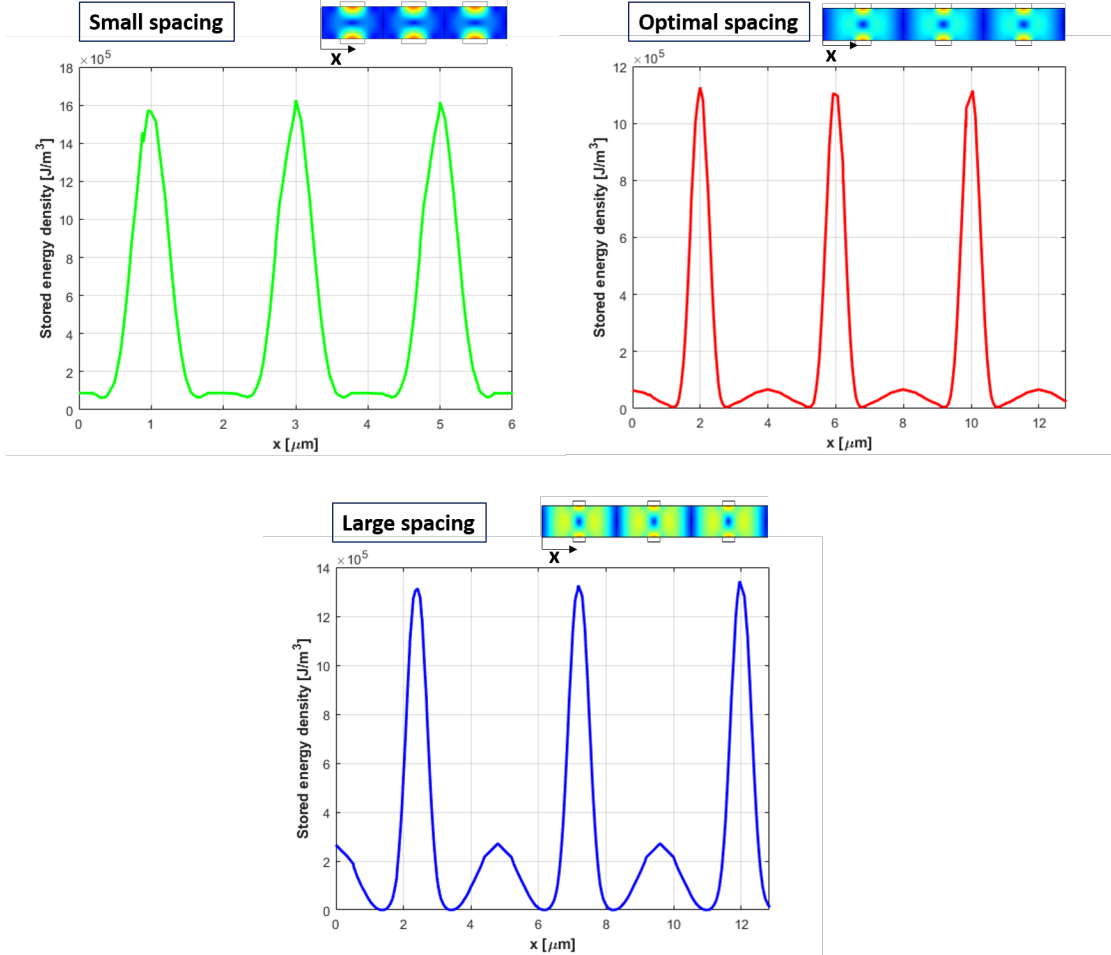


**Figure 3.20:** comparison of the stored energy density along the section of Pt/AlN 2DMRs with  $EW = 0.8 \text{ } [\mu\text{m}]$  and different spacing values. Small and large spacings refer to minimum and maximum values included in the plots of fig.3.15.

Finally, it should be noticed that the boosted  $k_t^2$  due to the S1/S0 reactive coupling cannot be seen for electrode widths much higher than the thickness of the piezoelectric layer (i.e.,  $EW \gg h_{AlN}$ ) because this is the value above which overtones of the S1 mode get excited with significant coupling within the active areas. Indeed, when wide electrodes are implemented, multiple resonances equally

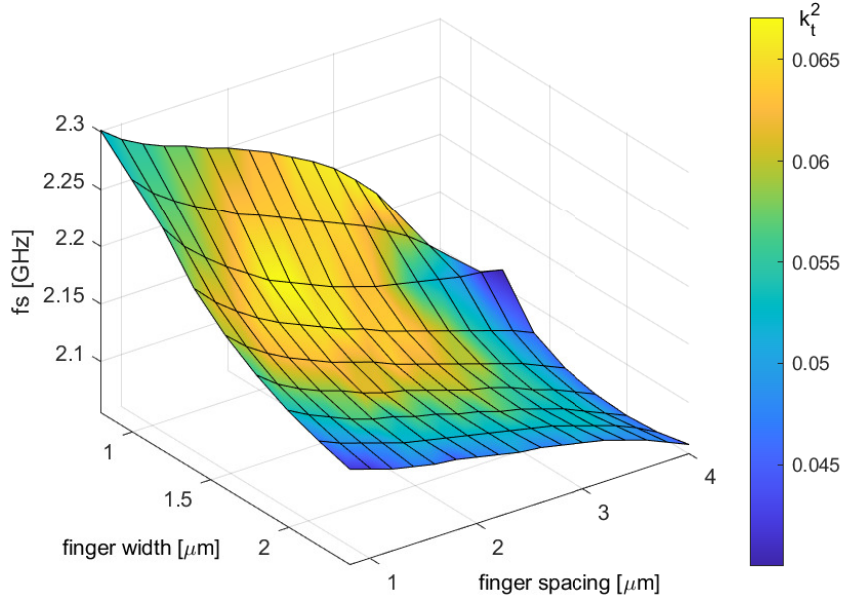


**Figure 3.21:** resonance frequency dependence on the geometrical parameters of the electrode gratings. The colour refers to the magnitude of the electromechanical coupling coefficients.

spaced in frequency appear; their wavelength is a fraction of the main mode wavelength and the electromechanical performances are considerably degraded. According to the results from hundreds of 3D and 2D, empirical design rules for  $2DMRs^M$  have been derived and checked in a wide frequency range (i.e., for a multitude of AlN thicknesses) extending from 800 [MHz] to 5 [GHz]. The precise ratio between the electrode width and the spacing depends on the materials adopted for the top and bottom electrodes and on their thicknesses, as these are the main features affecting the phase velocities of the modes under interest. As a general rule, the phase condition expressed by eq.3.26 should be matched to get the reactive interaction that boosts the performances. More in general, the following relation needs to be satisfied:

$$k_{x,S1} \cdot E.W. + k_{x,S0} \cdot s = 2\pi \quad (3.28)$$

where E.W. is the electrode width and s the spacing between electrodes. For a given electrode configuration chosen to minimize the electrical loading, the optimal spacing is directly derived:

$$s = \frac{2\pi - k_{x,S1} \cdot E.W.}{k_{x,S0}} \quad (3.29)$$

To numerically find the optimized arrangement, a complete analytical description that goes beyond the purpose of this work would be needed. However, the condition of eq.3.29 can be satisfied by studying the dispersion curves for the  $S1$  and  $S0$  modes as shown above. Finally, as an empirical rule to quickly check the  $k_t^2$  optimization, the optimal configuration for different materials can be found by running a detailed 2D FEM analysis around the following approximated values:

$$\begin{aligned} EW &\approx h_{AlN} \\ spacing &\approx 2 \cdot EW. \end{aligned} \tag{3.30}$$

### 3.3 Bottom plate resonators

When the Aluminum Nitride is grown on the metal electrodes, residual stress is usually observed in the film because of steps at the base of the substrate. The film defects become more and more relevant when the thickness is reduced to values comparable with the one of the electrodes. The implementation of a grounded bottom electrode plate (BP) instead of patterned metal fingers simplifies the fabrication process ensuring a better Aluminum Nitride conformity and less residual stresses. However, as previously demonstrated by Zou et al. in [1], when a continuous metal layer is adopted as the bottom electrode, the  $k_t^2$  is generally reduced because of the strong loading effect induced. The BP provides backside electrical boundaries that are needed for an effective excitation of the piezoelectric layer, but the direct excitation of half wavelength of the  $S1$  mode relies on the top patterned electrodes geometry. Indeed, from a mechanical point of view, the bottom plate acts as an acoustic load for waves propagation, making it more difficult to design the  $S1/S0$  modes combination derived in the previous study. The mode shape of a 2DMR implementing a bottom plate is shown in fig.3.22 in terms of total displacement and Mises stress. It reflects the original 2DMR thickness extensional mode shape showing a well confined displacement in the active areas.

In order to limit the acoustic loading preserving high  $kt^2$  values, it is usually preferred to have a thin and light metal as the bottom substrate rather than a heavy one. Generally speaking, the choose of the metal thickness should be done so to maximize the mechanical displacement inside the piezoelectric film. If a thin bottom metal plate is employed as a base for AlN growth (e.g.,  $t_e/h_{AlN} < 0.2$ ), the aforementioned condition can be satisfied by selecting a top metal with large acoustic impedance with respect to the piezoelectric layer. This feature is especially true for sufficiently thick piezoelectric films compared to the acoustic wavelength excited (i.e.,  $h_{AlN}/\lambda > 0.2$ ) [1].

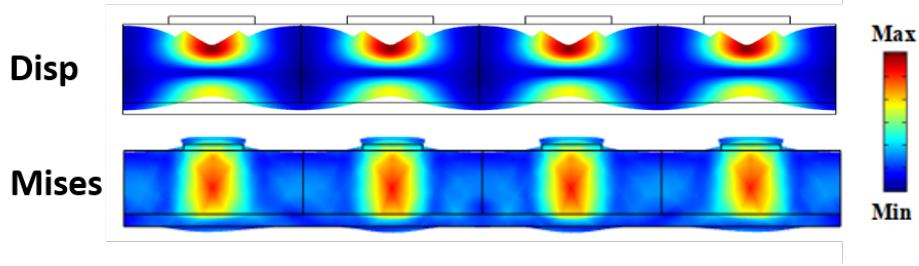
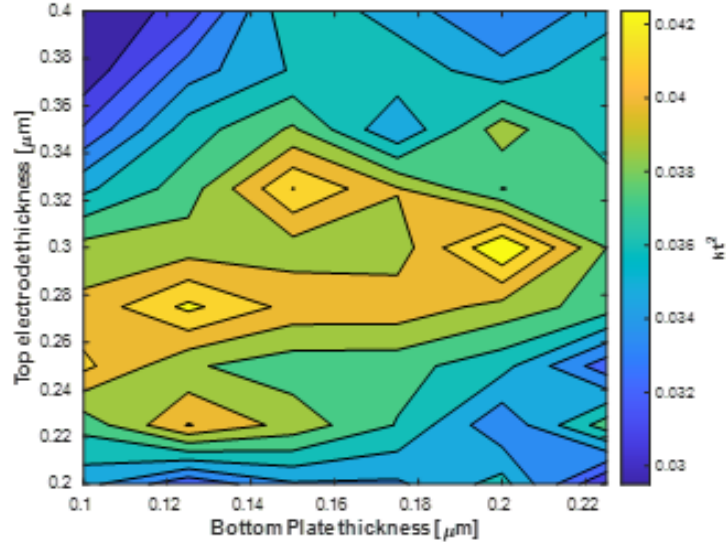


**Figure 3.22:** 2D FEM model of a 2DMR with a bottom plate electrode instead of patterned bottom electrodes. The mode shapes are similar to the one of classical 2DMRs.

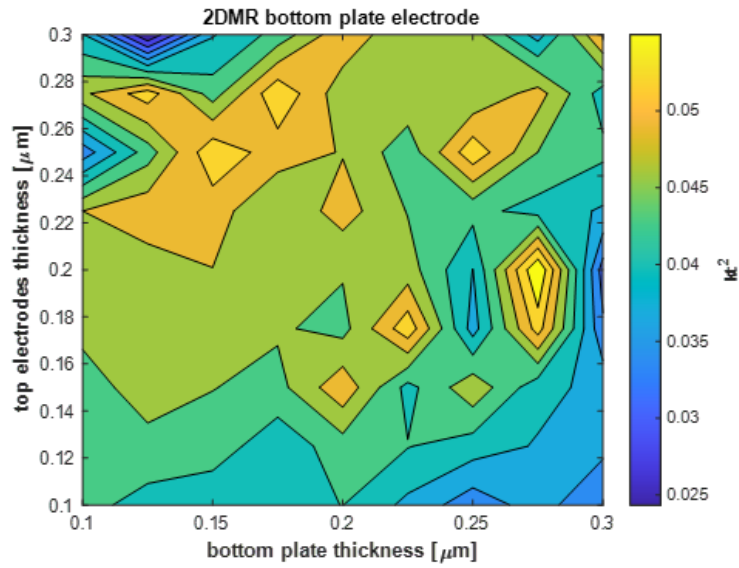
Fig.3.23 shows the  $k_t^2$  values obtained for the  $S1$  thickness extensional mode excited in a 2DMR with different bottom and top electrode thicknesses. In these simulations, Platinum has been chosen for the bottom electrode because it has been experimentally demonstrated to be a good substrate for the AlN growth whereas Aluminum and Molybdenum are compared as top electrodes materials. In both plots the electromechanical coupling is maximized for top electrode thicknesses smaller than the one of the bottom plate. Local maxima are distinguishable, however, they should not be given too much consideration as in this points the  $k_t^2$  is boosted by unwanted spurious modes in proximity to the main resonance. Since Aluminum is less dense than Molybdenum, slightly thicker layers are needed to get  $k_t^2$  higher than 4%. Furthermore, as summarized in fig.3.24, Molybdenum has an higher acoustic impedance than Aluminum and this explains the slightly higher electromechanical coupling coefficients shown in fig.3.23b with respect to the results in fig.3.23a.

Bottom plate 2DMRs relying on the  $S1$  mode excitation have never been demonstrated and they have been introduced for the first time in the experimental plans of this thesis. The same materials and thicknesses chosen for the other studies have been assumed for the electrodes to satisfy the layer specifications of the chip (i.e., 150 [nm] of Platinum on 1[ $\mu$ m] thick AlN). The simulated results corresponding to the configurations included in the main experimental layout are shown in fig.3.25. It should be noticed that, since Platinum has a much higher density ( $\rho_{AlN}/\rho_{Pt} \approx 0.15$ ) with respect to Aluminum ( $\rho_{AlN}/\rho_{Al} \approx 1.2$ ) and Molybdenum ( $\rho_{AlN}/\rho_{Mo} \approx 0.35$ ), this is not the optimal choice for the top electrodes and  $k_t^2$  lower than the simulated ones are experimentally expected. The dependence of the resonance frequency on the width of the electrode fingers and their spacing is plotted in fig.3.26. Compared to the case of patterned bottom electrodes (fig.3.21), the 3D plot shows the highest  $k_t^2$  for the same combinations of the two geometrical parameters; although similar  $f_s$  dependence is shown, the

curve is not smooth as in the previous case. This is related to the excitation of unwanted spurious modes that made it difficult to precisely evaluate the resonance mode under interest.



(a) Pt/AlN/Al



(b) Pt/AlN/Mo

**Figure 3.23:** computed  $k_t^2$  from simulations including different top and bottom electrode thicknesses. Results are showed for both Pt/AlN/Al and Pt/AlN/Mo configurations.

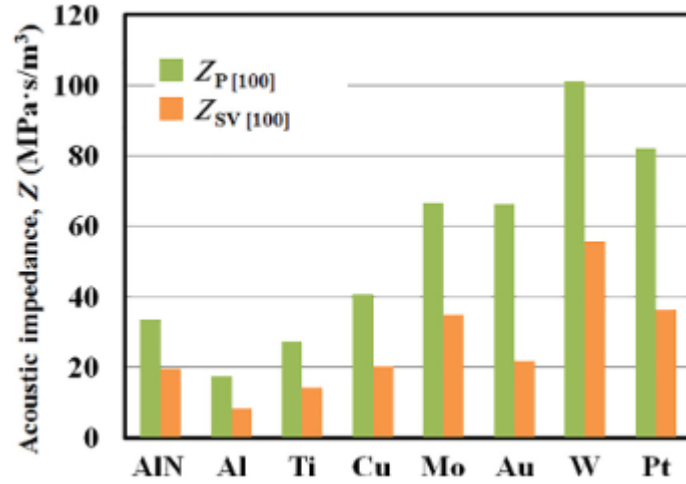


**Figure 3.24:** comparison of the acoustic impedance shown by different materials for longitudinal and vertical Lamb's waves in Aluminum Nitride thin films [1].

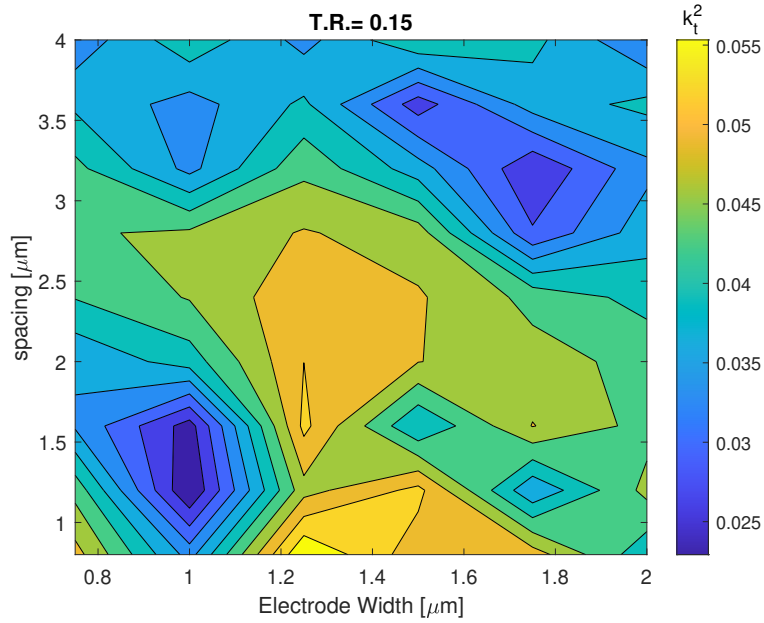


**Figure 3.25:**  $k_t^2$  dependence on top electrodes width and electrodes spacing for bottom plate 2DMRs with Platinum as both bottom and top electrodes material. The thickness ratio ( $T.R. = 0.15$ ) expresses the ratio between the Pt films and the AlN thicknesses.

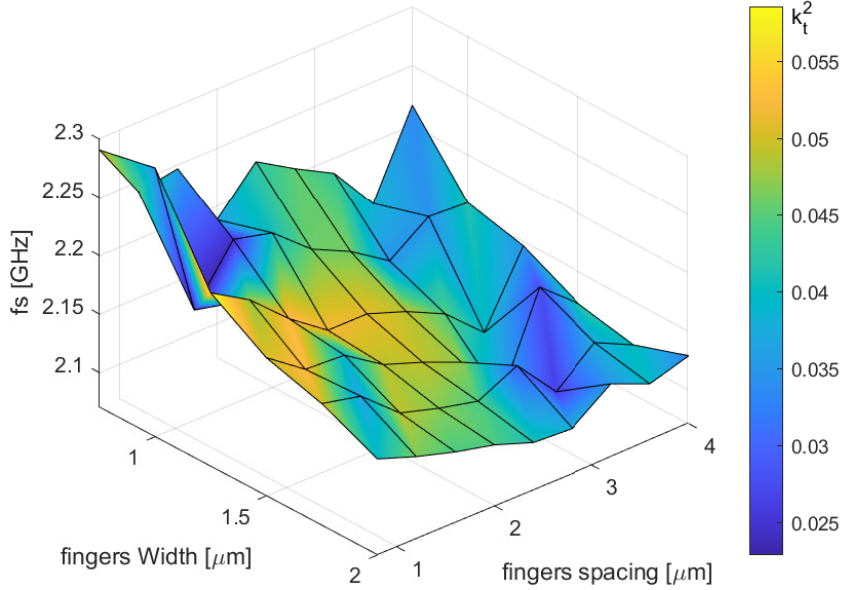


**Figure 3.26:** resonance frequency dependence on the geometrical parameters of the top electrodes in a bottom-plate Pt/AlN/Pt 2DMR; the thickness ratio between electrodes and piezoelectric film is  $T.R. = 0.15$ . The colour refers to the magnitude of the electromechanical coupling coefficients.

### 3.4 Apodization for spurious modes suppression

Unexpected spurious modes close to the main resonance can affect the resonators performances in terms of frequency selectivity and  $kt^2$ . Because of this, the ability and ease to control unwanted electrical responses while designing a resonant structure is a crucial factor to prefer a technology with respect to another one. The aim of this study is to understand how to take control of the main resonance cleanliness in 2DMRs and  $2DMR_s^M$ .

Theoretically, to reduce the effects of unwanted resonances on the electrical response of a resonating structure, it is sufficient to reduce their electromechanical coupling through a proper design. The most popular methods for modes suppression that have been proposed in the past rely on new anchors designs and on the introduction of dummy electrodes to extend the periodicity of the gratings in inactive areas [31],[32]. Again, no studies of this type have never been conducted on two-dimensional mode resonators and  $2DMR^M$ . As in the case of CLMRs, the 2DMRs active regions show different boundary conditions along the two in-plane directions and transverse spurious-modes may appear due to a larger acoustic

velocity along the length of the fingers [32]. Due to the electrodes extension along the  $y$  direction (see fig.3.27 for axis orientation), the total displacement generally shows a marked periodicity in the active area. Each "active cell" has the same dimensions and boundary conditions so that the acoustic vibrations perpendicular to the  $x$  direction (not analysable in 2D simulations) are common to each finger and gain significant piezoelectric coupling when adding up. One way to limit this behaviour is to introduce variations in the electrodes lengths; such a technique is commonly referred as *Apodization*. The concept of apodization consists of confining the vibration energy in specific regions of the 2DMR body by shaping its electrodes according to a specific geometry [31]. In this study, the electrodes of an optimized  $2DMR^M$  (i.e., with  $k_t^2 \approx 7\%$ ) with resonance frequency around 5 GHz (the highest operating frequency ever studied for such devices) have been shaped with different frames. Three main apodization geometries have been considered:

- Irregular polygon shape apodization
- Circular apodization
- Sine shape apodization,

let's analyze the results for all of them.

### **Irregular Polygon shape apodization**

In this case, the idea comes from the commercial FBAR technology. One of the main acoustic losses that occur in FBARs is related to the presence of lateral standing waves that generates when two electrodes edges are parallel to each other. When this occurs, the acoustic wave travels between the electrodes and bounces back and forth, generating the spurious modes. This effect can be seen, for example, in rectangular FBARs. This issue was historically addressed by adopting apodization i.e., designing FBARs with non-parallel edges [33]. Kumar et al. compared different apodization shapes for FBARs through 3D-FEM simulation, analyzing the  $kt^2$  and  $Q_f$  variations (i.e., the FoM). As expected, the results show that the adoption of irregular shapes with non-parallel edges enhances the device figure of merit [33]. In the case of 2DMRs, instead of modifying the whole body of the resonator, it is possible to shape the active areas only by varying the top and bottom electrodes lengths in a complementary way. Two options have been analyzed following this idea. Firstly, each electrode has been cut along its length and split into two segments separated by a small gap, one electrically connected to the bus and one left floating. In this configuration, the symmetry of the structure along  $x$  does not interrupt, but a significant parasitic capacitance is added to the system due to electrodes portions that do not actively participate in the piezoelectric excitation. In the second configuration, instead, the floating electrode segments have been

deleted resulting in a smaller static capacitance per unit of area. Fig.3.27 shows an example of irregular apodization applied to a 2DMR following the second approach. The displacement is concentrated in two regions along the length of the device, differently from the non-apodized resonator shown in fig.3.28.

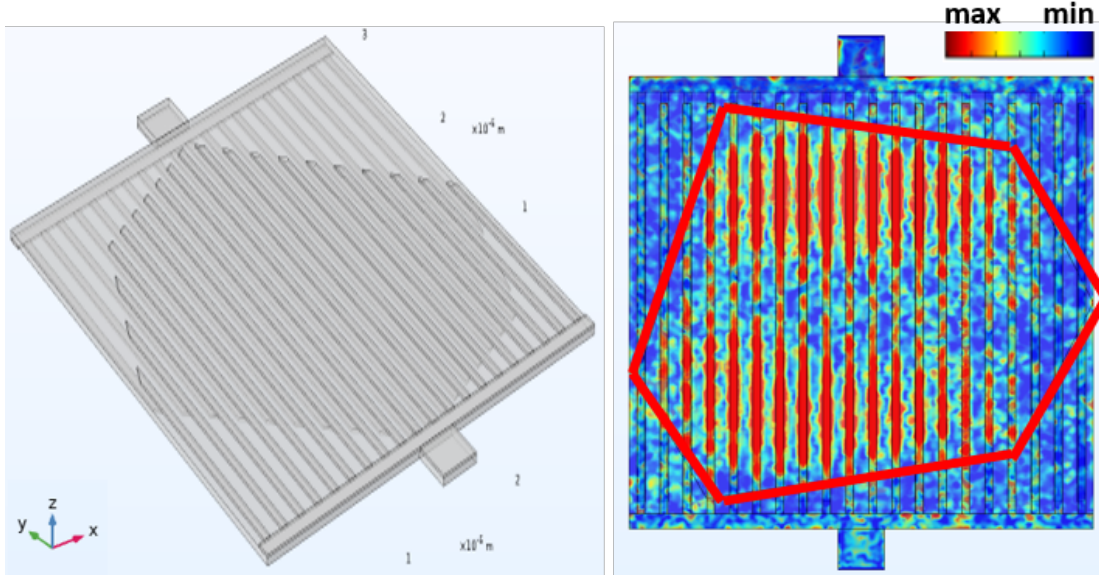


**Figure 3.27:** 3D COMSOL<sup>®</sup> model of a 2DMR with irregular apodization applied to the fingers and total displacement shown at resonance.

### Sine shape apodization

The effectiveness of the apodization in suppressing the spurious modes is dependent on the *apodization depth* (AD) adopted, defined as the ratio between apodized and not-apodized areas [34]. Several non-optimized structures (whose admittance response is significantly affected by spurious modes) with sinusoidal shaped apodization have been simulated for different sine aperture (A) values. The resulting admittance plots are shown in fig.3.29 and the relevant parameters are summarized in table 3.1 for all the configurations.

Differently from CLMRs [32], the  $k_t^2$  of 2DMRs is not affected by the magnitude of AD. This is due to the different arrangement of the electrodes that locally excite the  $S1$  mode instead of the  $S0$ . In fact, each couple of top and bottom fingers applies a vertical electric field for the entire length of the electrodes and, even when they are shaped, the entire capacitance actively participates in the electromechanical transduction. Thanks to this feature, the ratio between the motional and the static capacitance is preserved and no  $k_t^2$  variations are observed.

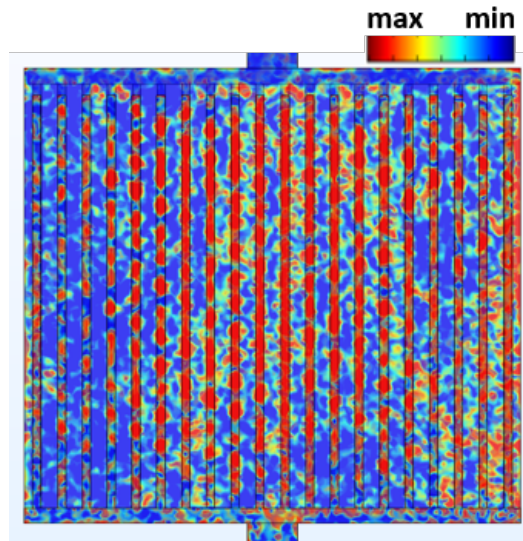


**Figure 3.28:** total displacement shown at resonance of an optimized 2DMR taken as a reference for the apodization study.

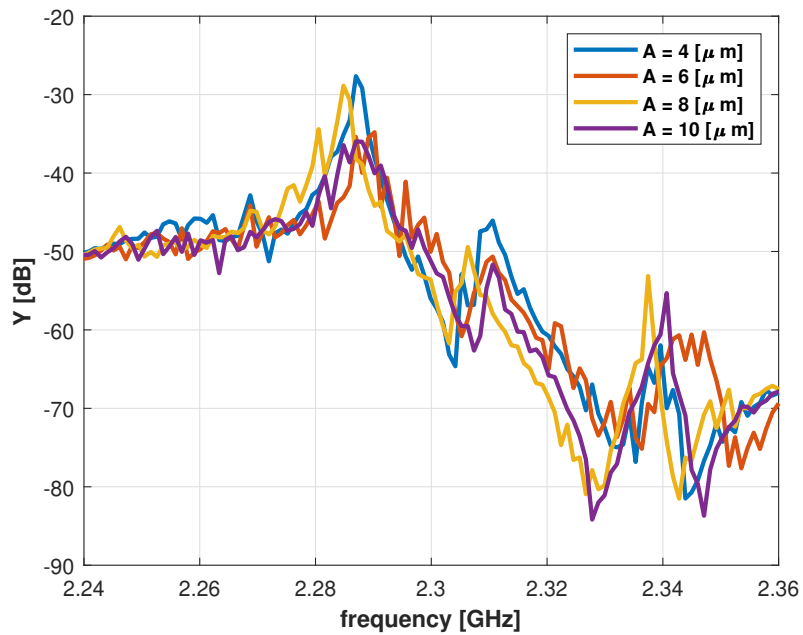


**Figure 3.29:** sinusoidal apodization study on a non optimized 2DMR configuration. The curves are relative to four different sine aperture values.

$A$ [ $\mu m$ ]	4	6	8	10
$k_t^2$ [%]	6.25	6.49	6.35	6.48
$Q/Q_{max}$	0.6	0.4	0.5	0.3
$C_0$ [fF]	95	88	85	80
$C_m$ [fF]	4.85	4.49	4.34	4.08

**Table 3.1:** results from the study on the aperture  $A$  of the sinusoidal apodization.

In the opposite way, when the IDT of CLMRs are shaped, the  $d_{31}$  excitation in the portion of the electrodes that extends beyond the neighboring fingers gives no results, hence decreasing the  $C_m$  together with  $C_0$  and greatly degrading the  $k_t^2$ . The big spurious modes affecting the resonances in fig.3.29 come from the support tethers and their effect is not reduced by the applied apodization. However, the multitude of ripples appearing between the main peaks are related to the electrode arrangement and disappear for higher apodization depths, showing a correlation between the finger lengths variation and ripples suppression. Unfortunately, the cost of spurious modes suppression is paid by the quality factor, that is reduced when AD is increased. Finally, it is worth mentioning that in the case under consideration the displacement is concentrated in the center of the resonator, as shown in fig.3.30.

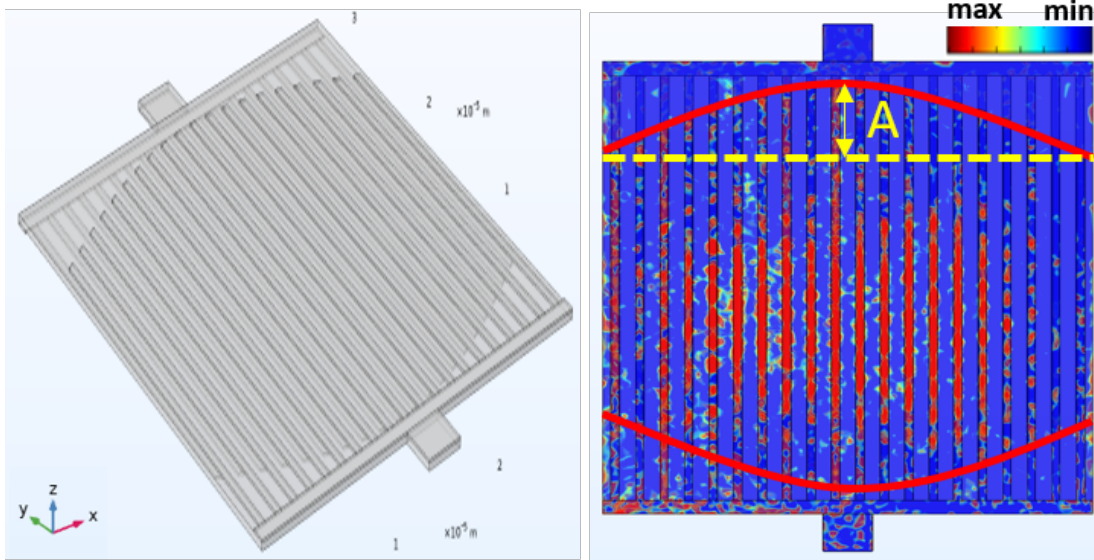


**Figure 3.30:** 2DMR with sinusoidal apodization applied to the fingers. "A" indicates the dimension that has been parametrically swept in simulations.

### Circular apodization

As an extreme case of the sinusoidal curvature, a circular shape has been simulated. Also in this case, the electromechanical coupling coefficient is unvaried and a reduction of the spurious modes is observed. A localized displacement similar to the one observed with irregular apodization is shown in fig.3.31.

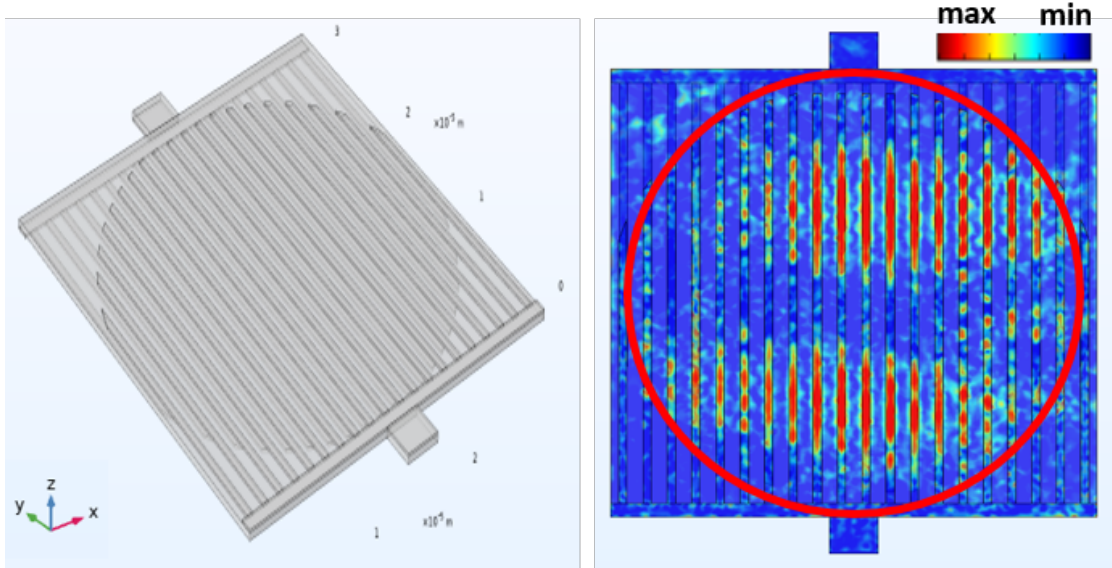


**Figure 3.31:** *2DMR with circular apodization applied to the fingers.*

### Comparison of different apodization shapes

The simulation results of a  $2DMR^M$  with center frequency at 4.9 GHz with different apodization shapes applied are compared in fig.3.32. The results refer to a configuration with optimized bus and anchors. As expected from previous results, the ripples in the admittance curve comprised between the resonance and anti-resonance frequencies get mitigated by the adoption of apodization, while preserving the  $k_t^2$ . The main parameters evaluated for all the simulated configurations are listed in table 3.2. The Q values have been evaluated by fitting the curves with the BVD model and very low variations are observed due to the similar apodization depth common to all the shapes. To properly characterize the impact of AD on the quality factor, experimental measurements are needed and different configurations have been included in the layouts for the experimental plans.

Finally, it should be remarked that these are good and smooth resonances for a 3D FEM simulation, very difficult to be obtained for CLMRs or CMRs without

drastically reducing the  $kt^2$ . This study truly demonstrates one more advantage of 2DMRs compared to other resonator typologies.

	$k_t^2$ [%]	Q	FoM
<b>NO APO</b>	6.3	2000	126
<b>POLY</b>	5.9	2000	118
<b>CIRCLE</b>	6.3	1800	113
<b>SINE</b>	6	2500	150

**Table 3.2:** comparison between different apodization shapes applied to the electrode fingers of a 2DMR.

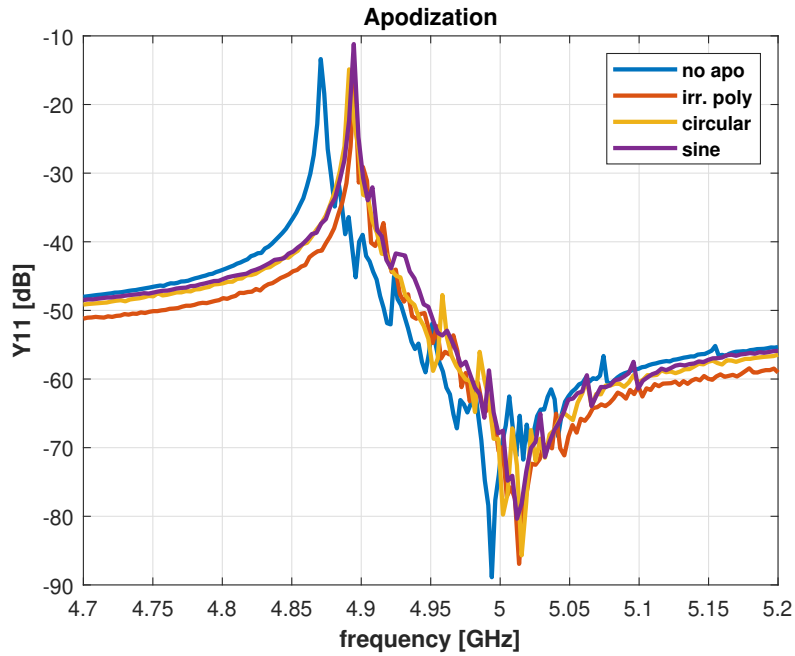


**Figure 3.32:** simulated admittances for different apodization shapes adopted. The resonance and anti-resonance frequencies are shifted by the same amount, thus maintaining the  $k_t^2$  constant.

# Chapter 4

## An innovative two-ports device

### 4.1 Principle of operation and modeling

In RF engineering, it is sometime required to have circuits whose behaviour depends on the input electromagnetic power feeding the system. Let's think, for example, of a circuit able to change the response of a filtering stage when the input power of a signal with a certain frequency  $f_c$  goes above a threshold. A common implementation would take advantage of a power detector put in parallel to a MEMS resonator that filters the signal at its resonance frequency. However, the connection between the sensor and the filter represents an electrical load for the MEMS resonator, thus degrading the  $kt^2$  and quality factor. In order to sense the power of an input signal preventing the degradation of the resonant system performances, a new device topology has been engineered based on 2DMR resonators.

The devices that have been described so far are characterized by one port only, where the bottom electrode is grounded and the top terminal gives an input where the admittance response is probed. With the aim of acoustically connecting two resonators preserving the independent operation of each component, a two ports device comprising two 2DMRs fabricated on the same Aluminum Nitride substrate has been simulated. The 3D geometry is shown in fig.4.1, where two terminals with  $N1$  and  $N2$  electrode fingers share the same ground (i.e. the bottom electrodes) and are physically separated by an *inactive gap/area* (IA) that is left uncovered by the metal. The first terminal is powered by an input signal while the second is sensed through a dedicated anchor and the two resonators are electrically decoupled when the electrical signal is out of resonance with respect to the 2DMRs main acoustic mode. Indeed, when the signal feeding the input terminal excites the resonator

at its resonance frequency, the S1 extensional mode spreads in an evanescent way along the inactive gap, resulting in a low power transmission to the output terminal. The main feature of this device derives from the peculiarity of the S1 mode of having a cut-off frequency below which it cannot be excited and propagate. By construction, the S1 mode is directly stimulated in the active areas only whereas it does not propagate through the spacing between the fingers and in the inactive gap separating the two resonators. In fact, in these areas the mode is evanescent and it is formally described by an imaginary wave-number  $k_{ix}$ ; the overall displacement is therefore well confined within the electrodes. The main goal of such architecture is to enable the sensing of the output terminal without affecting the resonance performances (i.e. the input admittance *vs* frequency) of the resonator at the input. It should be mentioned that this is the first time an application based on this principle of operation is presented and very few works on evanescent acoustic couplings have been presented in the past [35],[36].

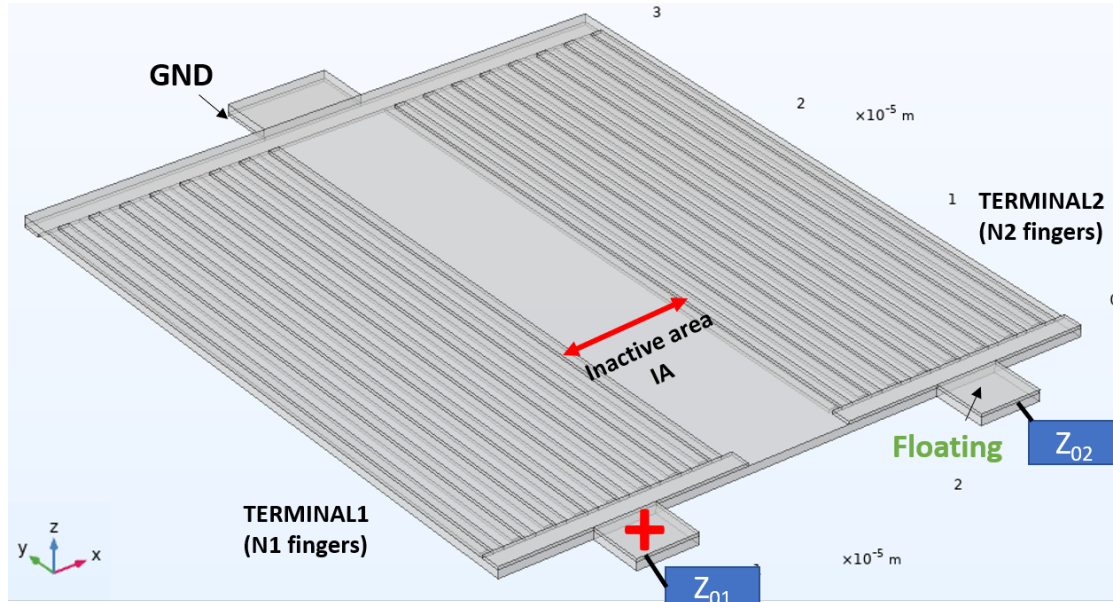


**Figure 4.1:** 3D model of the two-ports device based on acoustically coupled 2DMRs. Terminal 1 is powered by an input signal whereas terminal 2 is left at a floating potential. Both terminals are terminated on user-defined impedances for simulations.

## 4.2 Acoustic and electrical analyses

Fig.4.2 shows a 2-dimensional model used to characterize the behaviour of the two-ports device where  $N1$  is much larger than  $N2$ . The width of the electrodes

together with the spacing between them have been chosen so to excite the S1 mode alone, preventing the S0 to give a significant contribution in the displacement wave. The  $K^2$  plot of fig.4.3 gives an approximated idea of what  $k_x$  should be excited in an infinite plate 1  $[\mu m]$  thick so to gain a maximum disparity between the S1 and S0 excitation. The graph shows that an almost pure S1 induced displacement should be observed for  $k_x \approx 1.5 [\mu m^{-1}]$  which corresponds to a wavelength  $\lambda_x \approx 4 [\mu m]$ . According to this result, the electrode width has been set to  $E.W. = 1.75 [\mu m]$  with a fixed thickness  $t_E = 200 [nm]$  and the relative spacing has been chosen to not making the S1 mode couple with S0 (i.e. the  $kt^2$  of the 2DMR is not maximized in this case). If the optimized combination of S1 and S0 would be adopted for the resonator design, a displacement along the width of the device would be excited due to the horizontal dilatations and compressions induced by the zero order Lamb mode. In this case, a significant power transmission from terminal 1 to terminal 2 would be observed and each port would heavily affect the electrical behavior of the other one, which is not what it is expected from this device.

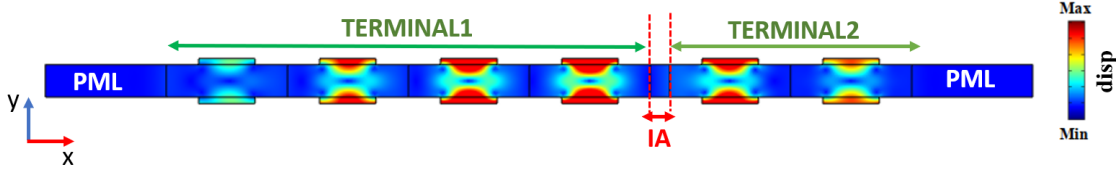


**Figure 4.2:** 2D model of the two-ports device based on 2DMRs technology. In this example,  $N1 > N2$ .

The width of the inactive area plays an active role in determining the amount of acoustic energy transmitted through the terminals. If the IA width is multiple of half wavelength of the S0 mode that would propagate in an infinitely wide uncovered area, the displacement induced along the  $x$  direction couples in phase with the one induced by the extensional S1 mode in the active areas. The result in this case is an enhancement of the power transmitted from terminal 1 to terminal 2. This means that, in order to minimize the power transmission (i.e. the  $S_{21}$  parameter) from the input port to the output, the inactive gap separating the two ports should not match integer multiples of the S0 mode's half-wavelength. Fig.4.4 shows the displacements along both the  $y$  and  $x$  directions for different IA widths in a portion of the device comprising the last cell of terminal 1, the inactive gap and the first cell of terminal 2. It is evident that for  $IA = 1.6[\mu m]$  the displacement induced in the  $x$  direction is enhanced; this is because the S0 in this region has an estimated wavelength of  $\lambda_{x,S0} \approx 2 \cdot 1.7[\mu m]$ . Increasing the IA width to 2  $[\mu m]$  and 2.6  $[\mu m]$  results in a displacements reduction, hence a better acoustic isolation between the two ports is obtained.

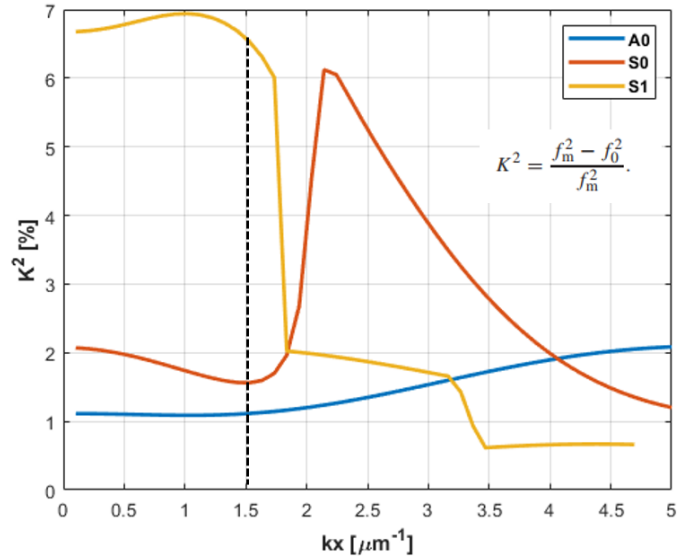


**Figure 4.3:**  $K^2$  plot computed from the dispersive relations of the three fundamental modes extracted by COMSOL®.

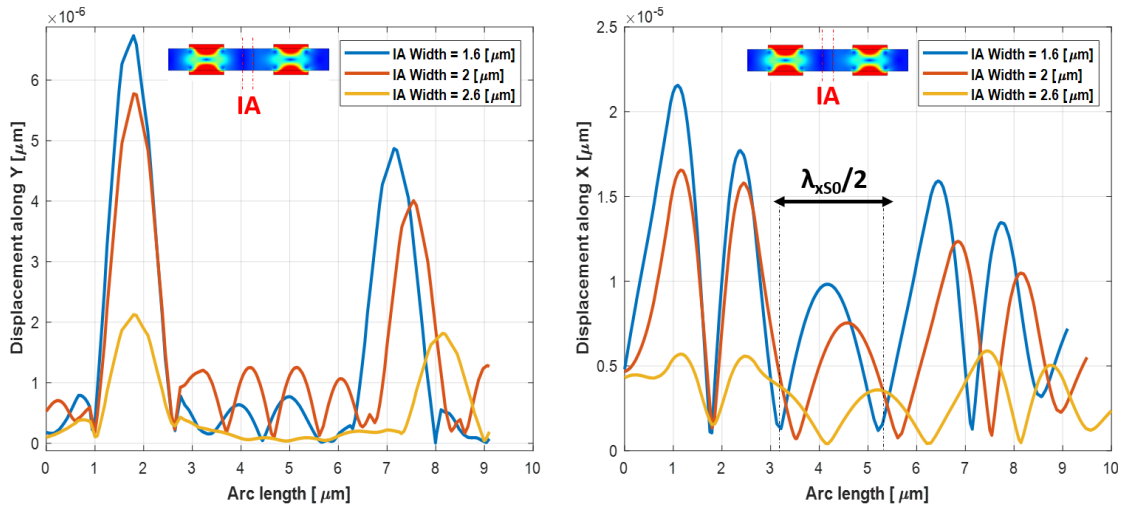


**Figure 4.4:** displacement along  $Y$  and  $X$  directions at the 2DMR resonant frequency for an arc length including two active cells. The insets show the portion of the resonators included in the arc.

To characterize the power transmission between the two terminals with respect to inactive area variations, the  $S$  parameters have been analyzed. The scattering parameters describe the relationships between electrical ports in term of power transmission and voltage gains. They describe reflection and transmission of voltages from both sides of a network. When fully evaluated, the S matrix characterizing the network can be used to represent it as a simple black box to be included in a bigger electrical schematic. Since it is generally faster for a 3D COMSOL<sup>®</sup> simulation to extract a Y matrix rather than the S elements, conversion formulas have been used for matrices conversion. Moreover, FEM simulations seemed to be extremely imprecise in determining the scattering parameters in presence of complex source and load impedances as termination of the electrical network. Therefore, conversion formulas valid both for real and complex loads have been used according to the derivation presented in [37]:

$$S_{11} = \frac{(1 - Y_{11}Z_{01}^*)(1 + Y_{22}Z_{02}) + Y_{12}Y_{21}Z_{01}^*Z_{02}}{(1 + Y_{11}Z_{01})(1 + Y_{22}Z_{02}) - Y_{12}Y_{21}Z_{01}Z_{02}} \quad (4.1a)$$

$$S_{21} = \frac{-2Y_{21}\sqrt{R_{01}R_{02}}}{(1 + Y_{11}Z_{01})(1 + Y_{22}Z_{02}) - Y_{12}Y_{21}Z_{01}Z_{02}} \quad (4.1b)$$

$$S_{12} = \frac{-2Y_{12}\sqrt{R_{01}R_{02}}}{(1 + Y_{11}Z_{01})(1 + Y_{22}Z_{02}) - Y_{12}Y_{21}Z_{01}Z_{02}} \quad (4.1c)$$

$$S_{22} = \frac{(1 + Y_{11}Z_{01})(1 - Y_{22}Z_{02}^*) + Y_{12}Y_{21}Z_{01}Z_{02}^*}{(1 + Y_{11}Z_{01})(1 + Y_{22}Z_{02}) - Y_{12}Y_{21}Z_{01}Z_{02}} \quad (4.1d)$$

where  $Z_{01}$ ,  $Z_{02}$ ,  $R_{01}$  and  $R_{02}$  are, respectively, the complex impedances at port 1 and port 2 and their real parts. The admittance matrix can be computed from the S parameters by complementary formulas:

$$Y_{11} = \frac{(1 - S_{11})(Z_{02}^* + S_{22}Z_{02}) + S_{12}S_{21}Z_{02}}{(Z_{01}^* + S_{11}Z_{01})(Z_{02}^* + S_{22}Z_{02}) - S_{12}S_{21}Z_{01}Z_{02}} \quad (4.2a)$$

$$Y_{21} = \frac{-2S_{21}(R_{01}R_{02})^{1/2}}{(Z_{01}^* + S_{11}Z_{01})(Z_{02}^* + S_{22}Z_{02}) - S_{12}S_{21}Z_{01}Z_{02}} \quad (4.2b)$$

$$Y_{12} = \frac{-2S_{12}(R_{01}R_{02})^{1/2}}{(Z_{01}^* + S_{11}Z_{01})(Z_{02}^* + S_{22}Z_{02}) - S_{12}S_{21}Z_{01}Z_{02}} \quad (4.2c)$$

$$Y_{22} = \frac{(Z_{01}^* + S_{11}Z_{01})(1 - S_{22}) + S_{12}S_{21}Z_{01}}{(Z_{01}^* + S_{11}Z_{01})(Z_{02}^* + S_{22}Z_{02}) - S_{12}S_{21}Z_{01}Z_{02}} \quad (4.2d)$$

The S parameters extracted from FEM simulations versus frequency are shown in fig.4.5. The  $S_{21}$  magnitude presents a well defined peak at the 2DMR resonance

frequency, as expected. A closer look at the dependence of the  $S_{21}$  peak with respect to the width of the inactive area is given in fig.4.6 for narrow and wide gaps. When the inactive area is much smaller than  $\lambda_{x,S0}$  (fig.4.6a), the decrease is almost exponential, coherently with the evanescent displacement induced by the S1 mode. On the other hand, when the width of the inactive gap reaches integer multiples of  $\lambda_{x,S0}/2$ , the power transmission is amplified and a precise periodicity is predicted by simulations (fig.4.6b).

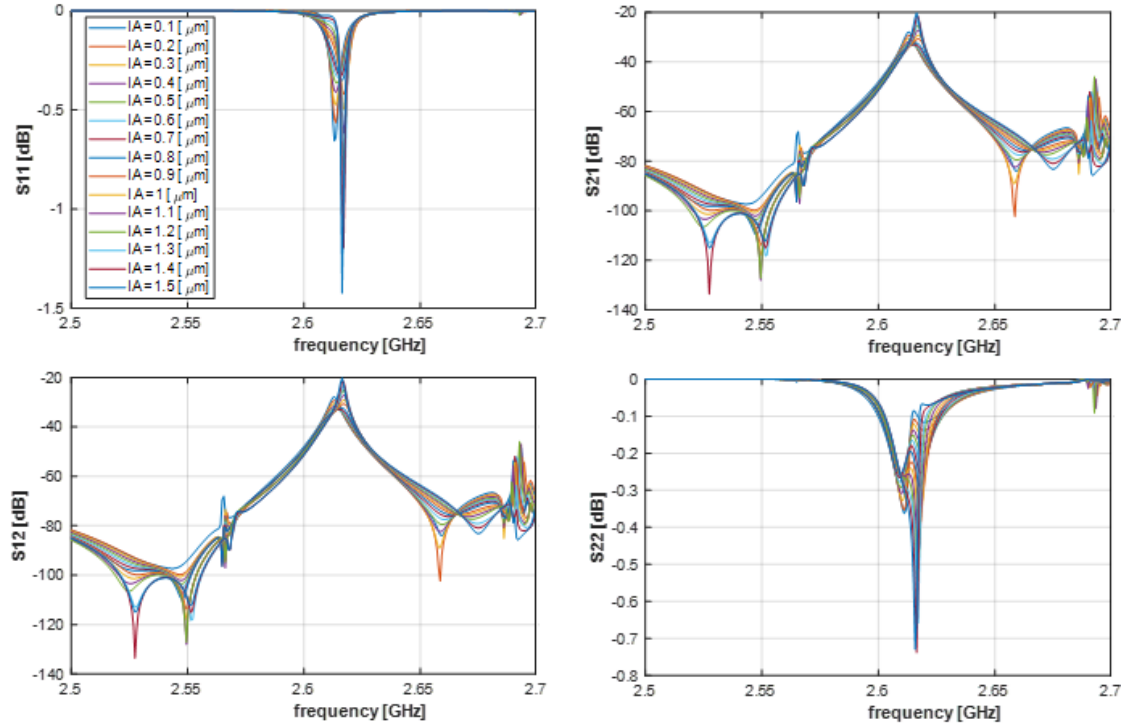


**Figure 4.5:** scattering parameters evaluated from COMSOL<sup>®</sup> 2D simulations with a real impedance termination ( $R = 50 [\Omega]$ ). The  $S_{21}$  parameter shows a peak at the 2DMR's resonance frequency that is inversely proportional to the inactive area width.

One of the most important features in a power detector based on MEMS resonator is the frequency selectivity in the electrical response. The RF signal that powers the input port (terminal 1 in figs.4.1, 4.2) sees the input impedance of the first 2DMR, which is frequency dependent. Thanks to the electrical and acoustic isolation between the input and output terminals, the electromechanical performances of the input resonator does not distinguish from that of a one-port 2DMR. This property permits to choose the number of active cells of the first resonator that

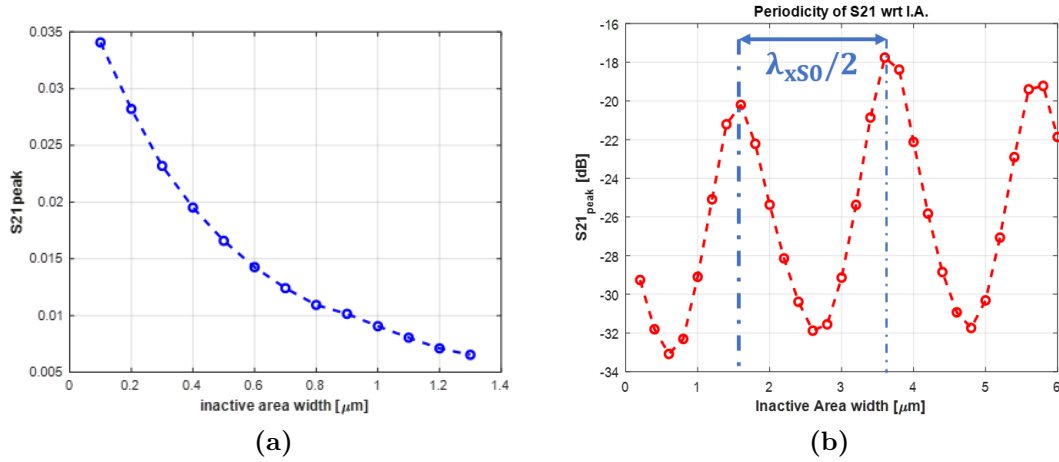


**Figure 4.6:**  $S_{21}$  peak value dependence on the inactive area width shown for narrow (a) and wide (b) gaps.

optimizes the acoustic performance regardless of the design chosen for the second 2DMR. Because of this, the number of fingers for the input 2DMR ( $N1$ ) is chosen to be higher than the number of electrodes of the output 2DMR ( $N2$ , see fig.4.2) so that an optimized resonance can be observed in the input admittance while keeping a minimum number of fingers. Indeed, the electrodes grating of the second terminal does not actively excite any resonance because it is left floating with the only purpose of collecting charges induced by the acoustic coupling at resonance within the piezoelectric substrate. Therefore,  $N2$  should be set to a minimum value that preserves the 2DMR mode at the output port with the selected wavelength.

The architecture can be thought as a two-port network as the one in fig.4.7:

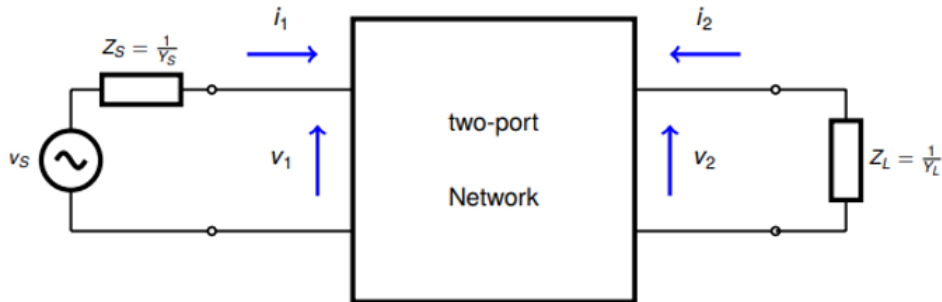


**Figure 4.7:** schematic of a two-port electrical network with load and source terminations.

where the currents are defined as

$$i_1 = Y_{11}v_1 + Y_{12}v_2 \quad (4.3a)$$

$$i_2 = Y_{21}v_1 + Y_{22}v_2 \quad (4.3b)$$

Substituting  $i_2 = -Y_L v_2$  into eq.4.3, the internal voltage gain is evaluated

$$\frac{v_2}{v_1} = \frac{-Y_{21}}{Y_L + Y_{22}} \quad (4.4)$$

and the input admittance is obtained from the expression of  $i_1$ :

$$Y_{in} = \frac{i_1}{v_1} = Y_{11} - \frac{Y_{12}Y_{21}}{Y_L + Y_{22}} \quad (4.5)$$

The input admittance obtained from 2D FEM simulations for different values of inactive area widths is given in fig.4.8. In these simulations, the IA values are smaller than half wavelength of the S0 mode. The admittance vs frequency plots remind the ones of a one-port 2DM resonator.

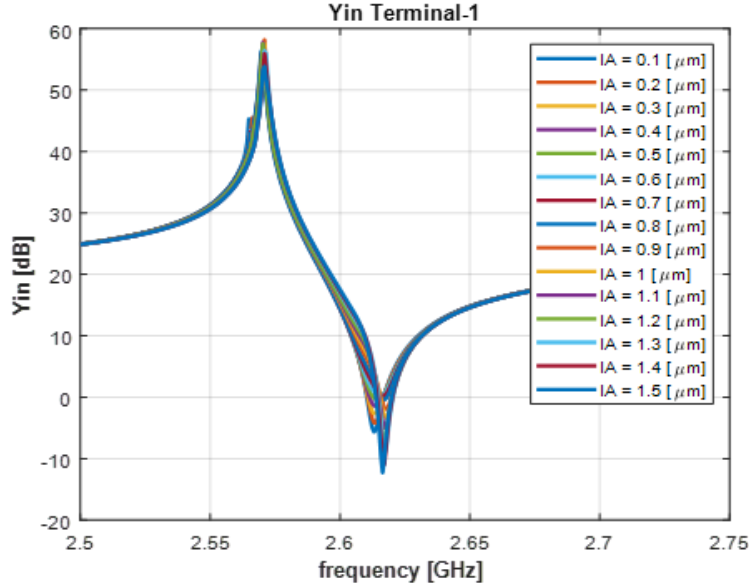


**Figure 4.8:** *input admittance seen from terminal 1 of the two-ports device obtained through 2D FEM simulations.*

From the analysis of the input admittance plots, the  $kt^2$  and quality factors at both the resonance and antiresonance frequency have been evaluated sweeping the

inactive area width in a wide range; the results are graphically presented in fig.4.9 and fig.4.10. All the parameters show a periodicity with respect to multiples of the half wavelength of the  $S0$  mode. It is interesting to note that the  $k_t^2$  shows its maximum values for inactive area widths that minimize the  $S_{21}$  and a similar behaviour is shown by the quality factor at resonance. This is due to the common dependence of both parameters on the mechanical energy stored in the resonator as described in detail in chapter 1. The more mechanical energy is lost by leakage, the smaller the quality factor is and the less energy is involved in the electromechanical transduction in the active areas. From the point of view of the input terminal, when the system is designed to enhance the acoustic coupling between the two ports through  $S0$ , a significant amount of acoustic energy is lost degrading the 2DMR performance. Instead, when the coupling is minimized by properly designing the inactive gap, very low leakage is observed due to the evanescent behaviour of the  $S1$  mode in this area and, in this case, the  $k_t^2$  and  $Q_{fs}$  are maximized.

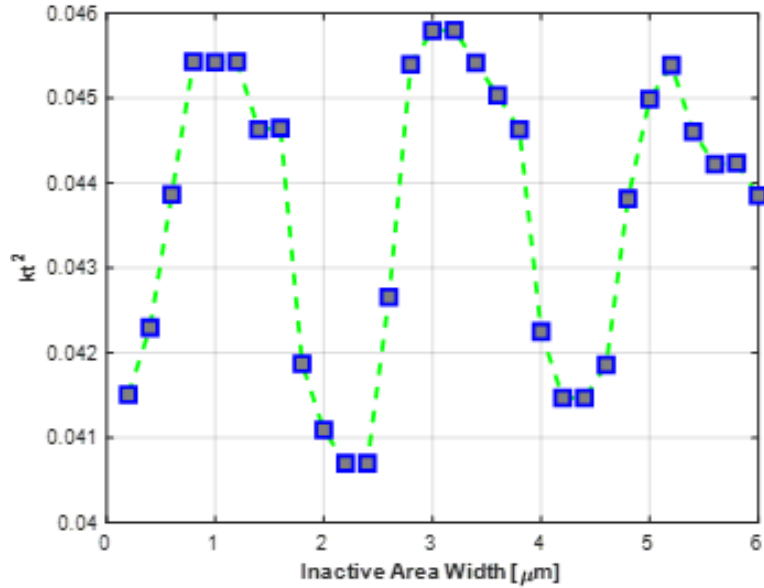
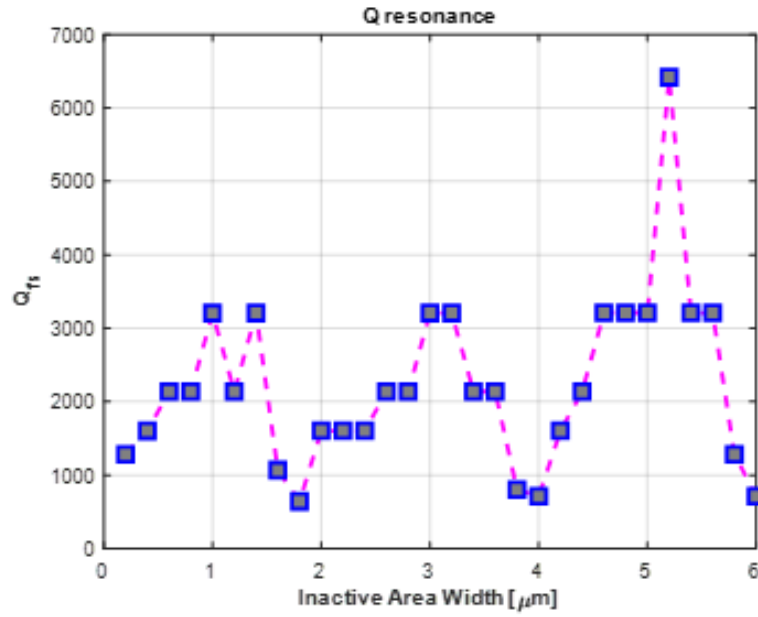
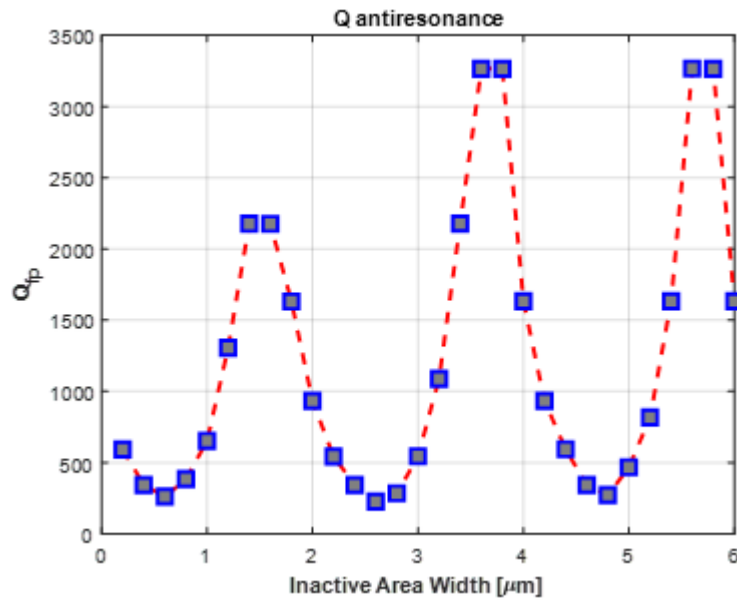


**Figure 4.9:** dependence of the electromechanical coupling coefficient on the width of the inactive area separating the two resonators. The periodicity is given by half-wavelength of the  $S0$  mode.



(a)



(b)

**Figure 4.10:** *dependence of the quality factor at resonance (a) and quality factor at antiresonance (b) on the width of the inactive area separating the two resonators. Both parameters show a periodicity given by half wavelength of the  $S_0$  mode.*

# Chapter 5

## Layouts design

### 5.1 Process flow and masks design

In order to experimentally demonstrate the results predicted through simulations, three sets of masks have been drawn for three layouts based on Aluminum Nitride and Scandium doped AlN thin films. The first (and most complete) layout includes 389 one port 2DMRs and 59 two ports devices with different configurations to cover the simulated parametric sweeps, all exhibiting a resonance frequency close to 2 [GHz]. The AlN film has a thickness of 1 [ $\mu m$ ] and Platinum has been chosen for bottom and top electrodes. The Platinum thickness has been set to 150 [nm] as a trade off between a small electrode resistance and a good acoustic confinement in the piezoelectric film. The entire process flow (excluding the masks fabrication and some high-definition lithography steps) has been run at Northeastern University cleanroom facility by expert PhD students due to entry limitations imposed by the emergency situation. The second batch of fabrication, instead, has been run at Harvard University by expert technicians and includes the study on apodization and two dimensional mode multimode resonators together with some two-ports devices. A thin piezoelectric film of 400 [nm] has been sputtered in this case, giving a resonance frequency around 5 [GHz], the highest ever measured for such a kind of resonators.

Given the high number of devices, the layouts have been drawn in a systematic way through the implementation of *ad-hoc* Python libraries defining all the functions for drawing the structures. The codes take advantage of the *gdspy* module for the creation of GDSII files by defining geometries and features on dedicated layers. The resulting files have then been merged using KLayout<sup>®</sup>, a widespread software for layouts drawings. Finally, all parameters concerning typical pads separation, dimensions of the testing structures, distance between the devices and layers numbering have been defined in a dedicated file updated for each project depending

on the tools used for fabrication.

The process flow adopted for the 2DMRs fabrication is schematically shown in fig.5.1. It comprises seven steps and five masks are needed for lithography. The Aluminum Nitride thin film has been deposited through sputtering by the Evatec CLUSTERLINE<sup>®</sup>, a recently installed tool that ranks Northeastern among the top universities for RF research in terms of fabrication capability. The same substrate has been wet etched using phosphoric acid to open the vias and all the metal layers have been patterned with lift-off. Finally, the resonators have been released from the Silicon substrate with a highly selective isotropic etch based on Xenon difluoride ( $XeF_2$ ).

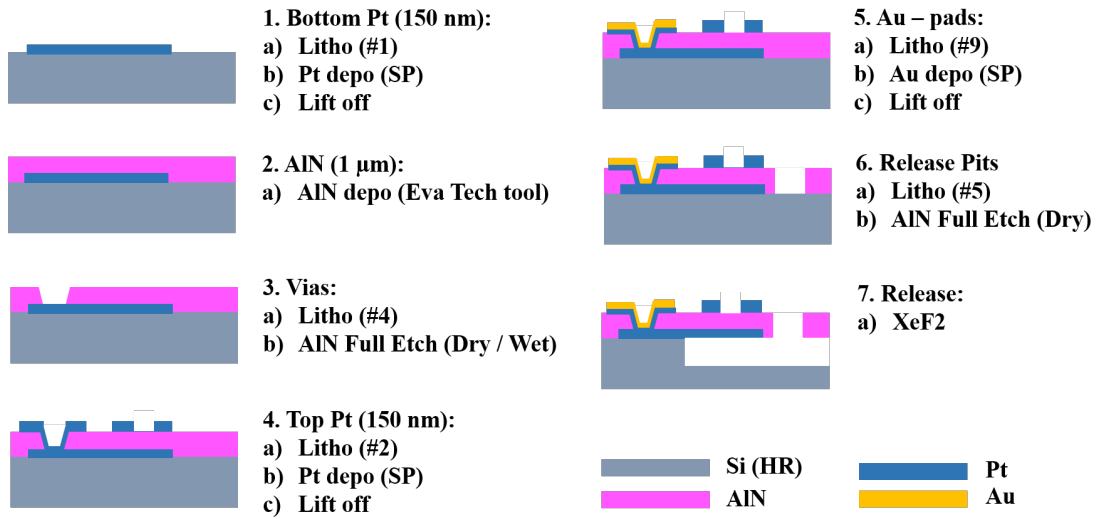


**Figure 5.1:** *process flow for the 2DMRs fabrication.*

Five layers are needed for the lithography steps in the process flow, they have been organized in this way:

- *layer 1:* bottom electrodes
- *layer 2:* top electrodes
- *layer 3:* gold pads
- *layer 4:* etching windows
- *layer 5:* vias

In the following, a few structures from the first layout comprising all the studies are taken as a reference for all the others to describe the features introduced in each mask. Fig.5.2 includes two examples of 2DMRs extracted from the *gds* file.

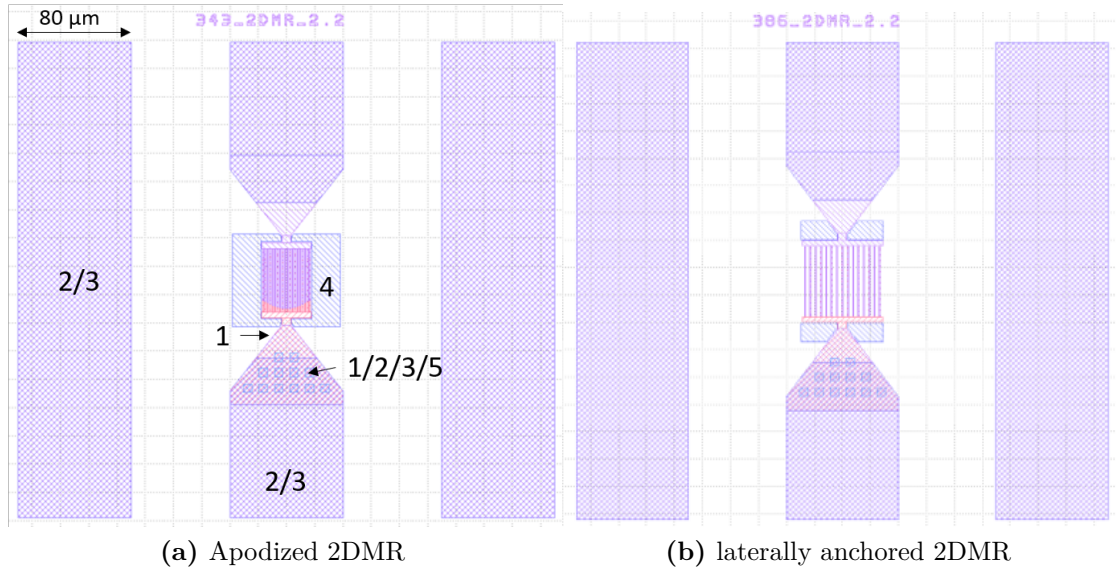


**Figure 5.2:** layout examples of 2DMRs. Numbers refer to the layers listed in the text.

Both figures show a ground-signal-ground (GSG) sequence for the probing pads; however, one ground has been shared by two subsequent resonators in the complete layout so to save precious space enabling both GSG and GS measurements at the same time. As depicted in the process flow, a thin gold layer has been deposited on the Pt pads so to reduce the parasitic resistances and thus the electrical loading of the resonators. For what concerns the vias, a minimum spacing of 4 [ $\mu m$ ] has been ensured between them and the edge of the metallic triangular routing, this is done to prevent irregularities in the metal layer due to the wet etch process. The resonators are surrounded by a release window for Silicon etching, their area has been carefully enlarged to ensure complete release of structure with different aspect ratios. In the example of fig.5.2b, the window is limited to the portion surrounding the anchors to maintain the lateral sides anchored to the substrate.

Exactly the same layers have been set for the two ports devices layout. Two examples are given in figs.5.3 and 5.4, where a suspended and a fully anchored configuration are respectively shown. The distance between ground and signal pads has been set to match the one of the probes (i.e., 150 [ $\mu m$ ]) and, in order to maintain the same orientation of 2DMRs on the masks, the structures have been rotated by 90°.

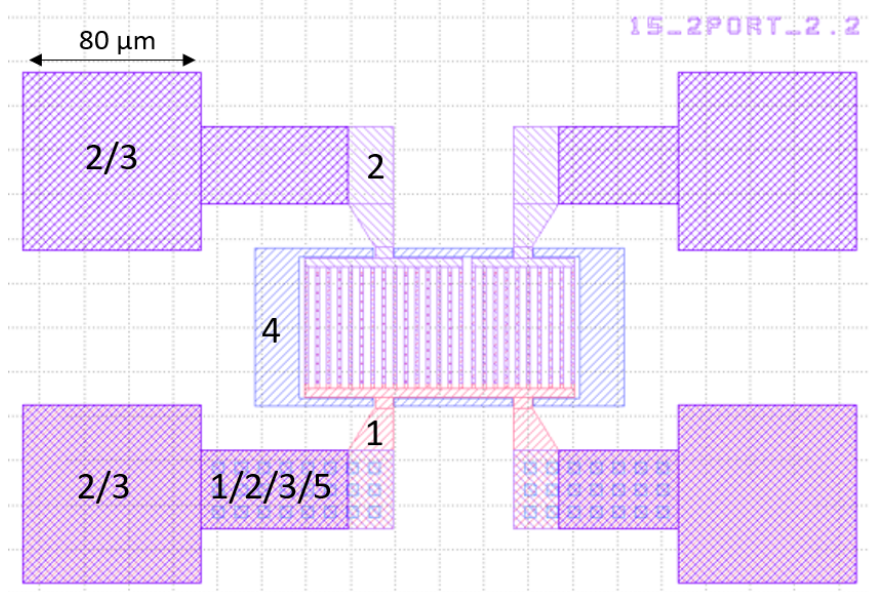


**Figure 5.3:** layout of a 2-ports device comprising two 2DMRs with different number of fingers. Numbers refer to the layers listed in the text.

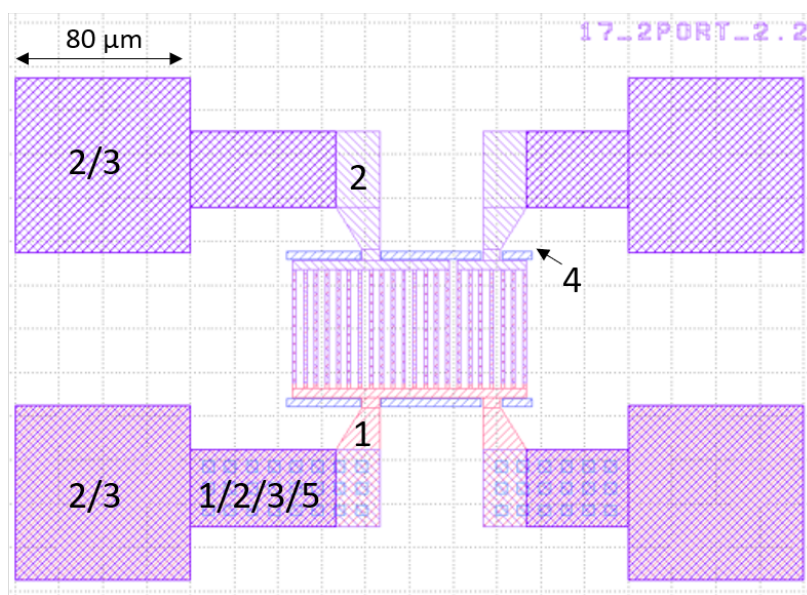


**Figure 5.4:** layout of a laterally anchored 2-ports device. Numbers refer to the layers listed in the text.

The entire chip comprising all the layers is shown in fig.5.5. It includes several test structures for each layer as serpentine for resistivity test, cantilevers for film stress tests and resolution structures. The total area of the chip is  $15 \times 15 \text{ mm}$  and several replicas have been fabricated on the same 4 inch wafer using a stepper with a minimum feature size of  $700 \text{ [nm]}$ .

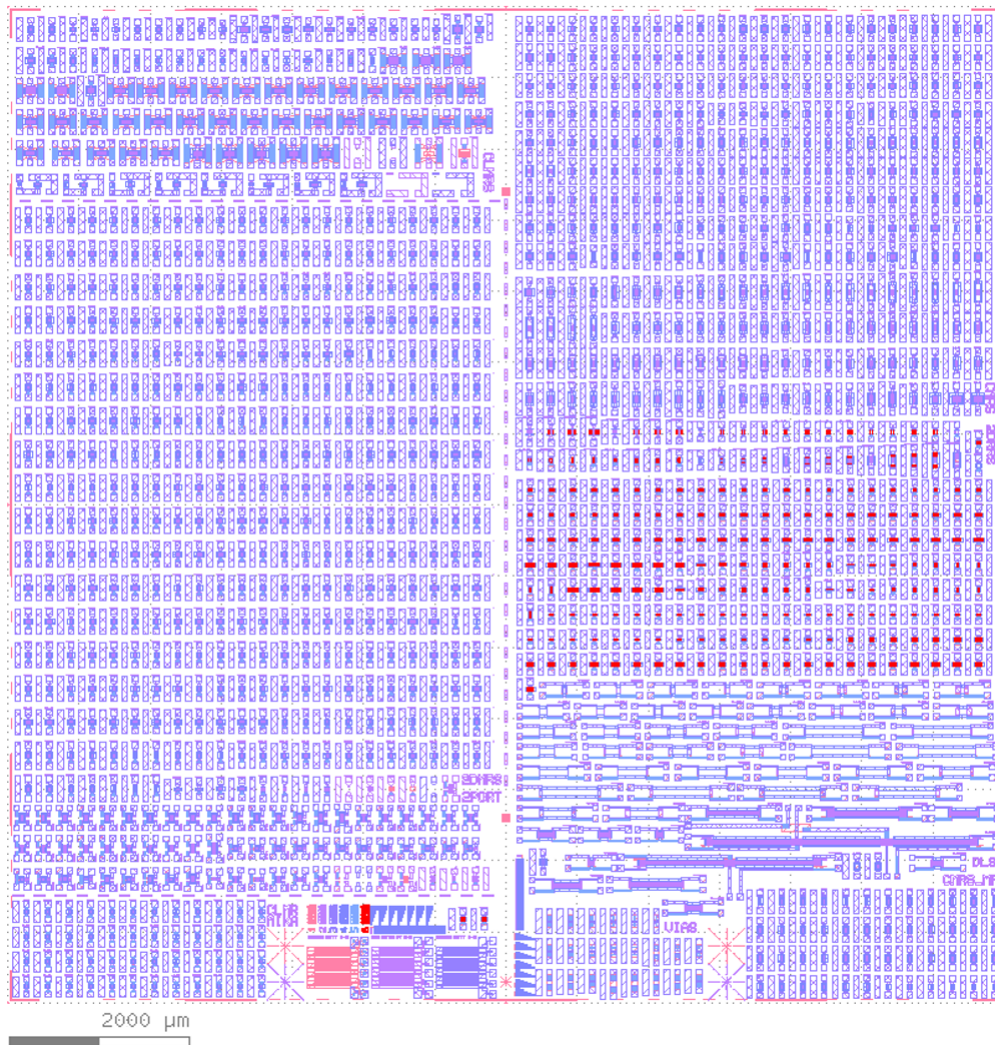


**Figure 5.5:** complete layout of the chip comprising all the resonators and testing structures for each layer.

## 5.2 Additional layouts

In addition to the main experimental plan that adopts the same layers and materials specifications adopted in the FEM simulations, two other layouts have been drawn to study the optimization results at different frequencies and implementing other materials. The first additional layout includes  $2DMR^M$  and 2-ports devices with resonance frequency centered at 5 [GHz] (the highest frequency ever adopted for 2DMRs). The process has to be run on 400 [nm] thick AlN layer with Molybdenum and Aluminum electrodes and the devices will be fabricated at the Lincoln Laboratory of MIT. The complete layout is shown in fig.5.7 and includes at its bottom some multi-ports delay lines based on the S1/S0 combination characterized for  $2DMR^M$ . These delay lines are based on a wide array of electrode pairs equally spaced so to excite the  $2DMR^M$  mode and several ports are attached to the line along its length. This permits to simultaneously read a signal at different terminals with specific delays from the input port.

A slightly different process flow from the one previously presented is implemented in this case and it is shown below. In order to better confine the released area, a poly-Silicon layer is deposited and patterned in a  $SiO_2$  substrate. Therefore, an additional mask is needed to geometrically define these areas.

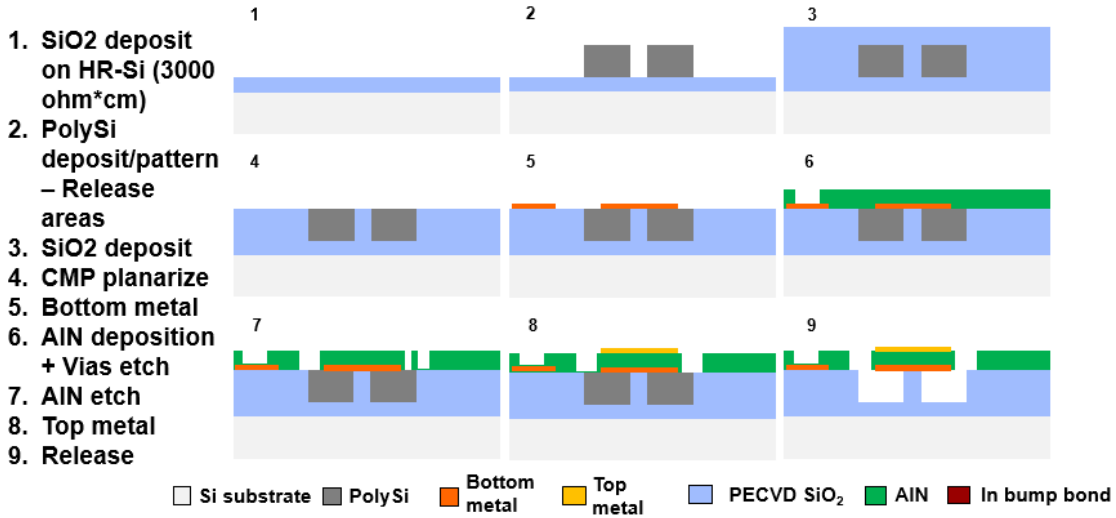
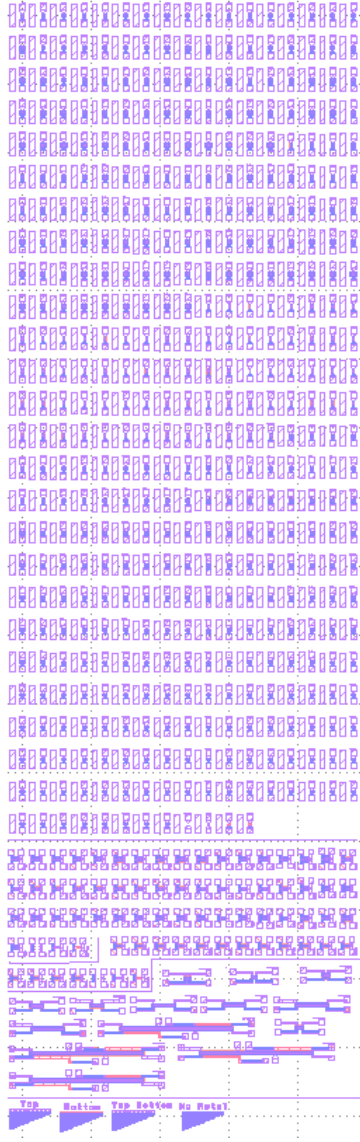


Figure 5.6: process flow adopted by the Lincoln Laboratory for the 5[GHz] layout.

Finally, a third layout including 2DMRs and  $2DMR_s^M$  with different lengths, widths and number of fingers has been drawn. It has to be run on a 2 [ $\mu m$ ] thick Scandium doped AlN film. The doping concentration is 30% and enables an astonishing boosting of the devices  $k_t^2$  thanks to the change induced in the stiffness and piezoelectric coefficients [2]. The layout including 2-ports devices

and 2DMRs is shown in fig.5.8. In order to predict the resonators performances with this innovative material, a 2D Comsol<sup>®</sup> model including the piezoelectric and stiffness coefficients published by Caro et al. in [2] has been built. However, since ScAlN technology is not the focus of this work, the simulation results have not been included in the discussion.



**Figure 5.7:** layout for the study of one and two ports AlN based 2DMRs with resonance frequency centered at 5 [GHz]. Multiports delay lines based on 2DMR<sup>M</sup> technology have been included.

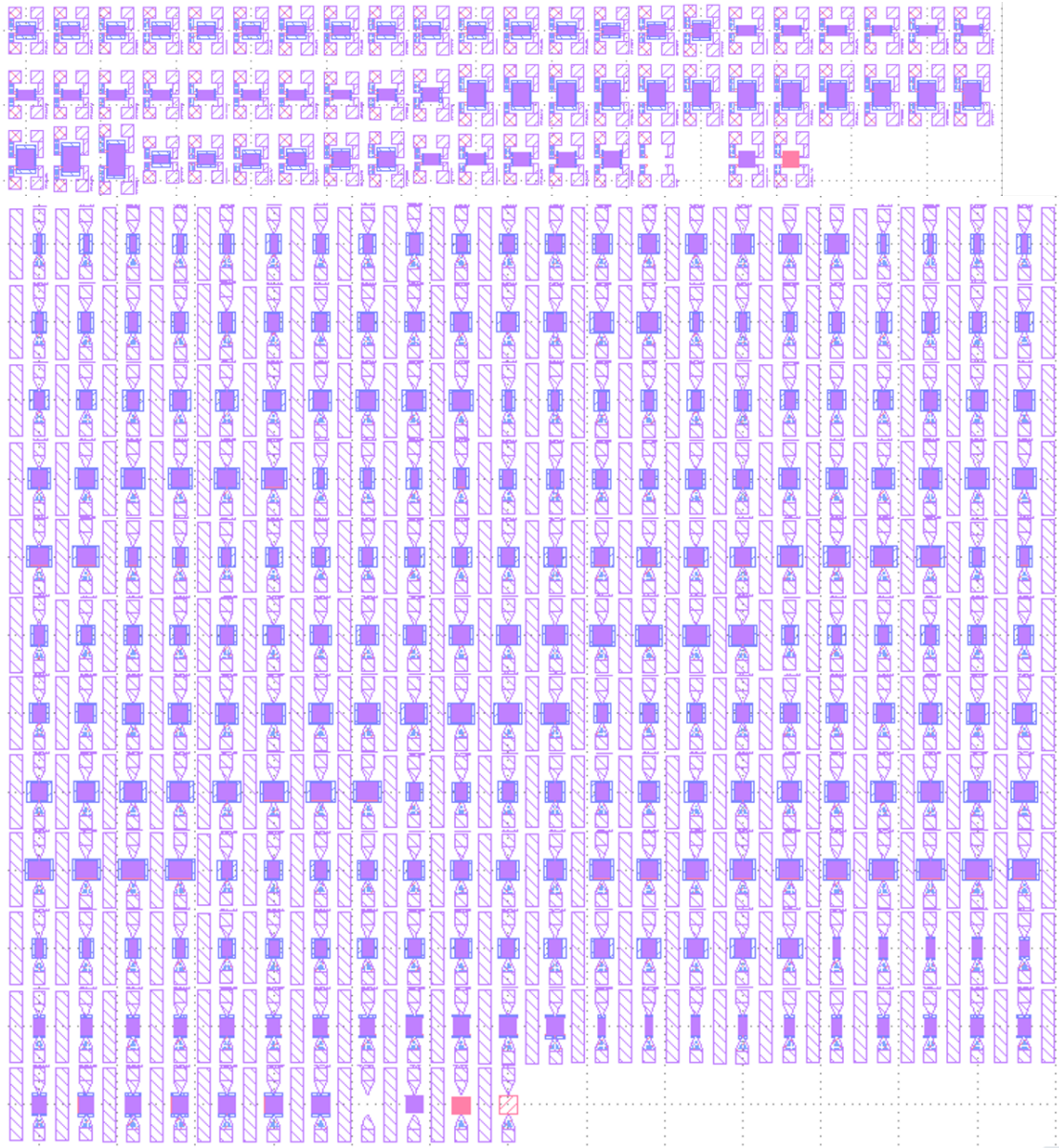


**Figure 5.8:** layout for the study of one and two ports AlScN based 2DMRs with resonance frequency centered at 900 [MHz].

# Chapter 6

## Conclusions

Detailed insights into the operation and performances of two-dimensional mode resonators for Radio Frequency applications have been discussed. With the aim of improving the quality factor at resonance  $Q$  and the electromechanical coupling coefficient  $k_t^2$  (and therefore the FoM) of 2DMRs without introducing additional steps in their fabrication process flow, four different studies have been presented. These have been conducted through COMSOL<sup>®</sup> Multiphysics FEM simulations and analytically described with mathematical models. Two- and three- dimensional models have been built and improved by the addition of non idealities and artificial domains to consider dissipative effects that impact the resonator performances. Particular attention has been given to the design of the mesh geometry and the boundary conditions imposed to the structures so to ensure the reliability of the studies by comparison with experimental data found in literature.

First of all, anchor losses have been analyzed by splitting the problem of acoustic leakage minimization into two subproblems, one focused on the design rules of the electrode bus and one focused on the anchors. Both the discussions have been based on the analogy between electromagnetic transmission lines and acoustic waveguides. The design rules for the bus electrodes have been derived by modeling the inactive portion of the resonators as a  $\lambda/4$  transformer for the acoustic waves excited in the active area; with this approach, nodal lines at the fingers edges are introduced so that the stress free boundaries at the resonator edges are converted into "*virtual fixed boundaries*" at the edge of the active areas. This change of boundary conditions has been shown to increase the energy stored under the electrodes, reducing the mechanical displacement in the buses and the amount of energy generated along the anchors direction. However, the introduction of nodal lines close to the active areas increases the effective device stiffness, therefore reducing the motional capacitance of the 2DMRs and decreasing the electromechanical coupling coefficient. Excellent matching between simulation results and theory has been demonstrated and commented.

The optimization of the anchors geometry has been investigate following two different approaches and boundary conditions. Based on the assumption of a huge acoustic impedance mismatch between the released area and the external substrate, fixed constraints (FC) have been firstly imposed at the edges of the released area and simulations with different anchor lengths have been run. Since COMSOL<sup>®</sup> does not precisely evaluate the quality factor in presence of FC, the latter has been evaluated through the integration of the acoustic Poynting vector over the anchors faces. Under the approximation of small released area, an analytical model demonstrating a  $\lambda/4$  periodicity of Q with respect to the anchor length with fixed released and inactive areas has been derived and compared with simulation results. The same study has been run with the implementation of Perfectly Matched Layers (PMLs) as artificial domains introduced to dissipate the acoustic energy irradiated from the anchor through the released area. In this case, however, an almost null reflection coefficient is set between the released area and PMLs and therefore, the transmission line model gets too complicated to be analytically handled. The Q results obtained with PMLs show clear trends versus the anchor width and length, being inversely proportional to  $W_a$  and proportional to  $L_a$ . In this case, a global optimum has been found for the configuration with Molybdenum electrodes for an anchor length of 5 [ $\mu m$ ]; with this value, the total length of the equivalent transmission line is  $\approx 11\lambda$ . Finally, a complete model including the Si substrate surrounding the resonator has been built and results have been fit to analytical predictions with an excellent agreement.

The second study focused on a complete analysis of the possible electrodes configurations for the 2DMRs excitation. The width of the electrodes and the relative spacing between them have been swept in a wide range monitoring the evolution of the  $k_t^2$  and resonance frequency  $f_s$  for different electrode thicknesses. Global maxima for the electromechanical coupling coefficient up to  $\approx 7\%$  both with Molybdenum and Platinum electrodes have been found when meeting specific design rules. This is a very important result as it shows that very high electromechanical coupling coefficients as the ones achieved by non-degenerate CLMRs can be achieved with 2DMR technology even without the introduction of additional components that could complicate the fabrication process. The high  $k_t^2$  are made possible by a reactive coupling between the first and the zero order symmetric Lamb modes that enables a higher motional capacitance. Because of this feature, these resonators have been named *Two-Dimensional Mode Multimodal Resonators* ( $2DMR^M$ ). Frequency tunability of 11% with  $k_t^2 > 5\%$  has been demonstrated through simulations, showing how  $2DMRs^M$  could be monolithically integrated on the same chip varying the acoustic wavelength lithographically.

The third study, instead, focused on the study of bottom-plate resonators where the electrical grating forming the bottom electrodes was substituted by a continuous

thin plate to further simplify the manufacturing process. Since it was experimentally demonstrated that good Aluminum Nitride crystallization is achieved when Platinum is used as the bottom substrate, a Pt thin plate has been assumed and the dependence of acoustic performances on its thickness studied. Different materials combinations including Molybdenum, Aluminum and Platinum have been simulated in two dimensions based on results found in literature. High  $k_t^2$  values up to 5% have been found also with this case with a frequency tunability comparable to the one of  $2DMRs^M$ . However, these devices seem to be affected by unwanted spurious modes and experimentally results are still under investigation to understand their effect.

To solve the spurious modes issue affecting the latter devices, a fourth study on electrodes apodization has been discussed. Different shapes have been drawn by complementary shaping the top and bottom electrode gratings, varying the electrode coverage up to 10% of the total surface of the device. Thanks to the mode excited by 2DMRs, no  $k_t^2$  variations have been observed when varying the fingers length. This is a very important result since it adds an interesting degree of freedom for the electrodes design that is not available in other resonator typologies as CLMRs and CMRs, where electrodes shaping drastically impacts the electromechanical performances.

In the last study presented in this thesis, a novel application based on the optimized one-port devices previously described has been introduced. It consists in a two-ports device with acoustically coupled 2DMRs through the evanescent acoustic displacement shown by the  $S1$  mode in the inactive areas. Thanks to the evanescent coupling, the input resonator is not electrically loaded by external components attached to the output 2DMR, making it possible to sense an input signal without degrading the optimized performances of the single-port resonator. This device could be implemented, for example, as a frequency selective power detector that enables a circuit reconfiguration when the input power goes above a certain threshold.

Finally, three experimental plans including 448, 309 and 494 devices and several test structures have been drawn. They included five/six masks each and have been drawn in a systematic way through Python coded libraries. The codes recall a set of *gds*py functions defining the geometries for drawing the blocks of the resonators and each layout has been drawn respecting the design rules listed in a separated file. Different components to be included on the same chip have been merged with KLayout<sup>®</sup>. The mask fabrication and the lithography steps are still running at Harvard University whereas the release process and test of the structure will be performed at Northeastern University. Due to limitations imposed by the COVID19 emergency, delays have accumulated and experimental results have not been made available in time to be included in this work.



# Appendix A

## Electrical loading considerations

The electrical loading of a MEMS resonator is an important specification that should be carefully taken into account when designing the structures. If the resistance of the electrical routings is much bigger than the motional resistance of the resonator itself, the admittance response gets hidden, making the resonator impossible to be tested and characterized. The resistive model that has been applied to study the best configurations satisfying the matching constraint is here presented. The idea is very simple, the single contributions of each part of the electrical routing have been considered and summed to get the final  $R_s$  estimation (i.e., the series resistance of the modified-BVD model). The following contributions refer to the dimensions labelled in fig.A.1;  $\rho$  is the electrical resistivity of the metal and  $t_m$  its thickness.

$$R_{pad} = \frac{\rho L_{pad}/2}{W_{pad}t_m} = \frac{\rho L_{pad}}{2W_{pad}t_m} \quad (\text{A.1})$$

$$R_{route} = \frac{\rho L_{route}}{\left(\frac{W_{pad}+W_a}{2}\right)t_m} = \frac{2\rho L_{route}}{(W_{pad} + W_a)t_m} \quad (\text{A.2})$$

$$R_{anchor} = \frac{\rho L_a}{W_a t_m} \quad (\text{A.3})$$

$$R_b = R_{bus}/2 \parallel R_{bus}/2 = R_{bus}/4 = \frac{\rho L_{bus}}{4W_b t_m} \quad (\text{A.4})$$

$$R_g = \frac{\rho g}{W_e t_m} \quad (\text{A.5})$$

$$R_{electrode} = \frac{4}{3} \frac{\rho L_e}{W_e t_m} \frac{1}{N_p} \quad (\text{A.6})$$

The series resistance  $R_s$  is evaluated by summing all the terms above for both the top and bottom electrodes together with the resistance of the vias connecting them ( $R_{vias} \approx 1 [\Omega]$ ):

$$R_1 = R_{pad} + R_{route} + R_{anchor} + R_{bus} + R_{fingers} \quad (\text{A.7})$$

$$R_2 = R_{pad} + R_{route} + R_{anchor} + R_{bus} + R_{vias} \quad (\text{A.8})$$

$$R_s = R_1 + R_2 \quad (\text{A.9})$$

Among all the contributions that come from the metals within the resonator area, the resistance of the bus is the most relevant, being the fingers resistances all in parallel. The length of the bus can be most of the times approximated by the width of the device and therefore it is directly proportional to the number of fingers ( $L_{bus} = N_p \cdot pitch$ ). This means that, when it comes to matching the resonator input impedance to a fixed real value (e.g., 50/500/1000  $[\Omega]$ ), a trade off between the number of finger pairs  $N_p$  and the length of the fingers should be considered to limit the resistance while maintaining fixed the static capacitance. The curves relative to a 1  $[k\Omega]$  matching impedance for a 2DMR respecting the layer specifications of the main experimental plan are shown in fig.A.2. The  $R_s$  vs  $L_{fingers}$  curve shows a minimum at 50  $[\mu m]$ , which corresponds to  $N_p \approx 15$ . The 1  $[k\Omega]$  matching gives a static capacitance higher than 60  $[fF]$  for a resonance frequency  $f_s \approx 2.2 [GHz]$  (fig.A.3), which is a preferred condition for the devices included in these experimental plans. The values of  $C_0$  have been computed given the targeted resonance frequency, and considering a measured loaded Q of  $\approx 1000$  (this value comes from previous experimental measurements of 2DMRs),

the motional resistance dependence on the matching impedance has been evaluated through eq.A.10. The  $R_m$  values are plotted in fig.A.3.

$$R_m = \frac{\pi^2}{8} \frac{1}{\omega C_0} \frac{1}{Q_{load} k_t^2} \quad (\text{A.10})$$

For  $R_{match} = 1000$  [ $\Omega$ ], the motional resistance is higher than 25 [ $\Omega$ ], which is almost double the  $R_s$  value shown at the minimum of the curve in fig.A.2. All these evaluations have been based on the experimental measured values of the Platinum resistivity listed in table A.1 and demonstrate that with a 1 [ $k\Omega$ ] impedance matching, the motional resistance is much higher than the resistance of the electrodes powering the device. Therefore, this is the configuration adopted for the 2DMR designed in this work and the estimated parameters are summarized in table A.2.

Material	Bulk Resistivity [ $\Omega m$ ]	Measured Resistivity [ $\Omega m$ ]
Pt	$1.06e - 7$	$1.80e - 7$

**Table A.1:** *experimental measurement of Pt thin film resistivity.*

Rmatch [ $\Omega$ ]	C0 [fF]	Rs [ $\Omega$ ]	Rm [ $\Omega$ ]
1000	73	17	26

**Table A.2:** *optimal configuration chosen for the 2DMR experimental plan considering the layers specifications. The 2DMR resonance frequency is  $f_s \approx 2.2$  [GHz]*

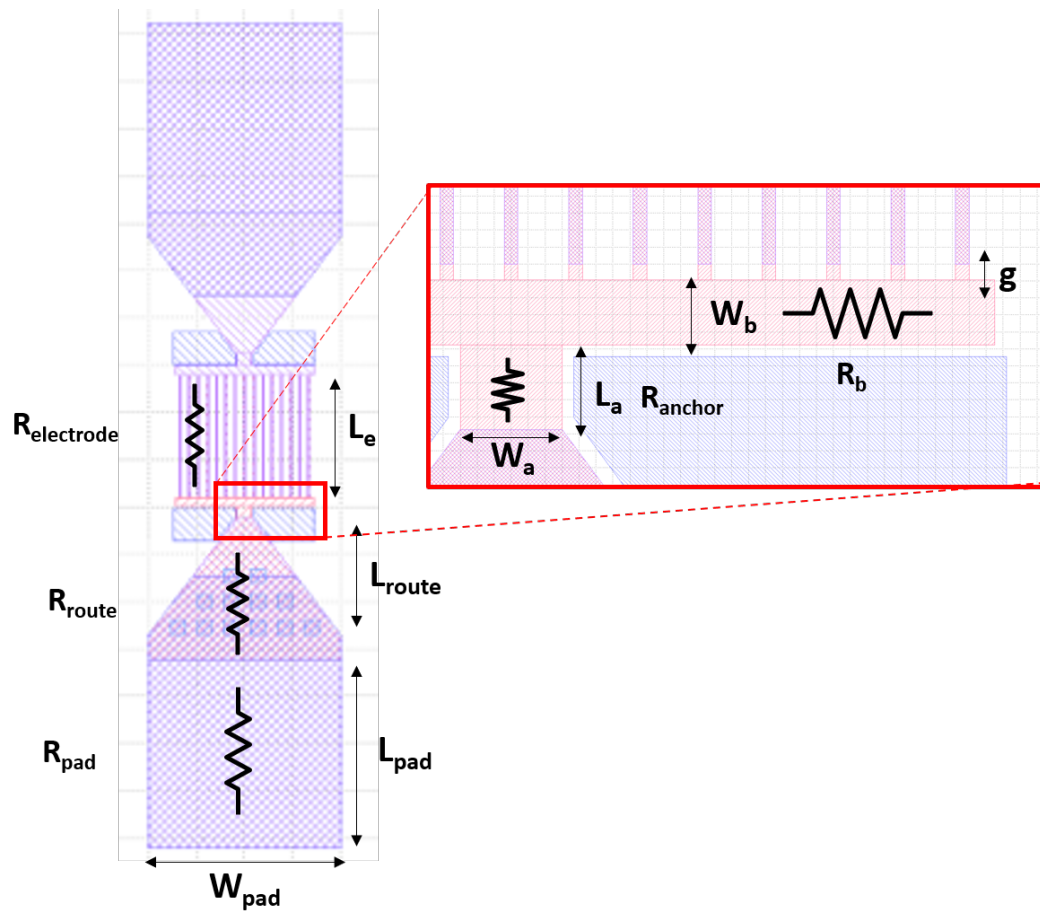
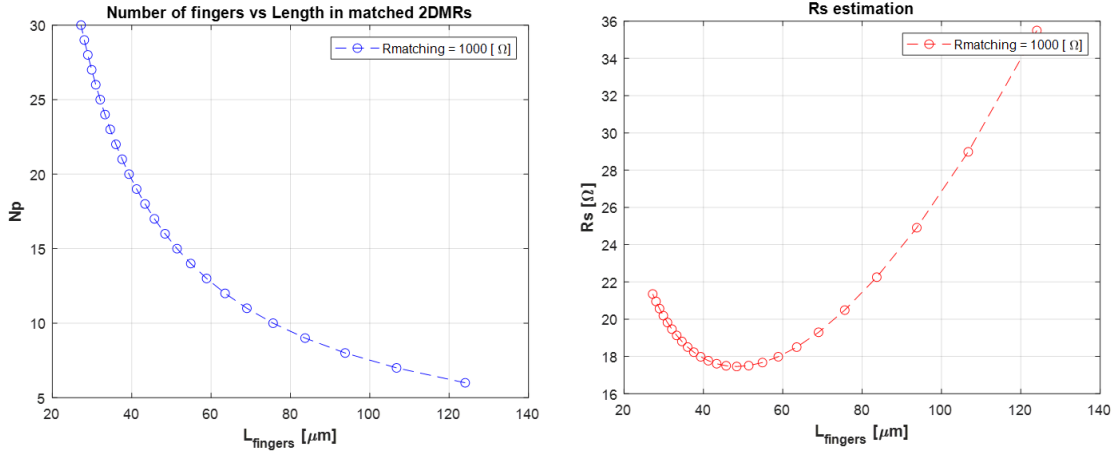
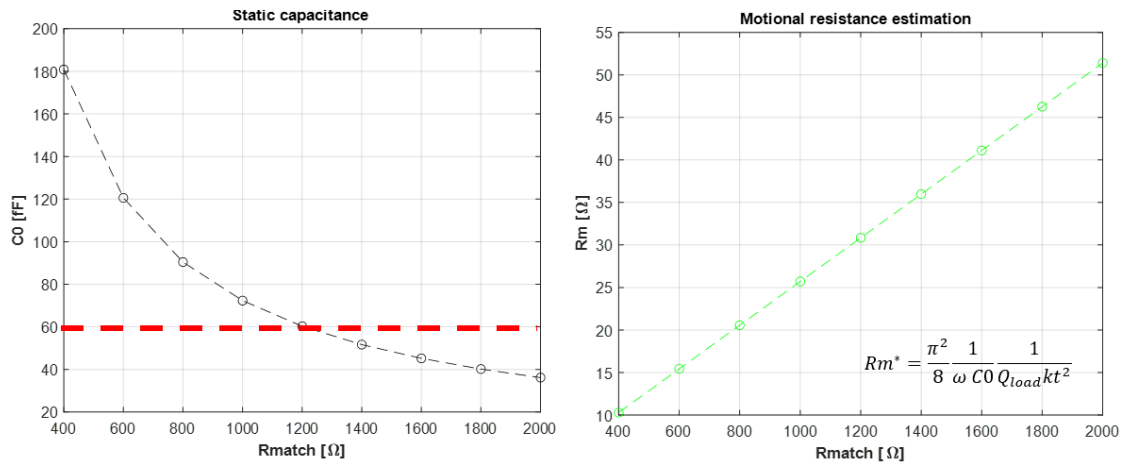


Figure A.1: 2DMR layout example with different resistance contributions.



**Figure A.2:**  $N_p$  vs  $L_e$  relation in a  $1 [K\Omega]$  matched 2DMR with  $150 [\mu m]$  thick Pt electrodes and  $R_s$  estimation. The  $R_s$  dependence on the finger length shows an absolute minimum.



**Figure A.3:**  $C_0$  and  $R_m$  dependence on the matching resistance in a 2DMR with  $150 [\mu m]$  thick Pt electrodes.



# Appendix B

## *gdspy* for layout drawings

To pay homage to the time spent perfecting the Python codes for the masks drawings, the outline of how the the design of the layouts has been organized is here included. The codes have been originally thought by Ph.D. Luca Colombo for basic structures and have been significantly amplified for the experimental plans discussed in the last chapter of this thesis. Three main files are here considered. The first Python file defines the classes of the resonators where all the main parameters as the layout layers and resonators dimensions are defined. The second file includes dozens of functions defining the geometries of the different blocks building the resonators. As unusual geometries have been introduced for the apodization and 2-ports devices studies, personalized functions have been coded for each case. For the sake of conciseness, only one example is reported below. Both the files are imported in a third code that reads a *.csv* list (fig.B.1) listing all the resonators referring to a specific study and recalls the functions related to that topology. This is a very efficient way of building complex layouts including huge numbers of devices in a very short time.

```
1 ##### DEVICES CLASSES #####
2 ##### Author: Luca Colombo #####
3 ##### Modified by: Fabio Bersano #####
4 ##### Date: July 2020 #####
5
6 class constants:
7     def __init__(self):
8
9         #LAYERS
10        self.layerSi = 0
11        self.layerBottom = 1
12        self.layerTop = 2
13        self.layerPad = 3
```

```

14     self.layerEtch = 4
15     self.layerVias = 5
16     self.layerPartialEtch = 6
17     self.layerBackSide = 7
18     self.layerGold = 9
19     #RESONATORS SPACING
20     self.rel = 20
21     self.safeRel = 20
22     self.deltaRes = 250
23     #RELEASE
24     self.Wpad = 80
25     self.Lpad = 80
26     self.GSG = 150
27     #OVERETCH (process variations)
28     self.overetchPlate = 0.7
29     self.overetchFingers = 0
30     #Distance between release pit and grounds
31     self.edgeRel = 2
32     #VIAs
33     self.viaSize = 6
34     self.viaSpace = 5
35     #BOTTOM ELECTRODE ROUTING FOR 2-PORT
36     self.distanceBottom = 2           #Distance between
bottom electrode and release pit
37     #Maximum allowed overlap between bottom elec. and traces
38     self.overlapBottom = 10
39     #BACKSIDE ETCH AND 2DRR
40     self.overetchBackSide = 10
41     #Distance between electrode and trench
42     self.overetchTrench = 0.5
43
44 #BASE RESONATOR
45
46 class device:
47     def __init__(self, dataList, constants):
48
49         self.numb = dataList[0]
50         self.type = dataList[1]
51         self.ports = dataList[2]
52         self.bottom = dataList[3]
53         self.freq = dataList[4]
54         self.We = float(dataList[5])
55         self.Le = float(dataList[6])
56         self.spac = float(dataList[7])
57         self.bus = float(dataList[8])
58         self.gap = float(dataList[9])
59         self.NAnchors = int(dataList[10])
60         self.Wa = float(dataList[11])
61         self.La = float(dataList[12])

```

```
62     self.c = float(dataList[13])
63     self.Nfingers = int(dataList[14])
64     self.aperture = int(dataList[15])
65     self.pads = dataList[16]
66     self.release = dataList[17]
67     self.study = dataList[18]
68
69     self.name = self.numb + "_" + self.type + "_" + self.freq
70     self.p = self.We + self.spac
71     self.W = self.Nfingers*self.p
72     self.L = self.Le + 2*self.bus + 2*self.gap
73
74     #ADD OVERTCHS
75     self.Lr = self.L + 2*constants.overetchPlate
76     self.Wr = self.W + 2*constants.overetchPlate
77     self.War = self.Wa + 2*constants.overetchPlate
78     self.Lar = self.La - 2*constants.overetchPlate
79
80     self.cr = self.c + 2*constants.overetchFingers/self.p
81
82 #POSITIONING OF THE STRUCTURES
83 class origin:
84     def __init__(self, X, Y):
85         self.X0 = X
86         self.Y0 = Y
87
88     def updateOrigin(self, dx, dy):
89         self.X0 = self.X0 + dx
90         self.Y0 = self.Y0 + dy
```

```
1
2 ##### DEVICES LIBRARY EXAMPLE #####
3 ##### Author: Fabio Bersano #####
4 ##### Date: July 2020 #####
5
6 import gds.py
7 import math
8 from math import pi
9 import os
10 import csv
11
12 # FUNCTION DRAWING THE SINUSOIDAL SHAPED TOP ELECTRODES
13 def draw2DMRFinTopSine(X0, Y0, cell, resonator, constants, terminal):
14
15     res = resonator
16     con = constants
17
```

```

18     if terminal == 1:
19         N = res.Nfingers1
20     else:
21         N = res.Nfingers2
22
23     for j in range(0, N):
24
25         XinitialStart=X0-res.totW/2.0+0.5*res.p-0.5*res.p*res.cr
26         XfinStart=X0-res.totW/2.0+0.5*res.p+j*res.p-0.5*res.p*res.cr
27         XfinEnd=XfinStart+res.p*res.cr
28         XfinalSt=X0-res.totW/2.0+0.5*res.p+(N-1)*res.p-0.5*res.p*res.
29     cr
30         YfinSt=Y0-res.L/2.0+res.bus+res.gap+res.aperture-res.aperture
31         *math.sin((XfinStt-XinitialStart)*pi/(XfinalSt-XinitialStart))
32         YfinEnd=Y0+res.L/2.0-res.bus
33         fingerTmp=gdspy.Rectangle((XfinStart, YfinStart),(XfinEnd,
34         YfinEnd, layer=con.layerTop)
35         cell.add(fingerTmp)
36
37     return cell
38
39     ...
40
41     ...

```

	A	B	C	D	E	F	G	H	I	J	K	L	M	N	O	P	Q	R	S
1	Number	Type	Ports	Bottom	Freq	We	Le	Spacing	bus	gap	Nanchors	Wa	La	c	Nf	A	PADS	Release	Study
2	1	ZDMR	1Y	2.2	0.8		50	3.3.8	0.95		1	4	3.0.21		15	0 GS	Y	ANCHORS	
3	2	ZDMR	1Y	2.2	0.8		50	3.3.8	0.95		1	5	3.0.21		15	0 GS	Y	ANCHORS	
4	3	ZDMR	1Y	2.2	0.8		50	3.3.8	0.95		1	6	3.0.21		15	0 GS	Y	ANCHORS	
5	4	ZDMR	1Y	2.2	0.8		50	3.3.8	0.95		1	7	3.0.21		15	0 GS	Y	APO-SINE	
6	5	ZDMR	1Y	2.2	0.8		50	3.3.8	0.95		1	8	3.0.21		15	0 GS	Y	APO-POLY1	
7	6	ZDMR	1Y	2.2	0.8		50	3.3.8	0.95		1	9	3.0.21		15	0 GS	Y	ANCHORS	
8	7	ZDMR	1Y	2.2	0.8		50	3.3.8	0.95		1	10	3.0.21		15	0 GS	Y	ANCHORS	
9	8	ZDMR	1Y	2.2	0.8		50	3.3.8	0.95		1	4.3.5	0.21		15	0 GS	Y	ANCHORS	
10	9	ZDMR	1Y	2.2	0.8		50	3.3.8	0.95		1	5.3.5	0.21		15	0 GS	Y	ANCHORS	
11	10	ZDMR	1Y	2.2	0.8		50	3.3.8	0.95		1	6.3.5	0.21		15	0 GS	Y	ANCHORS	
12	11	ZDMR	1Y	2.2	0.8		50	3.3.8	0.95		1	7.3.5	0.21		15	0 GS	Y	ANCHORS	
13	12	ZDMR	1Y	2.2	0.8		50	3.3.8	0.95		1	8.3.5	0.21		15	0 GS	Y	ANCHORS	
14	13	ZDMR	1Y	2.2	0.8		50	3.3.8	0.95		1	9.3.5	0.21		15	0 GS	Y	ANCHORS	
15	14	ZDMR	1Y	2.2	0.8		50	3.3.8	0.95		1	10.3.5	0.21		15	0 GS	Y	ANCHORS	
16	15	ZDMR	1Y	2.2	0.8		50	3.3.8	0.95		1	4	4.0.21		15	0 GS	Y	ANCHORS	
17	16	ZDMR	1Y	2.2	0.8		50	3.3.8	0.95		1	5	4.0.21		15	0 GS	Y	ANCHORS	
18	17	ZDMR	1Y	2.2	0.8		50	3.3.8	0.95		1	6	4.0.21		15	0 GS	Y	ANCHORS	
19	18	ZDMR	1Y	2.2	0.8		50	3.3.8	0.95		1	7	4.0.21		15	0 GS	Y	ANCHORS	
20	19	ZDMR	1Y	2.2	0.8		50	3.3.8	0.95		1	8	4.0.21		15	0 GS	Y	ANCHORS	
21	20	ZDMR	1Y	2.2	0.8		50	3.3.8	0.95		1	9	4.0.21		15	0 GS	Y	ANCHORS	
22	21	ZDMR	1Y	2.2	0.8		50	3.3.8	0.95		1	10	4.0.21		15	0 GS	Y	ANCHORS	
23	22	ZDMR	1Y	2.2	0.8		50	3.3.8	0.95		1	11	4.0.21		15	0 GS	Y	ANCHORS	

Figure B.1: portion of the Excel file listing the devices included in one of the experimental plans.

```
1
2 ##### csv READER & GDS FILE #####
3 ##### Authors: Luca Colombo & Fabio Bersano #####
4 ##### Date: July 2020 #####
5
6 #IMPORT LIBRARY
7 %run ./Library2DMR.ipynb
8 %run ./Classes2DMR.ipynb
9
10 #CREATE LIBRARY AND CELL
11 lib = gdspy.GdsLibrary()
12 #cell = lib.new_cell('RES')
13 cell = gdspy.Cell('RES')
14 cnst = constants()
15 k = 1
16
17 X0 = 0.0
18 Y0 = 0.0
19
20 #CSV READER
21
22 dataList = []
23
24 with open('2DMR_list.csv') as f:
25     reader = csv.reader(f)
26     for row in reader:
27         dataList.append(row)
28
29 for i in range(1, len(dataList)):
30     k = k+1
31
32     resonator = device(dataList[i][:], cnst)
33
34     #RESONATOR PLATE AND ANCHORS
35     if resonator.NAnchors == 1:
36         study = resonator.study
37         drawEtch(X0, Y0, cell, resonator, cnst, study)
38     else:
39         drawEtchMultiAnchor(X0, Y0, cell, resonator, cnst)
40
41     #RESONATOR ELECTRODES AND VIAS
42
43     if resonator.study == "APO-SINE":
44         draw2DMRBusTop(X0, Y0, cell, resonator, cnst)
45         draw2DMRFinTopSine(X0, Y0, cell, resonator, cnst)
46         drawGoldContacts(X0, Y0, cell, resonator, cnst)
47
48         if resonator.bottom == "Y":
```

```

49         draw2DMRFinBottomSine(X0, Y0, cell, resonator, cnst)
50         draw2DMRBusBottom(X0, Y0, cell, resonator, cnst)
51         draw2DMRVIAAs(X0,Y0,cell, resonator, cnst)
52     else:
53         draw2DMRBottom(X0, Y0, cell, resonator, cnst)
54         draw2DMRVIAAs(X0,Y0,cell, resonator, cnst)
55
56     elif resonator.study == "APO-CIRCLE":
57         draw2DMRBusTop(X0, Y0, cell, resonator, cnst)
58         draw2DMRFinTopCircle(X0, Y0, cell, resonator, cnst)
59         drawGoldContacts(X0,Y0,cell, resonator, cnst)
60
61         if resonator.bottom == "Y":
62             draw2DMRFinBottomCircle(X0, Y0, cell, resonator, cnst)
63             draw2DMRBusBottom(X0, Y0, cell, resonator, cnst)
64             draw2DMRVIAAs(X0,Y0,cell, resonator, cnst)
65         else:
66             draw2DMRBottom(X0, Y0, cell, resonator, cnst)
67             draw2DMRVIAAs(X0,Y0,cell, resonator, cnst)
68
69     elif resonator.study == "APO-POLY1":
70         draw2DMRBusTop(X0, Y0, cell, resonator, cnst)
71         draw2DMRFinTopPoly(X0, Y0, cell, resonator, cnst,1)
72         drawGoldContacts(X0,Y0,cell, resonator, cnst)
73
74         if resonator.bottom == "Y":
75             draw2DMRFinBottomPoly(X0, Y0, cell, resonator, cnst,1)
76             draw2DMRBusBottom(X0, Y0, cell, resonator, cnst)
77             draw2DMRVIAAs(X0,Y0,cell, resonator, cnst)
78         else:
79             draw2DMRBottom(X0, Y0, cell, resonator, cnst)
80             draw2DMRVIAAs(X0,Y0,cell, resonator, cnst)
81
82     elif resonator.study == "APO-POLY2":
83         draw2DMRBusTop(X0, Y0, cell, resonator, cnst)
84         draw2DMRFinTopPoly(X0, Y0, cell, resonator, cnst,2)
85         drawGoldContacts(X0,Y0,cell, resonator, cnst)
86
87         if resonator.bottom == "Y":
88             draw2DMRFinBottomPoly(X0, Y0, cell, resonator, cnst,2)
89             draw2DMRBusBottom(X0, Y0, cell, resonator, cnst)
90             draw2DMRVIAAs(X0,Y0,cell, resonator, cnst)
91         else:
92             draw2DMRBottom(X0, Y0, cell, resonator, cnst)
93             draw2DMRVIAAs(X0,Y0,cell, resonator, cnst)
94
95     elif resonator.study == "APO-POLY3":
96         draw2DMRBusTop(X0, Y0, cell, resonator, cnst)
97         draw2DMRFinTopPoly(X0, Y0, cell, resonator, cnst,3)

```

```

98     drawGoldContacts(X0,Y0,cell , resonator , cnst)
99
100    if resonator.bottom == "Y":
101        draw2DMRFinBottomPoly(X0, Y0, cell , resonator , cnst,3)
102        draw2DMRBusBottom(X0, Y0, cell , resonator , cnst)
103        draw2DMRVias(X0,Y0,cell , resonator , cnst)
104    else:
105        draw2DMRBottom(X0, Y0, cell , resonator , cnst)
106        draw2DMRVias(X0,Y0,cell , resonator , cnst)
107
108    elif resonator.study == "ANCHORS" or resonator.study == "MODES"
or resonator.study == "SHORT-LONG":
109        draw2DMRBusTop(X0, Y0, cell , resonator , cnst)
110        draw2DMRFinTop(X0, Y0, cell , resonator , cnst)
111        drawGoldContacts(X0,Y0,cell , resonator , cnst)
112
113    if resonator.bottom == "Y":
114        draw2DMRFinBottom(X0, Y0, cell , resonator , cnst)
115        draw2DMRBusBottom(X0, Y0, cell , resonator , cnst)
116        draw2DMRVias(X0,Y0,cell , resonator , cnst)
117    else:
118        draw2DMRBottom(X0, Y0, cell , resonator , cnst)
119        draw2DMRVias(X0,Y0,cell , resonator , cnst)
120
121    else:
122        print("Invalid code")
123
124    #RESONATOR PADS
125    drawPads(X0, Y0, cell , resonator , cnst, "Y")
126
127    #POSITIONING
128    if k <= 22:
129        if (resonator.pads == 'GSG'):
130            X0 = X0 + 2*cnst.deltaRes
131        else:
132            X0 = X0 + 2*cnst.GSG
133        #Y0 = 0
134    else:
135        X0 = 0.0
136        Y0 = Y0-2*cnst.deltaRes + 30
137        k = 1
138
139    lib.write_gds('2DMR_COMPLETE_LAYOUT.gds')

```



# Bibliography

- [1] Jie Zou, Chih-Ming Lin, C. S. Lam, and Albert P. Pisano. «Transducer design for AlN Lamb wave resonators». In: *Journal of Applied Physics* 121.15 (2017), p. 154502. DOI: 10.1063/1.4979914 (cit. on pp. 1, 27, 29, 30, 63, 68, 71).
- [2] Miguel A Caro, Siyuan Zhang, Tommi Riekkinen, Markku Ylilammi, Michelle A Moram, Olga Lopez-Acevedo, Jyrki Molarius, and Tomi Laurila. «Piezoelectric coefficients and spontaneous polarization of ScAlN». In: *Journal of Physics: Condensed Matter* 27.24 (2015), p. 245901 (cit. on pp. 3, 94, 95).
- [3] X. Zhao and C. Cassella. «On the Coupling Coefficient of ScyAl1-yN-based Piezoelectric Acoustic Resonators». In: *2019 Joint Conference of the IEEE International Frequency Control Symposium and European Frequency and Time Forum (EFTF/IFC)*. 2019, pp. 1–4 (cit. on p. 3).
- [4] H. Bhugra and G. Piazza. *Piezoelectric MEMS Resonators*. Microsystems and Nanosystems. Springer International Publishing, 2017. ISBN: 9783319286884 (cit. on pp. 3, 4, 8, 15, 16, 20, 21).
- [5] D Gerlich, SL Dole, and GA Slack. «Elastic properties of aluminum nitride». In: *Journal of Physics and Chemistry of Solids* 47.5 (1986), pp. 437–441 (cit. on p. 4).
- [6] K.Y. Hashimoto. *Surface Acoustic Wave Devices in Telecommunications: Modelling and Simulation*. Engineering online library. Springer Berlin Heidelberg, 2000. ISBN: 9783540672326 (cit. on pp. 5–7).
- [7] Z. Su and L. Ye. *Identification of Damage Using Lamb Waves: From Fundamentals to Applications*. Lecture Notes in Applied and Computational Mechanics. Springer London, 2009. ISBN: 9781848827844 (cit. on pp. 10, 12).
- [8] J.L. Rose. *Ultrasonic Guided Waves in Solid Media*. Titolo collana. Cambridge University Press, 2014. ISBN: 9781107048959 (cit. on pp. 11, 13).
- [9] Christopher Hakoda, Joseph Rose, Parisa Shokouhi, and Clifford Lissenden. «Using Floquet periodicity to easily calculate dispersion curves and wave structures of homogeneous waveguides». In: *AIP Conference Proceedings*. Vol. 1949. 1. AIP Publishing LLC. 2018, p. 020016 (cit. on p. 13).

- 
- [10] C. Cassella, Y. Hui, Z. Qian, G. Hummel, and M. Rinaldi. «Aluminum Nitride Cross-Sectional Lamé Mode Resonators». In: *Journal of Microelectromechanical Systems* 25.2 (2016), pp. 275–285 (cit. on p. 21).
- [11] Gianluca Piazza, Philip J Stephanou, and Albert P Pisano. «Piezoelectric aluminum nitride vibrating contour-mode MEMS resonators». In: *Journal of Microelectromechanical systems* 15.6 (2006), pp. 1406–1418 (cit. on p. 23).
- [12] Chengjie Zuo et al. «Cross-sectional dilation mode resonator with very high electromechanical coupling up to 10 % using AlN». In: *2012 IEEE International Frequency Control Symposium Proceedings*. IEEE. 2012, pp. 1–4 (cit. on pp. 23, 24, 29).
- [13] Cristian Cassella and Gianluca Piazza. «AlN two-dimensional-mode resonators for ultra-high frequency applications». In: *IEEE Electron Device Letters* 36.11 (2015), pp. 1192–1194 (cit. on pp. 24, 30, 44, 58).
- [14] Yao Zhu, Nan Wang, Bangtao Chen, and Ying Zhang. «AlN BAW-like Resonators with Patterned Top Electrodes Achieving Coupling Coefficient up to 8% at > 2.5 GHz». In: *2019 IEEE International Ultrasonics Symposium (IUS)*. IEEE. 2019, pp. 93–95 (cit. on p. 24).
- [15] Xuanyi Zhao, Luca Colombo, and Cristian Cassella. «Aluminum nitride two-dimensional-resonant-rods». In: *Applied Physics Letters* 116.14 (2020), p. 143504 (cit. on p. 25).
- [16] Cristian Cassella, Nicolò Oliva, Jeffrey Soon, Merugu Srinivas, Navab Singh, and Gianluca Piazza. «Super High Frequency Aluminum Nitride Two-Dimensional Mode Resonators With  $k_t^2$  exceeding 4.9%». In: *IEEE Microwave and Wireless Components Letters* 27.2 (2017), pp. 105–107 (cit. on pp. 27, 29, 30, 58).
- [17] Gianluca Piazza and Christian Cassella. *Two-dimensional mode resonators*. US Patent App. 15/560,757. Mar. 2018 (cit. on p. 30).
- [18] Cristian Cassella and Jeronimo Segovia-Fernandez. «High  $k_t^2$  exceeding 6.4% through metal frames in aluminum nitride 2-D mode resonators». In: *IEEE transactions on ultrasonics, ferroelectrics, and frequency control* 66.5 (2019), pp. 958–964 (cit. on pp. 30, 31, 58, 66).
- [19] Cristian Cassella, Guofeng Chen, Zhenyun Qian, Gwendolyn Hummel, and Matteo Rinaldi. «Cross-sectional Lamé mode ladder filters for UHF wideband applications». In: *IEEE Electron Device Letters* 37.5 (2016), pp. 681–683 (cit. on pp. 31, 34).
- [20] Reza Abdolvand, Behraad Bahreyni, Joshua E-Y Lee, and Frederic Nabki. «Micromachined resonators: A review». In: *Micromachines* 7.9 (2016), p. 160 (cit. on pp. 34, 35).

- [21] Gianluca Piazza. «Integrated aluminum nitride piezoelectric microelectromechanical system for radio front ends». In: *Journal of Vacuum Science & Technology A: Vacuum, Surfaces, and Films* 27.4 (2009), pp. 776–784 (cit. on pp. 35, 36).
- [22] D. S. Binder, E. Quevy, T. Koyama, S. Govindjee, J. W. Demmel, and R. T. Howe. «Anchor loss simulation in resonators». In: *18th IEEE International Conference on Micro Electro Mechanical Systems, 2005. MEMS 2005*. 2005, pp. 133–136 (cit. on p. 37).
- [23] David S Bindel and Sanjay Govindjee. «Elastic PMLs for resonator anchor loss simulation». In: *International Journal for Numerical Methods in Engineering* 64.6 (2005), pp. 789–818 (cit. on p. 39).
- [24] Jeronimo Segovia-Fernandez and Gianluca Piazza. «Analytical and numerical methods to model anchor losses in 65-MHz AlN contour mode resonators». In: *Journal of Microelectromechanical Systems* 25.3 (2016), pp. 459–468 (cit. on pp. 39, 41, 48, 49).
- [25] Jie Zou. «High-performance aluminum nitride Lamb wave resonators for RF front-end technology». PhD thesis. UC Berkeley, 2015 (cit. on p. 41).
- [26] Cristian Cassella, Navab Singh, Bo Woon Soon, and Gianluca Piazza. «Quality factor dependence on the inactive regions in AlN contour-mode resonators». In: *Journal of Microelectromechanical Systems* 24.5 (2015), pp. 1575–1582 (cit. on pp. 41–43).
- [27] Andrea Lozzi, Annalisa De Pastina, Ernest Ting-Ta Yen, and Luis Guillermo Villanueva. «Engineered acoustic mismatch for anchor loss control in contour mode resonators». In: *Applied Physics Letters* 114.10 (2019), p. 103502 (cit. on p. 41).
- [28] Brian Gibson, Kamala Qalandar, Cristian Cassella, Gianluca Piazza, and Kimberly L Foster. «A study on the effects of release area on the quality factor of contour-mode resonators by laser doppler vibrometry». In: *IEEE transactions on ultrasonics, ferroelectrics, and frequency control* 64.5 (2017), pp. 898–904 (cit. on p. 45).
- [29] B.A. Auld. *Acoustic fields and waves in solids*. A Wiley-Interscience publication. Wiley, 1973. ISBN: 9785885013437 (cit. on pp. 47, 48).
- [30] J. Segovia-Fernandez and C. Cassella. «Active and Inactive Frames Improve Figure of Merit of Two Dimensional Mode Resonators». In: *2018 IEEE International Ultrasonics Symposium (IUS)*. 2018, pp. 206–212 (cit. on p. 58).

- [31] M. Giovannini, S. Yazici, N. Kuo, and G. Piazza. «Spurious mode suppression via apodization for 1 GHz AlN Contour-Mode Resonators». In: *2012 IEEE International Frequency Control Symposium Proceedings*. 2012, pp. 1–5 (cit. on pp. 72, 73).
- [32] G. Chen, C. Cassella, T. Wu, and M. Rinaldi. «Single-chip multi-frequency wideband filters based on aluminum nitride cross-sectional Lamé mode resonators with thick and apodized electrodes». In: *2018 IEEE Micro Electro Mechanical Systems (MEMS)*. 2018, pp. 775–778 (cit. on pp. 72–74).
- [33] Yoginder Kumar, Jitendra Singh, Gunjan Kumari, Ravindra Singh, and Jamil Akhtar. «Effect of shapes and electrode material on figure of merit (FOM) of BAW resonator». In: *AIP Conference Proceedings*. Vol. 1724. 1. AIP Publishing LLC. 2016, p. 020045 (cit. on p. 73).
- [34] Guofeng Chen, Cristian Cassella, Tao Wu, and Matteo Rinaldi. «Single-chip multi-frequency wideband filters based on aluminum nitride cross-sectional Lamé mode resonators with thick and apodized electrodes». In: *2018 IEEE Micro Electro Mechanical Systems (MEMS)* (2018), pp. 775–778 (cit. on p. 74).
- [35] Wanling Pan, Vikram A Thakar, Mina Rais-Zadeh, and Farrokh Ayazi. «Acoustically coupled thickness-mode AlN-on-Si band-pass filters-part I: principle and devices». In: *IEEE transactions on ultrasonics, ferroelectrics, and frequency control* 59.10 (2012), pp. 2262–2269 (cit. on p. 80).
- [36] Vikram A Thakar, Wanling Pan, Farrokh Ayazi, and Mina Rais-Zadeh. «Acoustically coupled thickness-mode AlN-on-Si band-pass filters-Part II: simulation and analysis». In: *IEEE transactions on ultrasonics, ferroelectrics, and frequency control* 59.10 (2012), pp. 2270–2277 (cit. on p. 80).
- [37] D. A. Frickey. «Conversions between S, Z, Y, H, ABCD, and T parameters which are valid for complex source and load impedances». In: *IEEE Transactions on Microwave Theory and Techniques* 42.2 (1994), pp. 205–211 (cit. on p. 83).